LIQUID-CRYSTAL ALIGNMENT MECHANISMS AND INFLUENCE ON DISPLAY-DEVICE CHARACTERISTICS

BY
SHOHEI NAEMURA

JUNE 1982

ABSTRACT

The relationships between measured liquid-crystal anchoring parameters, such as easy-axis angle Θ and anchoring-strength coefficient B_θ, and substrate-surface energy polar and nonpolar (dispersive) components, γ_S^p and γ_S^d, are obtained both theoretically and experimentally. It is found that either low γ_S^p or low γ_S^d substrates introduce $\Theta = 0°$ (homeotropic alignment) and large-B_θ conditions. The low γ_S^p conditions are shown to be obtained by surfactant alkyl chains which screen the substrate-surface electrostatic potential and the low γ_S^d conditions by surfactant fluorocarbon chains, for example.

Moreover, relaxation time τ_{rp} from the field-induced nematic state to the quiescent cholesteric state is found to become minimum in $\Theta = 0°$ cases and to be shorter for larger B_θ. As a result, memory type of liquid-crystal matrix display devices are fabricated with several new features, including that the "wash-out" problem, when storing the displayed information, is diminished by the fast nematic→cholesteric transition which is realized by selecting an optimum surface-treatment technique.

Wall effects on the Freedericksz transition are analyzed and utilized to derive B_θ values from measured Θ and threshold field strength H_c' for the Freedericksz transition. Angle Θ and threshold field H_c' are measured by either an improved magneto-capacitance method or a newly developed total-reflection method, using various surface-treated substrates. Angle Θ and derived B_θ values are related to the surfactant molecular structures and the substrate materials. It is found that polar and nonpolar interaction forces play individual roles in aligning liquid-crystal molecules. Those polar and nonpolar contributions are clarified by measurements of surface-energy polar and nonpolar components, γ_S^p and γ_S^d. The relationships between anchoring pa-

rameters, Θ and B_θ, and substrate surface-energy components, γ_S^p and γ_S^d, are also obtained theoretically. It is explained that the liquid-crystal interfacial alignment is controlled by the anisotropy of liquid-crystal surface energy.

The structural arrangement of short-pitch cholesteric liquid-crystals between parallel substrates with $\Theta = 0°$ condition is proposed. Furthermore, a director realignment model is suggested for the relaxation from a field-induced nematic state to the quiescent cholesteric structure. Nematic→cholesteric relaxation time τ_{rp} is shown to depend on anchoring parameters, Θ and B_θ. That is, $\Theta = 0°$ and large-B_θ conditions are found to realize a fast nematic→cholesteric relaxation. Finally, it is shown that improved storage type of matrix display devices can be fabricated by utilizing the fast nematic→cholesteric relaxation.

TABLE OF CONTENTS

FIGURES LIST

TABLES LIST

I. INTRODUCTION

Liquid-crystal materials exhibit various electro-optic effects such as dynamic scattering mode, twisted nematic mode, deformation of aligned phases, etc. Corresponding to those varieties of liquid-crystal electro-optic effects, there are several types of liquid-crystal display devices. Although a few of those liquid-crystal electro-optic effects are caused by electrically induced charged-particle flow, the majority bases their operational principles on the liquid-crystal molecular realignment induced by an electric field. For these field-induced electro-optic effects, it is practically important to control the initial liquid-crystal molecular alignment so that the field-induced liquid-crystal molecular realignment produces optimum changes in optical characteristics. In addition, even for electro-optic effects caused by charged-particle flow, the initial liquid-crystal molecular alignment affects display-device characteristics such as threshold sharpness and contrast ratio. Consequently, the initial liquid-crystal molecular alignment is very important for every type of liquid-crystal display devices. The initial liquid-crystal molecular alignment is subject to the liquid-crystal substrate interfacial alignment for a practical liquid-crystal layer thickness ($< \sim 100\ \mu m$). Thus, the liquid-crystal interfacial alignment control is important for liquid-crystal display devices. Many efforts have been made, both to develop techniques for aligning liquid-crystal molecules uniformly on substrates and to study their mechanisms.

Two kinds of liquid-crystal alignments are used for display devices: In one, liquid-crystal molecules lie parallel to substrates (parallel alignment) or lie with a slight tilt angle relative to substrates (low-tilted alignment), and in the other, liquid-crystal molecules lie perpendicular to substrates (homeotropic alignment).

Parallel and low-tilted alignments are usually obtained by rubbing [1] or oblique evaporation[2-4] technique. These techniques are those for forming microgrooves at substrate surfaces. The molecular alignments caused by substrates with microgrooves are explained by Berreman[5] in terms of elastic strain energy and short-range molecular forces by molecules aligned in some preferred direction on the substrate surfaces. In this interpretation, however, the origin of the preferable alignment at the substrate surface is not clarified.

On the other hand, the homeotropic alignment is produced by various techniques such as chemical[6-8] or plasma[9] etching, plasma polymerization[9-11], sputtering[10,11], evaporation of heat-degradation products[12] and deposition from solution[13-21]. Almost all of these techniques are for forming desirable material layers on the substrate surfaces, which cause liquid-crystal molecules to align in preferable directions. In these flat substrate cases, the liquid-crystal alignment is directly controlled by its preferable alignment on substrate surfaces. Thus, whether a microgrooved or flat substrate surface, it is practically important to consider the origin of liquid-crystal preferable alignments on substrate surfaces.

Among several existing hypotheses on the liquid-crystal interfacial alignments, a steric model states that parallel or perpendicular alignment of the surfactant alkyl chains on substrates produces the liquid-crystal parallel or homeotropic alignment, respectively[15]. Although this steric effect seems to be one factor to control the liquid-crystal interfacial alignment, it cannot give any idea for liquid-crystal material dependence of the interfacial alignment. On the other hand, several studies have been directed to explain the relations between liquid-crystal molecular alignment and the substrate surface energies. Pioneer works in this field were made by Creagh-Kmetz[17] and Kahn[22], who stated that the parallel (homeotropic) alignment is produced in the case when the substrate

critical surface-tension γ_c is larger (smaller) than liquid-crystal surface tensions γ_{LC}. Dubois *et al.*[11] investigated liquid-crystal alignments for the combinations of several liquid-crystal materials and substrates, and made it clear that very good homeotropic alignment is observed when γ_c is very low in front of γ_{LC} and, conversely, high energy surfaces induce parallel alignment. Haller[23], however, pointed out that the γ_c-hypothesis lacks universal validity, and Perez *et al.*[24] insisted on the necessity for considering polar interaction contributions.

It is theoretically suggested that the anchoring strength also affects liquid-crystal display-device characteristics[25]. Consequently, for manufacturing liquid-crystal display devices with desired characteristics, it is necessary to control not only liquid-crystal molecular alignment angle but also liquid-crystal molecular anchoring strength on substrate surfaces. At an earlier stage, the liquid-crystal substrate interfacial interaction forces were assumed to be large enough for restricting liquid-crystal molecular alignment in the "easy axis" direction against external fields, which act to realign liquid-crystal molecules. Some topological observations [12,21], however, suggest that interfacial interaction forces between liquid-crystal molecules and substrate surfaces with organic layers are not always so strong. Their observation principle is based on the fact that, when liquid-crystal layer thickness ℓ is smaller than a characteristic length, the so-called extrapolation length[26], there occurs a Bloch wall of width d, which is represented as $d \simeq (\ell K/W_s)^{1/2}$ by using Frank's elastic constant K and surface energy density W_s. Ryschenkow *et al.*[12] measured the Bloch-wall width for the sample which consisted of 4'-methoxybenzylidene-4-*n*-butylaniline (MBBA) and substrates covered with the product of degradation from heated paper, and derived their interfacial interaction energy density (anchoring strength) on the order of 10^{-4} erg/cm^2. By using this method, Porte[21] derived an anchoring

strength on the same order for the interface between MBBA and substrate with *n*-alkylamine layer. Although their observations are effective to suggest that strong anchoring conditions are not necessarily realized, their method is not a precise one to measure the liquid-crystal substrate interfacial interaction strength. The reason is that the anchoring strength, which can be measured by the above-mentioned method, is limited to be very small ($\sim 10^{-4}$ erg/cm^2), when samples of ordinary thickness (10 $\sim$ several 10 μm) are used.

In the above-mentioned situation, in order to improve liquid-crystal display-device characteristics from the viewpoint of substrate-surface treatments, the following systematic study is needed.
(1) Develop a measuring method for liquid-crystal interfacial alignment conditions, which are subject to anchoring parameters. Throughout this dissertation, "interfacial alignment condition" represents a situation that liquid-crystal molecules align with a polar angle θ_0 on a substrate surface which is characterized by "anchoring parameters", i.e., easy-axis angle Θ and anchoring-strength coefficient B_θ.
(2) Measure interfacial alignment condition for various surface treatments, and obtain relationships between anchoring parameters and surfactant structures or surface-treatment procedures.
(3) Clarify the relationships between the anchoring parameters and the liquid-crystal display-device characteristics.
This procedure is shown by a blockdiagram in Fig. 1-1.

This dissertation describes the study on liquid-crystal alignment mechanisms and influence on display-device characteristics along the above guideline, as shown in Fig. 1-1. In this study, a new method to measure the liquid-crystal interfacial alignment conditions is developed. Section II presents the analysis of wall effects on the Freedericksz transition, which gives the theoretical basis for the liquid-crystal anchoring-strength measurements. In

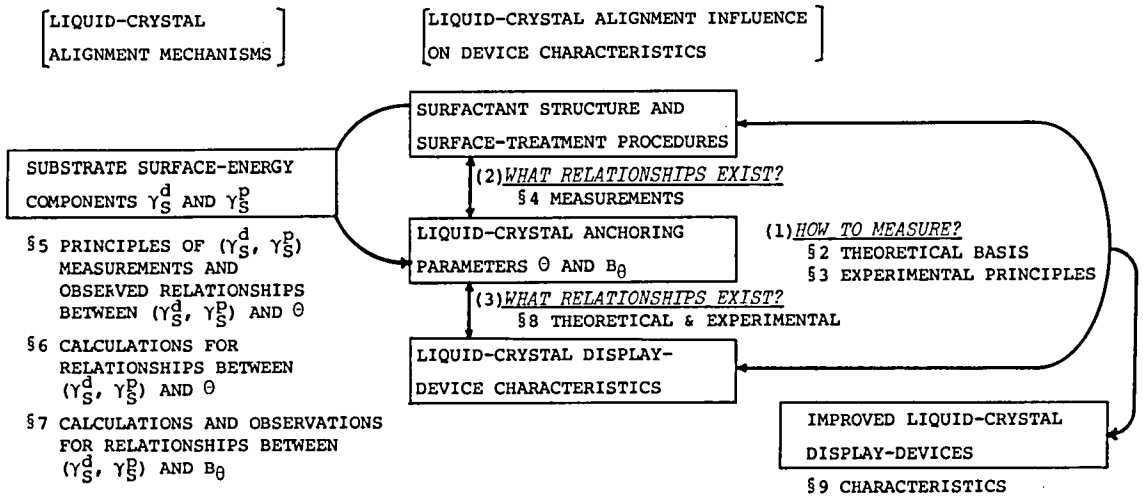

Fig. 1-1 Present study procedure blockdiagram.

Section III , the principles of both interfacial alignment angle and the Freedericksz-transition measurements are presented, which enable anchoring parameter derivation. In Section IV , the anchoring parameters are derived for various surface-treated substrates and the effects of both surfactant structures and substrate materials on the anchoring parameters are discussed. During the present study, the liquid-crystal alignment mechanisms are investigated through the intermediation of substrate surface-energy considerations. Section V is devoted to obtaining some relations between the liquid-crystal interfacial alignment angles and the surface energies for surface-treated substrates. In Section VI , liquid-crystal surface energy is represented in an alignment-angle dependent form. Calculations are performed to obtain the relations between the easy-axis angle and the substrate surface-energies by utilizing the liquid-crystal surface-energy representation. Here, the existing γ_c-hypothesis validity is also discussed. In Section VII , in addition to the interfacial alignment-angle considerations in the above sections, calculations are performed for the liquid-crystal anchoring strength and are compared with experimental results. The following two sections are devoted to obtaining some relationships between liquid-crystal interfacial alignment conditions and liquid-crystal display-device characteristics. Section VIII clarifies both theoretically and experimentally that relaxation times in cholesteric $\leftrightarrow$ nematic transition type of electro-optic effects are strongly affected by the anchoring-parameter values. Section IX presents the characteristics of cholesteric $\leftrightarrow$ nematic transition type of liquid-crystal display devices, optimized from the viewpoint of liquid-crystal interfacial alignment conditions. Finally, in Section X, concluding remarks and suggestions for further study are presented.

References

[1] P. Chatelain, Bull. Soc. Fr. Mineral. Cristallogr., 66, 105 (1943)

[2] J. L. Janning, Appl. Phys. Lett., 21, 173 (1972)

[3] E. Guyon, P. Pieranski, and M. Boix, Lett. Appl. Eng. Sci., 1, 19 (1973)

[4] W. Urbach, M. Boix, and E. Guyon, Appl. Phys. Lett., 25, 479 (1974)

[5] D. W. Berreman, Phys. Rev. Lett., 28, 1683 (1972); Mol. Cryst. Liq. Cryst., 23, 215 (1973)

[6] M. F. Schiekel and K. Fahrenschon, Appl. Phys. Lett., 19, 391 (1971)

[7] R. F. Soref and M. J. Rafuse, J. Appl. Phys., 43, 2029 (1972)

[8] T. Uchida, H. Watanabe, and M. Wada, Jpn. J. Appl. Phys., 11, 1559 (1972)

[9] G. J. Sprokel and R. M. Gibson, J. Electrochem. Soc., 124, 557 (1977)

[10] J. C. Dubois, M. Gazard, and A. Zann, Appl. Phys. Lett., 24, 297 (1974)

[11] J. C. Dubois, M. Gazard, and A. Zann, J. Appl. Phys., 47, 1270 (1976)

[12] G. Ryschenkow and M. Kleman, J. Chem. Phys., 64, 404 (1976)

[13] P. R. Wagner, IBM Tech. Disclosure Bull., 13, 2961 (1971)

[14] W. Helfrich, Phys. Lett., 35A, 393 (1971)

[15] J. E. Proust, L. Ter-Minassian-Saraga, and E. Guyon, Solid State Commun., 11, 1227 (1972)

[16] G. Barzilai, P. Maltese, C. M. Ottavi, and P. Reali, IEEE Conf. on Display Device, Conference Record p.67 (1972)

[17] L. T. Creagh and A. R. Kmets, Mol. Cryst. Liq. Cryst., 24, 59 (1973)

[18] F. J. Kahn, Appl. Phys. Lett., 22, 386 (1973)

[19] T. Uchida, C. Shishido, and M. Wada, Elec. Commun. Japan, 58-C, 132 (1975)

[20] S. Matsumoto, M. Kawamoto, and N. Kaneko, Appl. Phys. Lett., 27, 268 (1975); S. Matsumoto, K. Mizunoya, D. Nakagawa, N. Kaneko, and M. Kawamoto, J. Phys. (Paris), C3-40, C3-510 (1979)

[21] G. Porte, J. Phys. (Paris), 37, 1245 (1976)

[22] F. J. Kahn, G. N. Taylor, and H. Schonhorn, Proc. IEEE, 61, 823 (1973)

[23] I. Haller, Appl. Phys. Lett., 24, 349 (1974)

[24] E. Perez, J. E. Proust, and L. Ter-Minassian-Saraga, Mol. Cryst. Liq. Cryst., 42, 167 (1977)

[25] J. Nehring, A. R. Kmetz, and T. J. Scheffer, J. Appl. Phys., 47, 850 (1976)

[26] P. G. de Gennes, *The Physics of Liquid Crystals* (Oxford University, London, 1974)

II . ANALYSIS OF WALL EFFECTS ON THE FREEDERICKSZ TRANSITION

2-1. Introduction

Liquid-crystal molecular realignment under an external field is considered to be affected by anchoring parameters at interfaces between the liquid-crystal layer and substrates. First of all, therefore, numerical analysis was performed to obtain relationships between field-induced director distortions and anchoring parameters, which make it possible to derive the anchoring parameters from director distortion observations.

Nematic liquid-crystal molecular realignment induced by an external magnetic field is well known as a Freedericksz transition [1]. The molecular realignment is subject to the competition between the interfacial energy and the bulk energy, i.e., the sum of elastic distortion energy and magnetic energy. In most existing Freedericksz-transition analyses, however, the interfacial molecular alignment angle is assumed not to change because of strong anchoring forces at the interface[2,3]. This assumption is made only for analytical simplicity and is never confirmed experimentally. Although, in a very few analyses, the anchoring-parameters effects on the Freedericksz transition are considered, both easy-axis angle[4] and anchoring strength[5] effects are treated separately.

In this section, the more general case is considered, where the nematic liquid-crystal molecules are weakly clamped with an intermediate angle (not 0° or 90°) relative to the substrates. In Section 2-2, an expression is given for the total free energy of a nematic liquid-crystal layer under a magnetic field by proposing a pertinent formula for the interfacial interaction energy. Section 2-3 presents the Euler equation solution for the total free energy functional, which gives a necessary condition for molecular alignments

with minimum energy. Section 2-4 presents the anchoring-parameters effects on molecular alignments with minimum energy under the magnetic field, that is the wall effects on the Freedericksz transition. The theoretical and computational results in this section are summarized in Section 2-5.

2-2. Free Energy Representation

A nematic liquid-crystal layer between parallel substrates, with distance ℓ, is considered. The coordinate system is shown in Fig. 2-1 where z-axis is normal to the substrates and x-y plane (z=0) coincides with the median. The director $\vec{n}$ is represented by a polar angle $\theta(x,y,z)$ and an azimuthal angle $\phi(x,y,z)$ as shown in Fig. 2-1. It is possible to impose conditions $\partial\theta/\partial x = \partial\theta/\partial y = 0$ and $\partial\phi/\partial x = \partial\phi/\partial y = \partial\phi/\partial z = 0$ when the subject in the present analysis is concerned in non-twisted nematic liquid crystals. Moreover, x- and y-axes can be chosen to satisfy the condition $\phi = 0°$. Therefore, $\vec{n}$

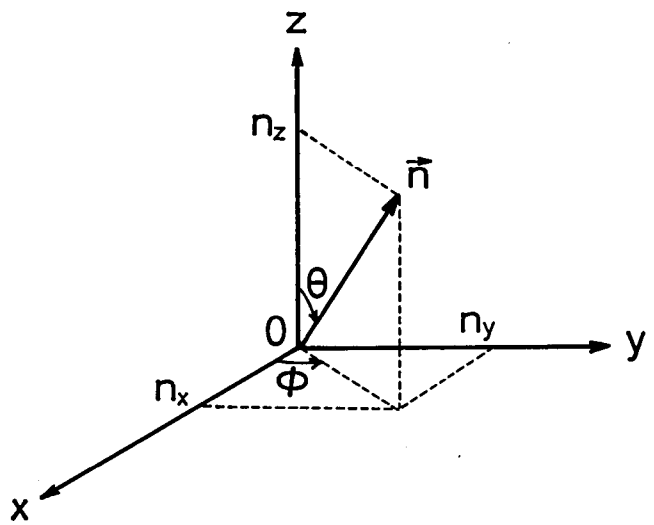

Fig. 2-1 Coordinate system and director angles.

is represented by a single variable function $\theta(z)$ as

$$n_x = \cos\theta(z)$$
$$n_y = 0 \qquad (2\text{-}1)$$
$$n_z = \sin\theta(z) \ .$$

The total free energy W per substrate unit area under a magnetic field $\vec{H}$ in the x direction is represented as a sum of interfacial interaction energy W_s, bulk distortion energy W_d, and magnetic energy W_m. Consequently, we have

$$W = W_s + W_d + W_m \ . \qquad (2\text{-}2)$$

By considering the director distortion under $\vec{H}$, as is shown in Fig. 2-2 and making several assumptions, we derive pertinent formulas for W_s, W_d, and W_m in the following subsections. These assumptions are:

(a) No disclinations exist.

(b) The director angle is constant in the x-y plane, i.e., θ is a single variable function of z.

(c) The angle $\theta(z)$ is symmetric for $z = 0$ and is equivalent with $\theta \pm \pi$.

(d) The differentiation $(d\theta/dz)_{z=0}$ is zero.

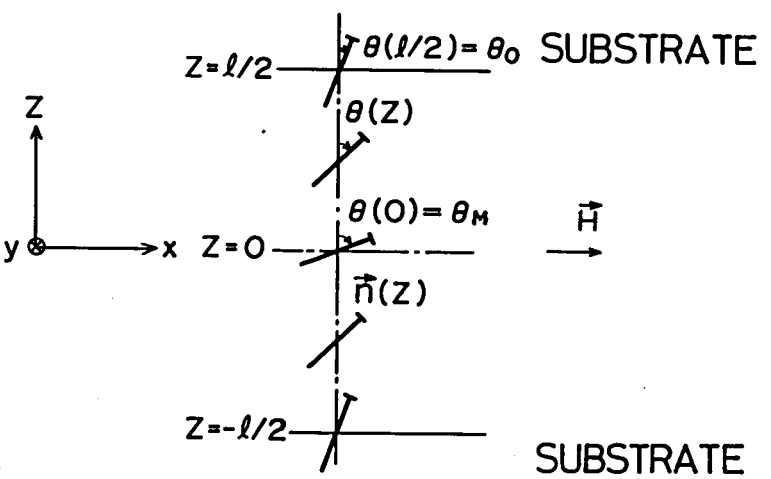

Fig. 2-2 Director distortion under magnetic field $\vec{H}$.

(i) Interfacial interaction energy

In such a situation that poor theoretical or experimental bases exist on the interfacial interaction energy formulation, many workers have introduced W_S in the form[6]

$$W_S = \int g[\,(\vec{n}\cdot\vec{\nu})^2\,]\,dS\,, \tag{2-3}$$

where dS is the interface unit area and $\vec{\nu}$ is the unit normal to the interface. The reason for g being an even function of $\vec{n}$ is that $\vec{n}$ and $-\vec{n}$ are physically the same in the case of liquid crystals. The function g is usually represented as a first approximation by

$$g = A_1\,(\vec{n}\cdot\vec{\nu})^2 + A_2\,, \tag{2-4}$$

where A_1 and A_2 are constants.

By following the above discussions and considering the assumption (b), we make a model for W_S into the form

$$W_S = A/2 + (B_\theta/2)\sin^2(\theta_0-\Theta)\,, \tag{2-5}$$

where A and B_θ are anchoring-strength coefficients, θ_0 is the director polar angle at the interface, $\theta_0 = \theta(\pm\ell/2)$, and Θ is the easy-axis polar angle. Note that the condition $\theta_0 = \Theta$ minimizes W_S. More generally, a term $(B_\phi/2)\int\sin^2(\phi_0-\Phi)\,dS$ should thirdly added for W_S. Here, B_ϕ is another anchoring-strength coefficient, ϕ_0 is the director azimuthal angle at the interface, Φ is the easy-axis azimuthal angle, and $\int dS$ means the surface integral for unit area. In discussions in this section, however, no forces exist to change the director azimuthal angle ϕ. The angle ϕ is usually considered to coincide with Φ. Therefore, this third term can be omitted from Eq. (2-5).

(ii) Bulk distortion energy

Elastic distortion energy in the bulk is obtained by Frank[7] as

$$2W_d = \int \{K_{11}(\mathrm{div}\,\vec{n})^2 + K_{22}(\vec{n}\cdot\mathrm{curl}\,\vec{n})^2 + K_{33}(\vec{n}\times\mathrm{curl}\,\vec{n})^2 + (K_{22}+K_{24})\,[\,Tr(\nabla\vec{n})^2 - (\mathrm{div}\,\vec{n})^2\,]\}\,dV\,, \tag{2-6}$$

where K_{ij}'s are Frank's elastic constants. As the volume integral of the forth term can be rewritten in a surface integral by using the Gauss theory, the forth term deminishes, in the case where the interface is an indefinite plane and $\vec{n}$ is a single variable function of z. When the director is represented by Eq. (2-1) , therefore, W_d is written as

$$W_d = (1/2)\int_{-\ell/2}^{\ell/2} [\, K_{11} (\mathrm{div}\,\vec{n})^2 + K_{33} (\vec{n} \times \mathrm{curl}\,\vec{n})^2 \,] \, dz$$

$$= (1/2)\int_{-\ell/2}^{\ell/2} (K_{11} \sin^2\theta + K_{33}\cos^2\theta)(d\theta/dz)^2 \, dz \, . \qquad (2\text{-}7)$$

(iii) Magnetic energy

By putting the magnetic susceptibility along and across the director, as $\chi_{//}$ and $\chi_{\perp}$, respectively, we can obtain the magnetic energy caused by the external magnetic field $\vec{H}$ (strength H) as

$$W_m = -(1/2)\,\chi_{\perp} H^2 - (1/2)(\chi_{//} - \chi_{\perp})(\vec{n} \cdot \vec{H})^2 \, . \qquad (2\text{-}8)$$

Here, the magnetic flux is assumed to coincide with $\vec{H}$ in their direction, because the magnetic susceptibility of nematic liquid crystals is sufficiently small. By putting

$$\chi_a = \chi_{//} - \chi_{\perp} \, , \qquad (2\text{-}9)$$

we have

$$W_m = -(1/2)\int_{-\ell/2}^{\ell/2} (\chi_{\perp} H^2 + \chi_a H^2 \sin^2\theta)\, dz \, . \qquad (2\text{-}10)$$

By inserting Eqs. (2-5) , (2-7), and (2-10) into Eq. (2-2) , and omitting the θ-independent terms, which need no further consideration, we finally obtain an expression for the total free energy θ-dependent component W_θ :

$$W_\theta = 2\times(1/2)B_\theta \sin^2(\theta_0 - \Theta) + (1/2)\int_{-\ell/2}^{\ell/2} (K_{11}\sin^2\theta + K_{33}\cos^2\theta)(d\theta/dz)^2 \, dz - (1/2)\int_{-\ell/2}^{\ell/2} \chi_a H^2 \sin^2\theta \, dz \, . \qquad (2\text{-}11)$$

2-3. Solution of Euler's Equation

The director distribution obtained under the magnetic field is such that minimizes W_θ for Eq. (2-11) . As W_θ is a functional of $\theta(z)$ and boundary condition $\theta(\pm\ell/2) = \theta_0$ is variable, it is a variation problem with variable boundaries. The procedure to solve this problem is as follows: (i) derive the Euler equation, which is a necessary condition for W_θ to take extremal values, (ii) obtain an extremal pencil, (iii) solve numerically the Euler equation, and (iv) choose W_θ-minimizing $\theta(z)$ out of the extremal pencil by varing θ_0 values for the boundary condition.

As Eq. (2-11) yields

$$\begin{aligned}\delta W_\theta/\delta\theta = & -(1/2)(K_{11}-K_{33})\sin^2(d\theta/dz)^2 \\ & -(K_{11}\sin^2\theta + K_{33}\cos^2\theta)(d^2\theta/dz^2) \\ & + (1/2)\chi_a H^2 \sin^2\theta \\ = & \ 0 \ , \end{aligned} \tag{2-12}$$

the multiplication of $2(d\theta/dz)$ and the application of a relation $2(d\theta/dz)(d^2\theta/dz^2) = (d/dz)(d\theta/dz)^2$ lead to the Euler equation

$$\begin{aligned}&(d/dz)[(1+K\sin^2\theta)(d\theta/dz)^2] \\ &\quad + (1/\xi_0{}^2)\sin 2\theta\,(d\theta/dz) = 0 \ , \end{aligned} \tag{2-13}$$

where $K = K_{11}/K_{33} - 1$ and $\xi_0 = (K_{33}/\chi_a)^{1/2}(1/H)$. Further, the integration of Eq. (2-13) yields

$$\xi_0{}^2(1+K\sin^2\theta)(d\theta/dz)^2 + \sin^2\theta = \text{constant} \ . \tag{2-14}$$

By putting the integral constant as $1/k^2$, and inserting the conditions $\theta(0) = \theta_M$ and $(d\theta/dz)_{z=0} = 0$ at $z = 0$, we have $1/k^2 = \sin^2\theta_M$. Thus, we obtain the Euler equation

$$\xi_0{}^2(1+K\sin^2\theta)(d\theta/dz)^2 = \sin^2\theta_M - \sin^2\theta \ , \tag{2-15}$$

that is,

$$d\theta/dz = \pm(1/k\xi_0)[(1-k^2\sin^2\theta)/(1+K\sin^2\theta)]^{1/2} . \tag{2-16}$$

For further consideration, the + sign case in Eq. (2-16) is omitted for the following reason. By use of a relation $1 + K \sin^2 \theta = (1/K_{33}) (K_{11} \sin^2\theta + K_{33} \cos^2 \theta) > 0$, Eq. (2-15) leads to an inequality

$$\sin^2 \theta_M - \sin^2 \theta = \sin(\theta_M + \theta) \sin (\theta_M - \theta) \geqq 0 \ . \qquad (2\text{-}17)$$

The θ and θ_M region, which satisfies the inequality (2-17) with a fixed θ_0, is shown in Fig. 2-3 . Regions A and B in Fig. 2-3 correspond to the cases $\theta_0 \leqq \theta \leqq \theta_M$ ($|\theta_0| \leqq \theta_M \leqq \pi/2$) and $\theta_M \leqq \theta \leqq \theta_0$ ($-\pi/2 \leqq \theta_M \leqq -|\theta_0|$) , respectively. Director distributions for cases

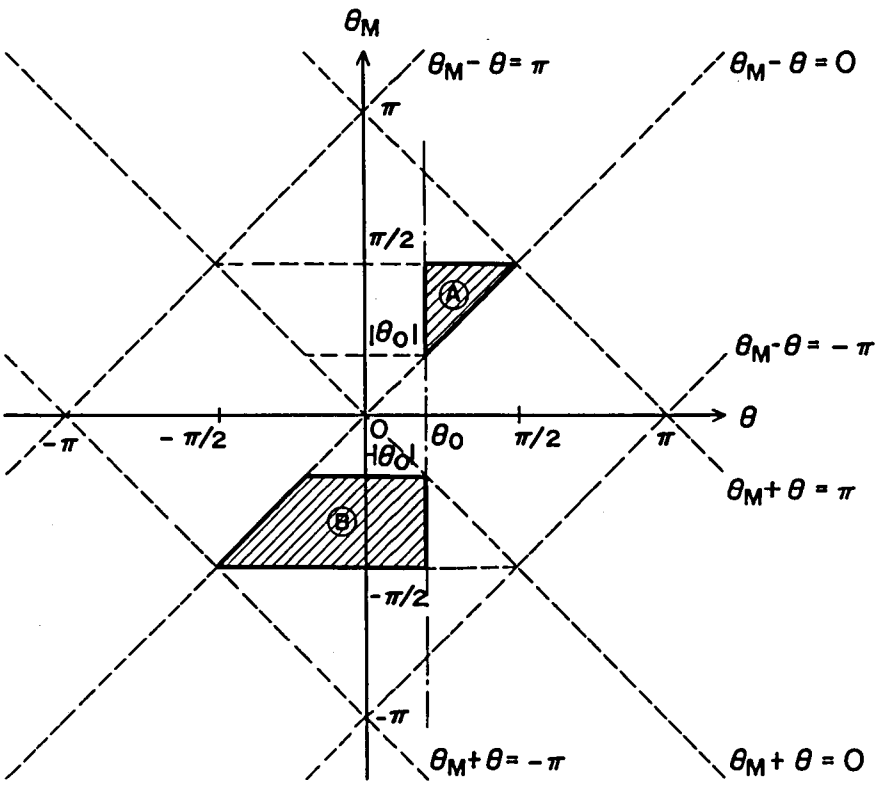

Fig. 2-3 Director angle θ existing region satisfying an inequality $\sin(\theta_M + \theta) \sin(\theta_M - \theta) \geqq 0$.

A and B are illustrated in Fig. 2-4 . As a relation $(1/2)\int_{-\ell/2}^{\ell/2} dz = \int_{0}^{\ell/2} dz$ is derived from the assumption (c), only the region $0 \leqq z \leqq \ell/2$ is considered in the following. In Fig. 2-4 , A and B correspond to the cases $d\theta/dz < 0$ and $d\theta/dz > 0$ in Eq. (2-16) , respectively. The distortion energy for case B, however, is easily obtained by changing θ_0 for case A into $-\theta_0$. Therefore, only case A is considered, where Eq. (2-16) takes the minus sign.

In case A in Fig. 2-4 , where $d\theta/dz < 0$, integrating Eq. (2-16) yields

$$(1/k\xi_0)(\ell/2 - z) = \int_{\theta_0}^{\theta} [(1 + K\sin^2\theta)/(1 - k^2\sin^2\theta)]^{1/2} d\theta \ . \tag{2-18}$$

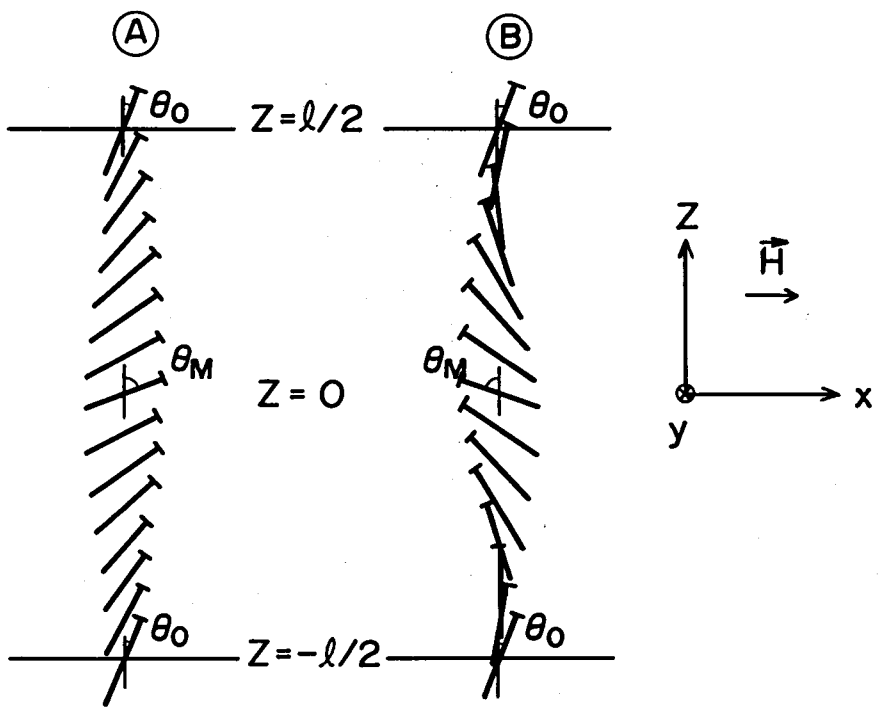

Fig. 2-4 Director distribution cor case A and B in Fig. 2-3 .

By using the foregoing relation $\xi_0 = (K_{33}/\chi_a)^{1/2}(1/H)$ and introducing a critical field strength

$$H_C = (\pi/\ell)(K_{33}/\chi_a)^{1/2} \quad , \tag{2-19}$$

we may write Eq. (2-18) as

$$(1 - 2z/\ell)(\pi/2k)(H/H_C) = \int_{\theta_0}^{\theta} [(1 + K\sin^2\theta)/(1 - k^2\sin^2\theta)]^{1/2}\, d\theta . \tag{2-20}$$

Moreover, by transforming the variable, $\sin\zeta = \sin\theta/\sin\theta_M$ and $\sin\zeta_0 = \sin\theta_0/\sin\theta_M$, we can reduce Eq. (2-20) to

$$(1 - 2z/\ell)(H/H_C) = (2/\pi)[F(\zeta,k) - F(\zeta_0,k)] , \tag{2-21}$$

where

$$F(\zeta,k) = \int_0^{\zeta} [(k^2 + K\sin^2\zeta)/(k^2 - \sin^2\zeta)]^{1/2}\, d\zeta . \tag{2-22}$$

The function $F(\zeta,k)$, given by Eq. (2-22), becomes an elliptic integral of the first kind in the elastically isotropic case, $K = 0$, and then $F(\pi/2,k)$ becomes a complete elliptic integral of the first kind. Insertion of a boundary condition $\zeta = \pi/2$ ($\theta = \theta_M$) at $z = 0$ into Eq. (2-21) finally gives the Euler equation

$$h = (2/\pi)[F(\pi/2,k) - F(\zeta_0,k)] . \tag{2-23}$$

Here, h is H/H_C and H_C, given by Eq. (2-19), means a critical magnetic-field strength under $\Theta = 0°$ and $B_\theta = \infty$ boundary conditions.

As Eq. (2-23) gives relationships among h ($h = H/H_C$), k ($1/k^2 = \sin^2\theta_M$), and ζ_0 ($\sin\zeta_0 = \sin\theta_0/\sin\theta_M$) for fixed K values, we can obtain the relationships between θ_M and H for various θ_0 values. As an example of numerical solutions of Eq. (2-23), the relationships between θ_M and h are obtained for several θ_0 values and shown in Fig. 2-5. As compared with the $K = 0$ case, which is shown in Fig. 2-5, θ_M vs h curves steepness decreases (increases) for the $K > 0$ ($K < 0$) case. As is shown in Fig. 2-5, the Euler equation (2-23) generally has three solutions θ_{Mi} ($i = 1,2,3$) for one pair of h and θ_0 values.

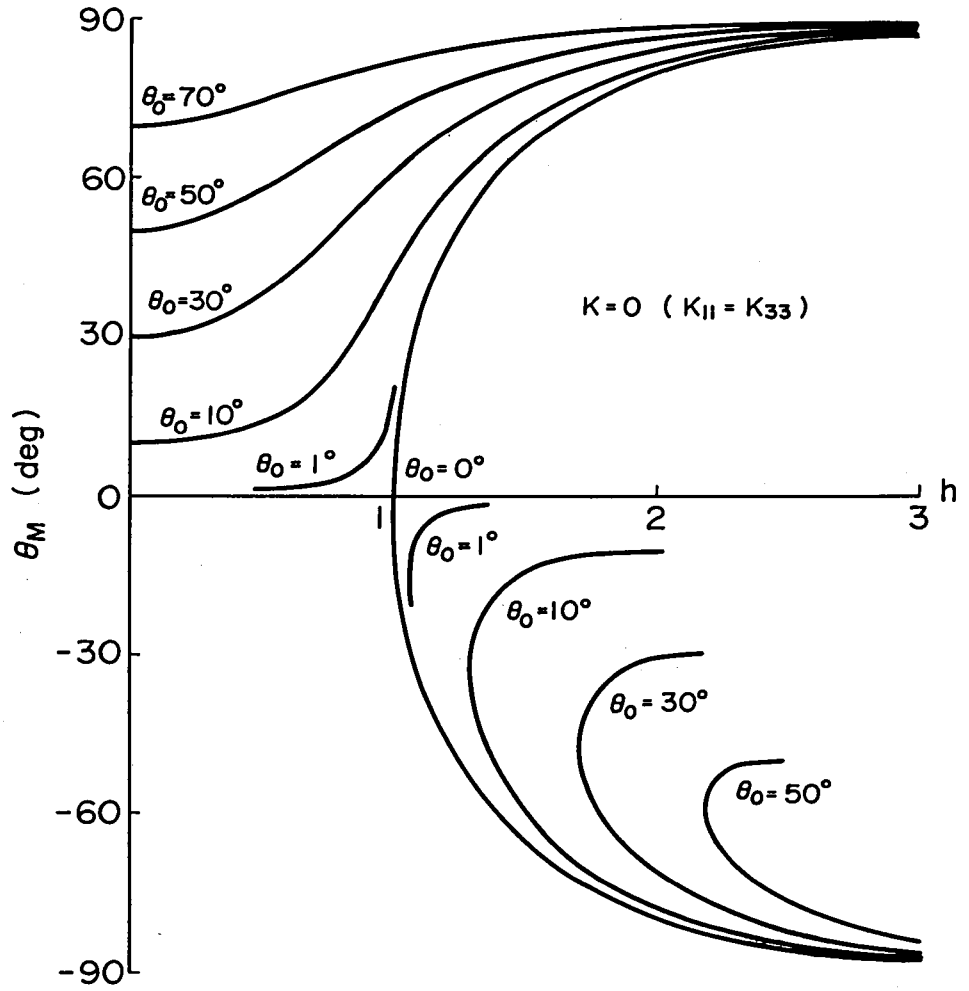

Fig. 2-5 Euler-equation example solutions.

Because the Euler equation gives only a necessary condition, it is necessary to check which θ_{Mi} makes W_θ minimum.

Insertion of Eq. (2-16) ($d\theta/dz < 0$) into Eq. (2-11) yields W_θ as a function of θ_0,

$$W_\theta = B_\theta \sin^2(\theta_0 - \Theta) + (\ell/2)\chi_a H^2 \{ \int_{\theta_0}^{\theta_M} [(1 + K \sin^2\theta) (1/k^2 - \sin^2\theta)]^{1/2} d\theta$$

$$-\int_{\theta_0}^{\theta_M}[(1+K\sin^2\theta)/(1/k^2-\sin^2\theta)]^{1/2}\sin^2\theta\,d\theta\}$$

$$/\int_{\theta_0}^{\theta_M}[(1+K\sin^2\theta)/(1/k^2-\sin^2\theta)]^{1/2}\,d\theta \quad . \qquad (2\text{-}24)$$

Furthermore, the foregoing variable transformation yields

$$W_\theta = B_\theta \sin^2(\theta_0-\Theta) + (K_{33}/\xi_0 k^2)\{(\ell/2\xi_0) - 2[F'(\pi/2,k) - F'(\zeta_0,k)]\} , \qquad (2\text{-}25)$$

where

$$F'(\zeta,k) = \zeta_0[(k^2+K\sin^2\zeta)/(k^2-\sin^2\zeta)]^{1/2}\sin^2\zeta\,d\zeta \quad . \qquad (2\text{-}26)$$

Now, we consider how W_θ in Eq. (2-25) changes according to θ_M. As an example, the case of $h = 1.5$ and $\theta_0 = 10°$ is considered. The solution of the Euler equation (2-23) for the condition $\theta_0 = 10°$ is again shown in Fig. 2-6, for use in explaining the three possible solutions θ_{Mi} for $h = 1.5$. The θ_M-dependence of W_θ is calculated from Eq. (2-25) and shown in Fig. 2-7. Figure 2-7 shows that θ_{M1} and θ_{M3} make W_θ minimum. When increasing h from zero value, as is shown in Fig. 2-6, the situation $\theta_M = \theta_{M1}$ is thought to be realized rather than the situation $\theta_M = \theta_{M3}$. Thus, the solutions in the region $\theta_M \geqq 0$ in Fig. 2-5 are found to make W_θ minimum.

As the last step, it is necessary to determine a θ_0 value, which minimizes W_θ for an arbitrary h. As the θ_0-dependence of θ_M for arbitrary h is obtained by Eq. (2-23), Eq. (2-25) together with Eq. (2-23) gives the relationship between W_θ and θ_0 for arbitrary h under a fixed pair of anchoring parameters, Θ and B_θ. As an example, calculated relationship between W_θ and θ_0 in $h = 1.0$ case is shown in Fig. 2-8. Here, a normalized coefficient β,

$$\beta = (2/\pi)(B_\theta/2)/(K_{33}/\ell) , \qquad (2\text{-}27)$$

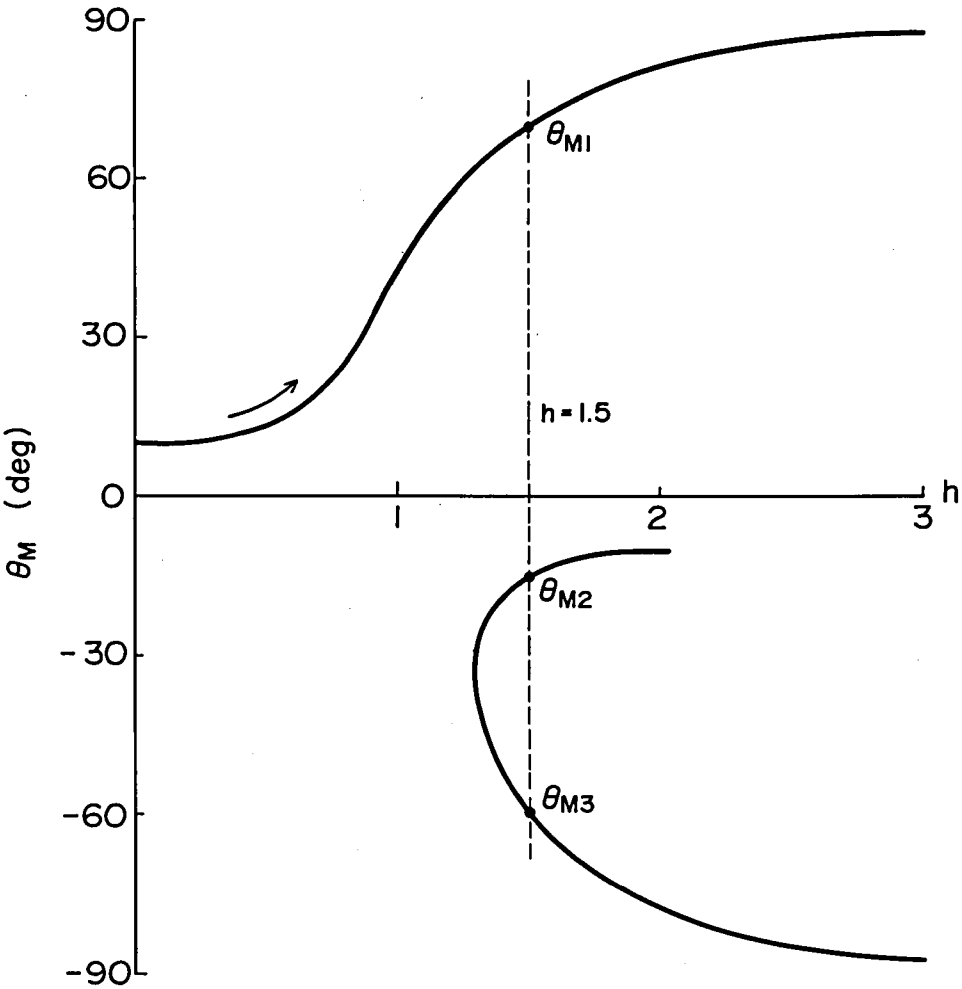

Fig. 2-6 Euler-equation solution for $\theta_0 = 10°$, showing three possible solutions θ_{Mi}.

is introduced instead of the anchoring-strength coefficient B_θ. Figure 2-8 shows that W_θ becomes minimum for $\theta_0 = 56°$ in $h = 1.0$ case, and then θ_M is obtained as 78° from Eq. (2-23) (in $\Theta = 10°$ and $\beta = 1.0$ case). As a conclusion, by using the numerical calculations mentioned in this section, we can obtain the director distribution under variable magnetic field h for each pair of anchoring parameters, Θ and B_θ.

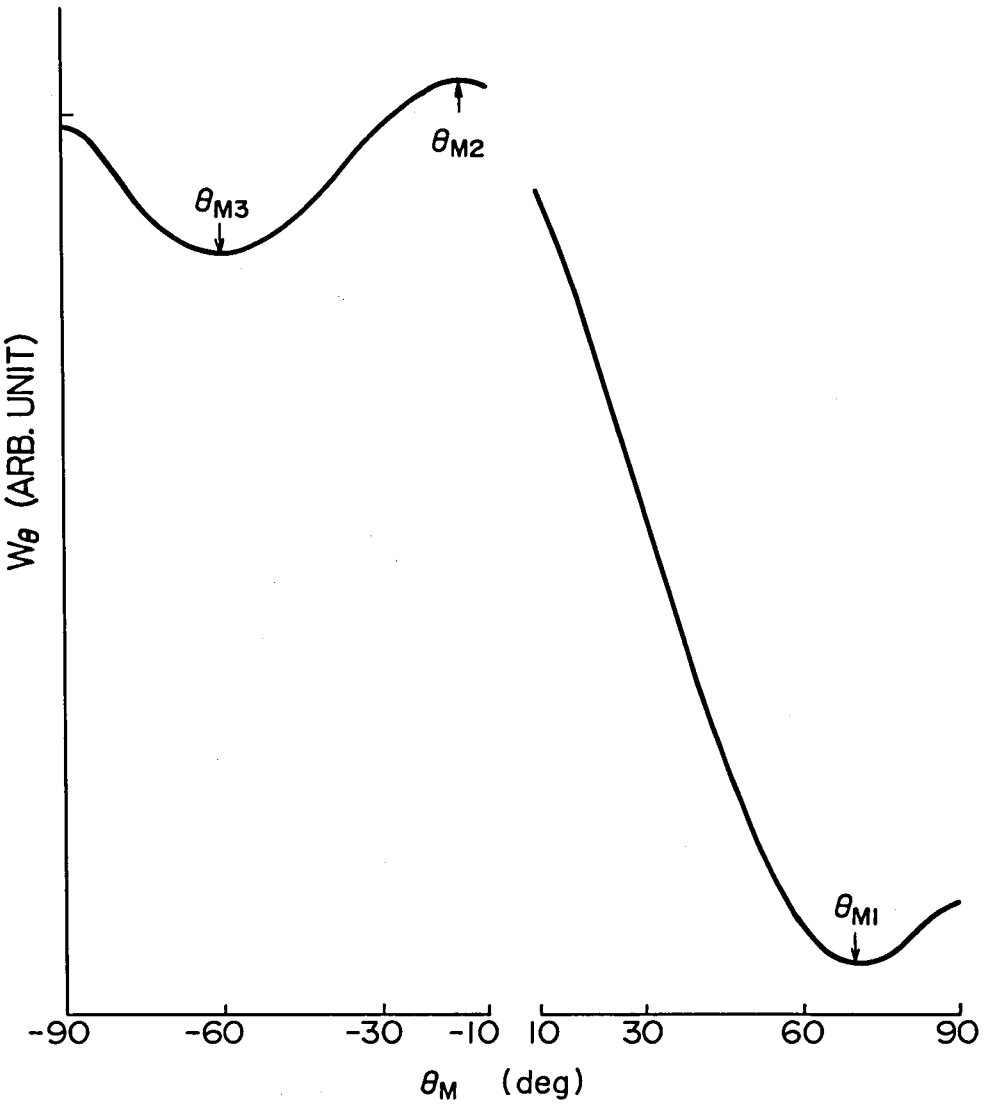

Fig. 2-7 Median alignment angle (θ_M) dependence of total free energy W_θ, when $\theta_0 = 10°$ and $h = 1.5$.

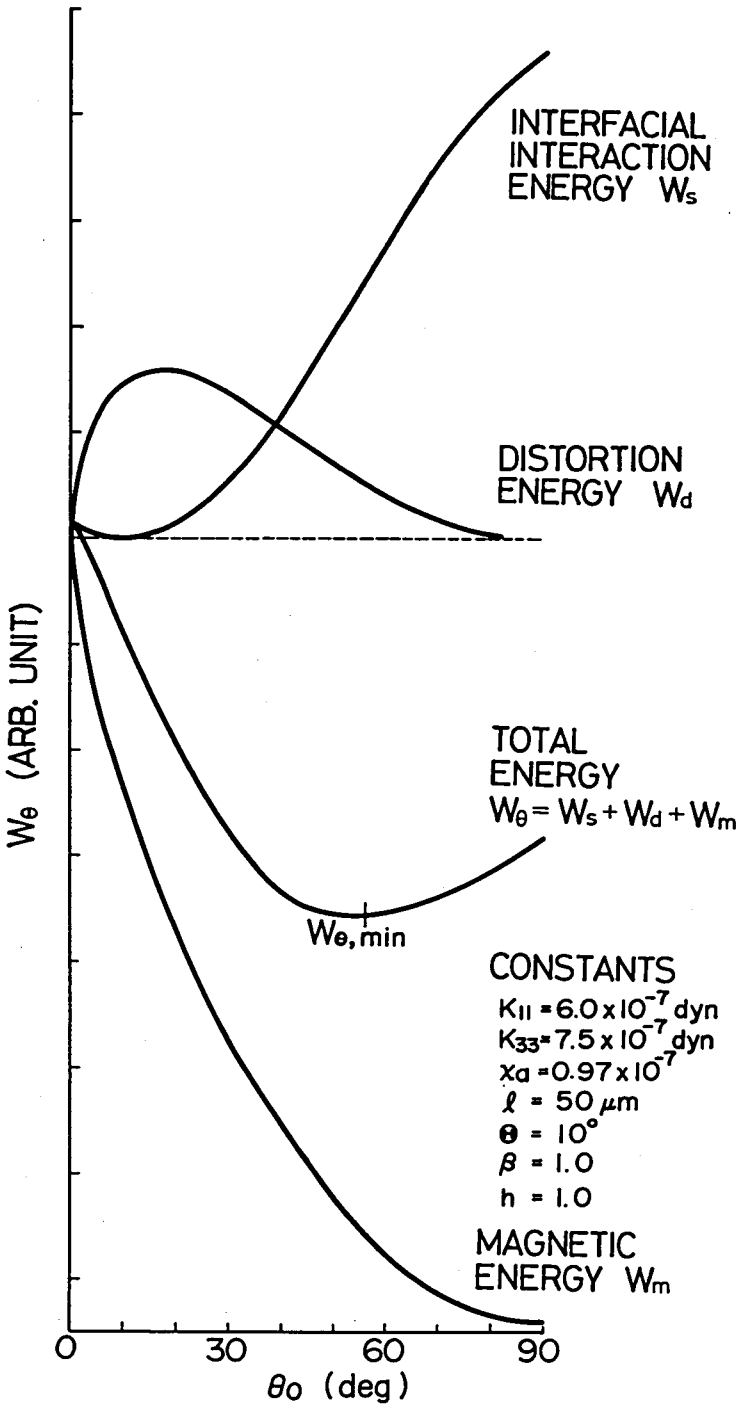

Fig. 2-8 Interfacial alignment angle (θ_0) dependence of total free energy W_θ, when $h = 1.0$.

2-4. Wall Effects Consideration

In this section, the anchoring parameters B_θ and Θ effects on the (θ_0, θ_M) vs h curves are considered. First, the β effects are considered, which correspond to the B_θ effects. As an example, (θ_0, θ_M) vs h curves are derived for six β values under $\Theta = 10°$ condition, and are shown in Fig. 2-9 . In the case of $\beta = \infty$, the interfacial alignment angle θ_0 stays constant and equals the easy-axis angle Θ for any h value. Median alignment angle θ_M increases smoothly as h increases. When β value is finite, on the other hand, θ_0 increases as h increases. The θ_M vs h curve becomes steeper and the differences between θ_0 and θ_M become smaller as β decreases. The director distortion in the bulk, therefore, deminishes as β decreases. This feature is illustrated for $h = 1.0$ case in the insert in Fig. 2-9 . When β is as small as 0.1 , almost no distortions occur in the bulk. In the finite case of $\beta = 0$, both θ_0 and θ_M become $\pi/2$, even under an extremely small magnetic field, that is, all the director align parallel to the magnetic field. These β-dependence features of θ slightly depend on Θ values. As an example, θ_0 vs h and θ_M vs h curves for the $\Theta = 0°$, $10°$, and $30°$ cases are shown in Fig. 2-10 . Thus, the Freedericksz transition is greatly affected by β values, and is classified into three cases. The first is where the interfacial alignment angle θ_0 is not affected by the external magnetic field and equals the easy-axis angle Θ, which is realized when $\beta \gtrsim 10^2$. In this case, the wall effect, corresponding to the first term in the right side of Eq. (2-25) , works as a constant boundary condition $\theta_0 = \Theta$, and the curves in the $\theta_M \geqq 0$ region in Fig. 2-5 , which are the solutions of the Euler equation (2-23), represent the θ_M vs h curve in the Freedericksz transition. This case, where the condition $\theta_0 = \Theta$ always holds independent of h values, is named by de Gennes[8] as a "strong anchoring" state.

A second case in the Freedericksz transition is where interfa-

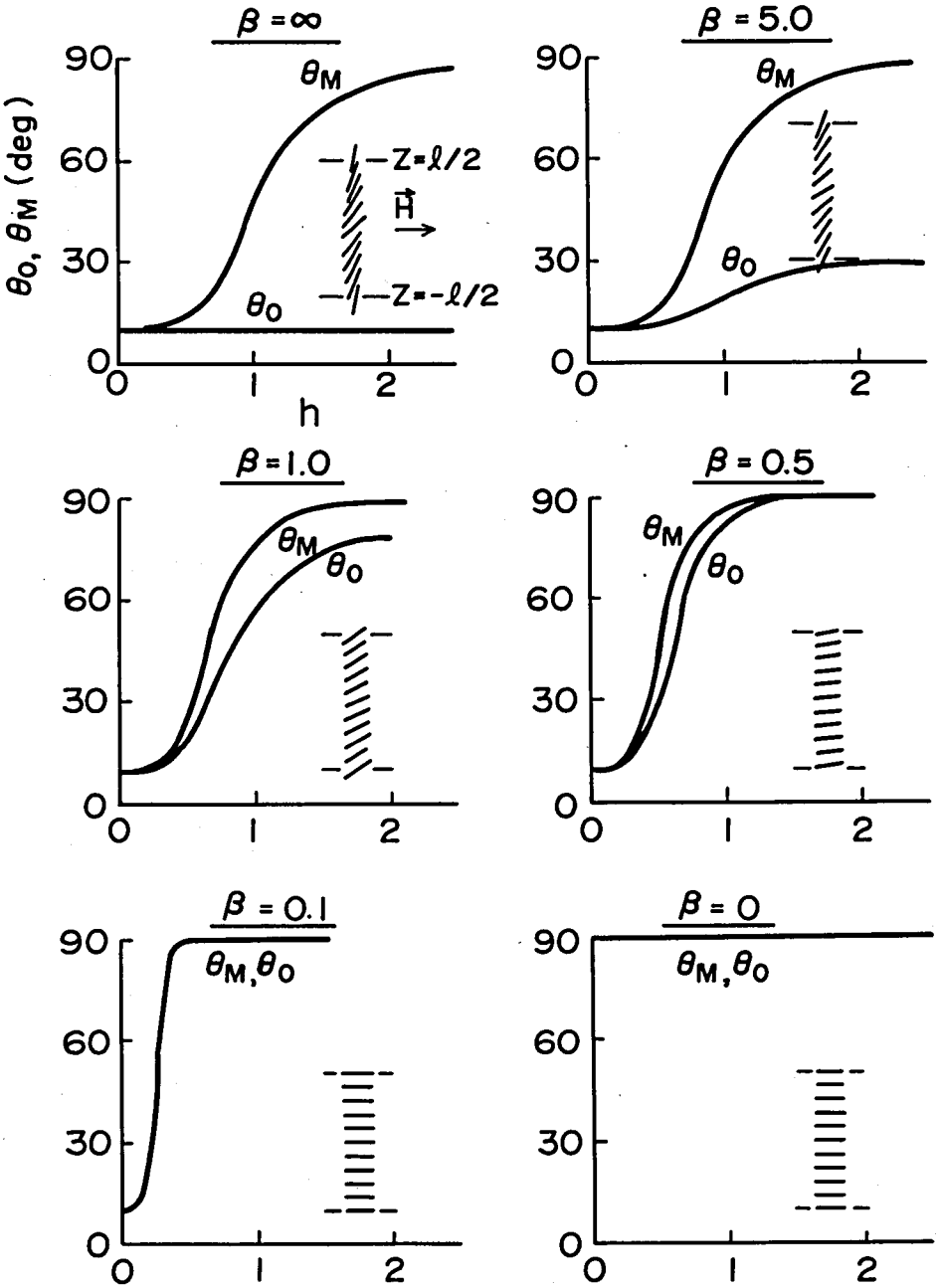

Fig. 2-9 Normalized anchoring strength (β) dependence of Freedericksz transition, when $\Theta = 10°$. (The insert illustrates director distribution for $h = 1.0$.)

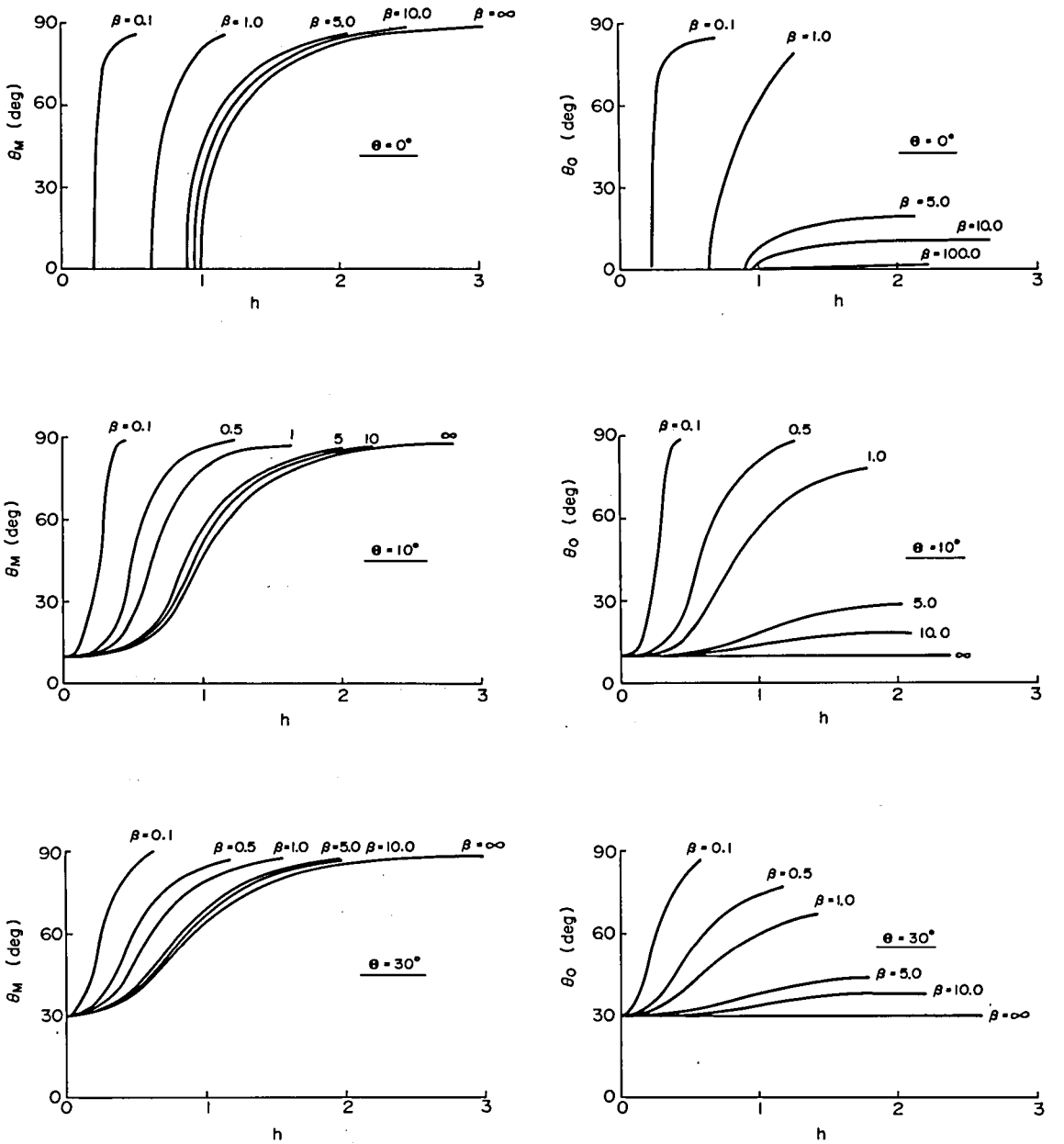

Fig. 2-10 Anchoring parameters (θ,β) dependence of Freedericksz transition.

cial alignment angle θ_0 changes according to external magnetic field h and director distortions occur in the bulk. This occurs for $10^{-1} < \beta < 10^2$ and is called a "weak anchoring" state.

A third case is where interfacial alignment angle θ_0 changes according to magnetic field h and nearly equals θ_M, that is $\theta(z) =$ constant $\neq \Theta$. This case, where no director distortions occur in the bulk, occurs for $\beta \lesssim 10^{-1}$ and is called a "free anchoring" state. This classification of the Freedericksz transition according to the anchoring condition is summarized in Table 2-1.

Table 2-1 Freedericksz-transition classification according to boundary conditions.

	I	II	III
ANCHORING CONDITION	STRONG ANCHORING	WEAK ANCHORING	FREE ANCHORING
β $(= \ell B_\theta / \pi K_{33})$	$\beta \gtrsim 10^2$	$10^{-1} < \beta < 10^2$	$\beta \leq 10^{-1}$
INTERFACIAL ALIGNMENT ANGLE θ_0	$\theta_0 = \Theta$	$\Theta < \theta_0 < \theta_M$	$\theta_0 = \theta_M$
DISTORTION $d\theta/dz$	FINITE	FINITE	$d\theta/dz = 0$

Next, consider the easy-axis angle Θ effects on the Freedericksz transition. The calculated results in Fig. 2-10, with several additional calculations, are shown in Fig. 2-11 in such forms as to illustrate clearly the Θ-dependence. Figure 2-11(a) represents how θ_M vs h curves change according to Θ values for the "strong anchoring ($\beta = \infty$)" case. In Fig. 2-11(a), a critical phenomenon is found to exist only when $\Theta = 0°$, and, in $\Theta \neq 0°$ cases, θ_M changes continuously, even under a weak magnetic field. Figure 2-11(b) shows the Θ dependence of (θ_0, θ_M) vs h curves for a "free anchoring ($\beta \simeq 0.1$)" case. In this case, too, the raising feature of θ vs h curves becomes smooth as Θ increases.

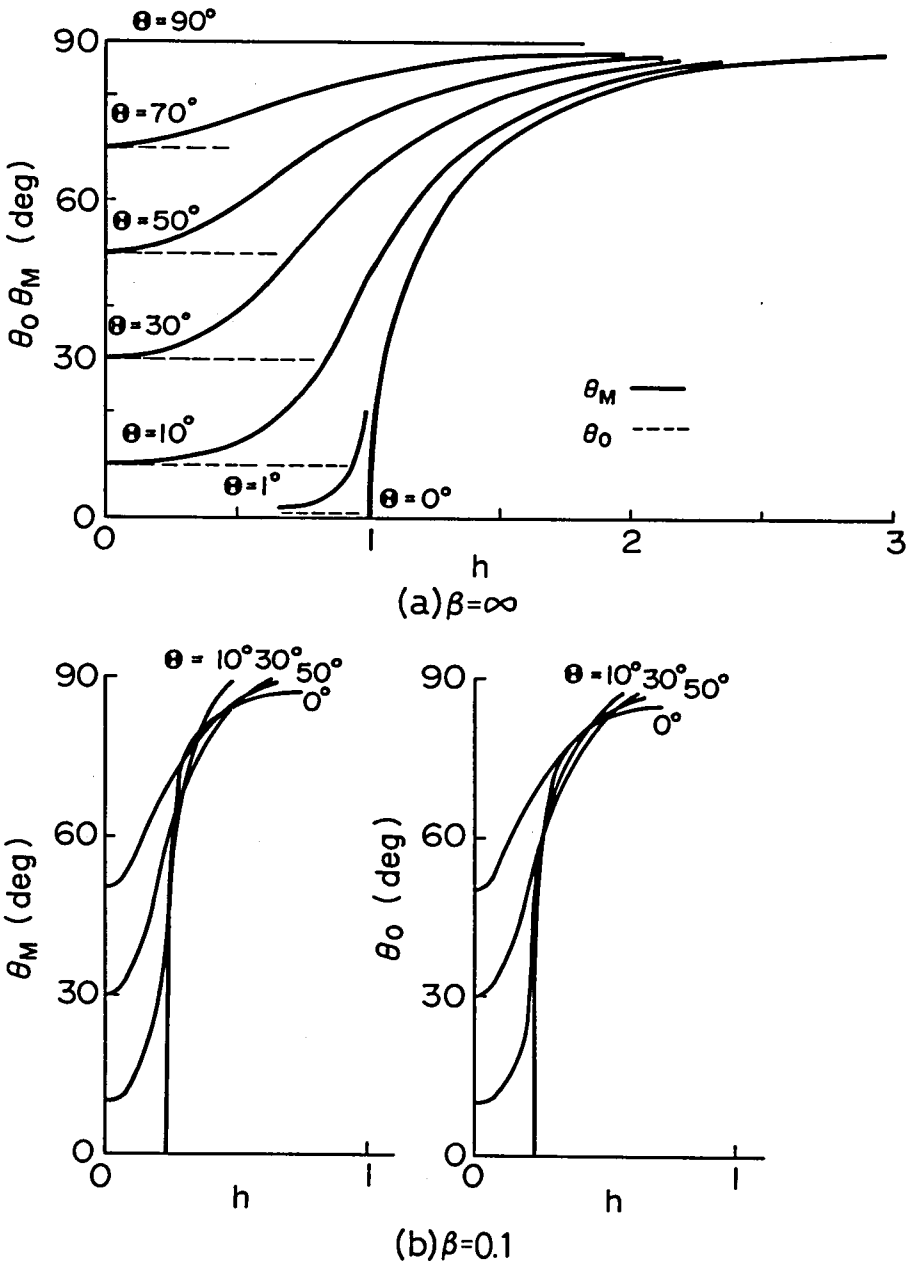

Fig. 2-11 Easy-axis angle (Θ) dependence of Freedericksz transition for $\beta = \infty$ (strong anchoring) and $\beta = 0.1$ (weak anchoring).

As clarified in the above considerations, either decreasing β or increasing Θ makes the Freedericksz-transition critical phenomena vague and the critical magnetic-field strength for the transition small. These effects become clearer by considering the β dependence for normalized critical field strength h_c, which is a ratio of the critical field strength H_c' and that in $\beta = \infty$ ($\Theta = 0°$) case, H_c.

The relationships between β and h_c are derived from θ vs h curves for various β values. In the case of $\Theta \neq 0°$, when the critical transition diminishes, h_c is defined by the intercept of a tangent of θ vs h curve and the line $\theta = \Theta$. As an example, the β-dependence of h_c is derived for $\Theta = 0°$, 10°, and 30° cases ($K = K_{11}/K_{33} - 1 = 0.2$), and is shown in Fig. 2-12. In the case of $\Theta = 0°$, h_c is calculated[5] as

$$h_c = \beta \cot(\pi h_c/2) \qquad (2\text{-}28)$$

by using a one-constant approximation ($K_{11} = K_{33}$, that is, $K = 0$). This relationship is also shown in Fig. 2-12 by a broken line. In this $\Theta = 0°$ case, the elastic anisotropy does not have too much effect and the one-constant approximation gives a fairly good approximation.

As is clearly shown in Fig. 2-12, the critical field strength for the Freedericksz transition is strongly affected by the anchoring parameters, Θ and B_θ. This fact gives a method to derive the anchoring-strength coefficient B_θ experimentally from measured Θ and h_c.

2-5. Summary

In this section, a theoretical basis for deriving the anchoring strength at liquid-crystal substrate interfaces has been presented.

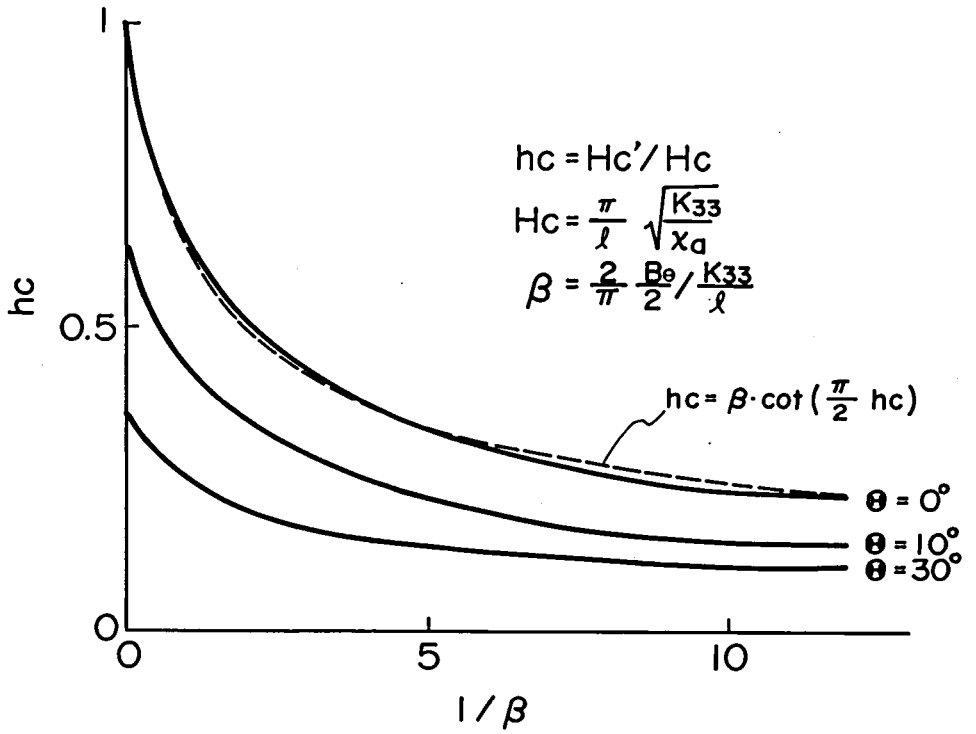

Fig. 2-12 Normarized anchoring strength (β) dependence of critical field-strength for Freedericksz transition.

1) Two parameters, easy-axis angle Θ and anchoring-strength coefficient B_θ, have been introduced to characterize the interfacial interaction energy.

2) A pertinent formula has been given to the total free energy for a nematic liquid-crystal layer between parallel substrates by expressing the interfacial energy properly.

3) The Freedericksz transition has been analyzed for various anchoring-parameter values, Θ and B_θ, by solving the Euler equation for the total free energy formula.

4) Threshold field strength H_c' for the Freedericksz transition has

been found to decrease with increasing Θ or decreasing B_θ .

5) It has been demonstrated that B_θ value can be derived by measuring Θ and H_c' and using the calculated relationships between H_c' and anchoring parameters, Θ and B_θ .

References

[1] V. K. Freedericksz and V. Zolina, Trans. Faraday Soc., 29, 919 (1933)

[2] H. Zocher, Trans. Faraday Soc., 29, 945 (1933)

[3] A. Rapini, M. Papoular, and P. Pincus, Compt. Rend. Acad. Sc. Paris, 267B, 1230 (1968)

[4] D. Meyerhofer, Phys. Lett., A51, 407 (1975)

[5] A. Rapini and M. Papoular, J. Phys. (Paris), C4-30, C4-54, (1969)

[6] J. L. Ericksen, Quart. J. Mech. Appl. Math., 27, 213 (1974)

[7] F. C. Frank, Disc. Faraday Soc., 25, 19 (1958)

[8] P. G. de Gennes, *The Physics of Liquid Crystals* (Oxford University, London, 1974)

III. PRINCIPLES OF INTERFACIAL ALIGNMENT ANGLE AND THE FREEDERICKSZ-TRANSITION MEASUREMENTS

3-1. Introduction

Section II showed the results of analyzing the wall effects on the Freedericksz transition. These results show that measuring easy-axis angle Θ and critical field strength H_c' for the Freedericksz transition enables deriving liquid-crystal anchoring-strength coefficient B_θ. The discussions in Section II stand on the assumption that no director distortion exists when there is no external magnetic field. In general, however, there are three possible director distributions, according to $d\theta/dz < 0$, $d\theta/dz > 0$, and $d\theta/dz = 0$, as shown in Fig. 3-1. The director distribution in case (c) is energetically most stable, because no elastic distortion energy exists. Then, interfacial alignment angle θ_0 is considered to equal Θ, so

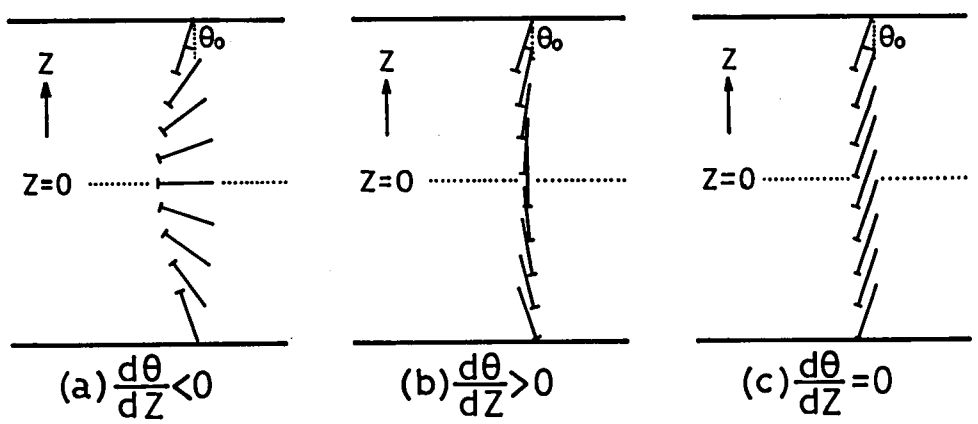

Fig. 3-1 Possible alignment for nematic liquid-crystal molecules under no external fields. (a) and (b) are distorted configuration and (c) is homogeneously tilted configuration.

as to minimize interfacial energy. Thus, in case (c), Θ value is easily obtained by the interfacial alignment angle θ_0 measurements. Then, the B_θ - deriving method, mentioned in Section II, is applicable. On the other hand, in cases (a) and (b), θ_0 does not necessarily equal Θ, because the director distribution is subject to the competition between the interfacial energy, caused by the discrepancy between θ_0 and Θ, and the bulk elastic distortion energy. The discrepancy between θ_0 and Θ can occur in such cases as field induced alignment or quasi-stable alignment after field removal. The discrepancy between θ_0 and Θ is determined by magnitudes of both anchoring-strength coefficient B_θ and Frank's elastic constants K_{11} and K_{33}. Consequently, in cases (a) and (b), Θ measurements cannot be performed independently from B_θ measurements. Although Θ can be determined only for case (c), measured θ_0 values, even in cases (a) and (b), give information in regard to $\Theta \leqq \theta_0$ (case(a)) or $\Theta \geqq \theta_0$ (case (b)) concerning easy-axis angle Θ. Consequently, it is desirable to develop a θ_0 - measuring method applicable for case (a), (b) or (c) in Fig. 3-1. At least, it is necessary to confirm which kind of director distribution is realized in a sample liquid-crystal cell.

Several methods have been reported concerning alignment angle measurements for uniformly aligned directors (Fig. 3-1(c)), including crystal-rotation method[1-5], optical phase-retardation method[6], electric-capacitance method[4], and magnetic null method[7,8]. All of these existing methods are useless, when the director distribution is in a distorted form, such as (a) or (b) in Fig. 3-1. Moreover, those methods, based on electric capacitance measurements, are not applicable for insulating substrate cases.

On the other hand, the Freedericksz transition is usually observed through the electric capacitance change caused by the director realignment. In the Freedericksz-transition measurement, too, the existing method cannot be applied for insulating substrate samples.

In this section, new methods are introduced for both interfacial alignment angle and the Freedericksz-transition measurements. Section 3-2 describes the principles of newly developed methods for interfacial alignment angle measurements. They are magneto-capacitance method, which is applicable even for distorted director distributions, and total-reflection method, which is applicable even for insulating glass-substrate samples. In Section 3-3, the Freedericksz-transition measurements principles are given, including the conventional magneto-capacitance method and the newly developed total-reflection method. In Section 3-4, the present methods are summarized in contrast to the conventional methods.

3-2. Principle of Interfacial Alignment Angle Measurements

3-2-1. Magneto-capacitance method

The angle between liquid-crystal molecules and a substrate normal at the substrate surface is defined as θ_0 . Again, note that θ_0 does not necessarily equal the easy-axis angle Θ , which means the interfacial alignment angle corresponding to minimum interfacial energy. The angle θ_0 is determined by magneto-capacitance measurements, as described in the following.

The coordinate system is the same as that used in Section II . Again it is shown in Fig. 3-2 accompanied with a magnetic field notation. The substrate surface is parallel to the x-y plane. As x- and y-axes are chosen to satisfy the condition $\phi = 0°$ and a condition $\partial\theta/\partial x = \partial\theta/\partial y = 0$ is imposed, director $\vec{n}$ is represented using a single-variable function $\theta(z)$. In this section, three possible distributions of $\vec{n}$ in Fig. 3-1 are considered.

In order to perform a precise analysis of director distributions,

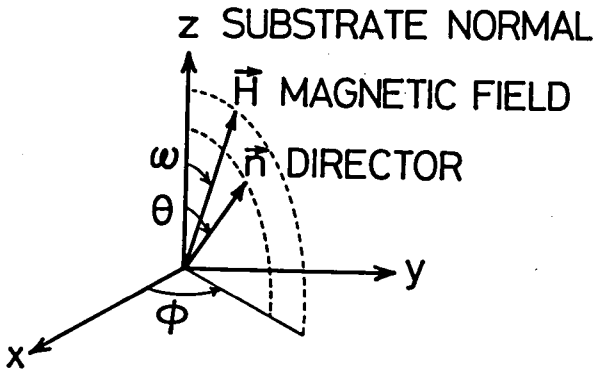

Fig. 3-2 Coordinate system and angles for director and magnetic field.

when there is no external field, anchoring strengths should be considered for cases (a) and (b) in Fig. 3-1. As the B_θ derivation, based on the method mentioned in Section II, is limited for case (c), a strong anchoring condition is assumed for simplicity in further considerations on cases (a) and (b). This assumption does not affect clarification of director distributions (a), (b) or (c).

In cases (a) and (b) in Fig. 3-1 under the strong anchoring approximation, $\theta(z)$ is obtained by solving the Euler equation only for a bulk energy density functional W_d (see Eq. (2-7)),

$$W_d = \int_0^{\ell/2} (K_{11} \sin^2\theta + K_{33} \cos^2\theta) (d\theta/dz)^2 dz \ , \qquad (3\text{-}1)$$

with boundary conditions of

$$\theta(0) = \pi/2, \ \theta(\ell/2) = \theta_0 \quad (\text{case(a)}) \ ,$$
$$\theta(0) = 0 \ , \ \theta(\ell/2) = \theta_0 \quad (\text{case(b)}) \ . \qquad (3\text{-}2)$$

Here, K_{11} and K_{33} are Frank's elastic constants and ℓ is the liquid-crystal layer thickness. By use of an approximation $K_{11} = K_{33}$, the Euler equation for Eq. (3-1) leads to

$$d^2\theta/dz^2 = 0 \ , \qquad (3\text{-}3)$$

which gives the following relations, together with boundary condi-

tions (3-2),

$$\theta(z) = (\pi/2)(1 - 2z/\ell) + (2z/\ell)\theta_0 \quad (\text{case(a)}),$$
$$\theta(z) = (2z/\ell)\theta_0 \quad (\text{case(b)}) . \quad (3\text{-}4)$$

In case (c) in Fig. 3-1, it is easily found without any assumption, that

$$\theta(z) = \theta_0 \quad (\text{case(c)}) . \quad (3\text{-}5)$$

The capacitance per unit area, C_0, for a liquid-crystal layer is calculated by substituting the above relations (3-4) and (3-5) into the formula,

$$C_0 = 2\int_0^{\ell/2} (\varepsilon_{//}\cos^2\theta + \varepsilon_{\perp}\sin^2\theta)\, dz , \quad (3\text{-}6)$$

resulting in

$$C_0 = \begin{cases} \ell[\hat{\varepsilon} + (\Delta\varepsilon/2)\sin 2\theta_0/(2\theta_0 - \pi)] & (\text{case(a)}), \\ \ell[\hat{\varepsilon} + (\Delta\varepsilon/2)\sin 2\theta_0/2\theta_0] & (\text{case(b)}), \\ \ell[\hat{\varepsilon} + (\Delta\varepsilon/2)\cos 2\theta_0] & (\text{case(c)}), \end{cases} \quad (3\text{-}7)$$

where $\varepsilon_{//}$ and $\varepsilon_{\perp}$ are dielectric constants parallel and perpendicular to the director, respectively, $\hat{\varepsilon} = (\varepsilon_{//} + \varepsilon_{\perp})/2$, and $\Delta\varepsilon = \varepsilon_{//} - \varepsilon_{\perp}$.

When magnetic field $\vec{H}$ is applied in a plane containing the z-axis and a director $\vec{n}$ (Fig. 3-2), capacitance changes according to the liquid-crystal molecule realignments. When magnitude of $\vec{H}$ is sufficiently large, almost all liquid-crystal molecules, except those in thin transition regions near each substrate, realign in the $\vec{H}$ direction with an angle ω relative to the z-axis. Therefore, the liquid-crystal layer capacitance per unit area under $\vec{H}$ is approximately represented as

$$C_H = \ell(\varepsilon_{//}\cos^2\omega + \varepsilon_{\perp}\sin^2\omega)$$
$$= \ell[\hat{\varepsilon} + (\Delta\varepsilon/2)\cos 2\omega] . \quad (3\text{-}8)$$

From Eqs. (3-7) and (3-8), an angle $\omega = \omega_0$ is obtained which

satisfies $C_H / C_0 = 1$ for each case of (a), (b), and (c).

$$\omega_0 = \begin{cases} (1/2)\arccos[\sin 2\theta_0/(2\theta_0-\pi)] & (\text{case(a)}), \\ (1/2)\arccos(\sin 2\theta_0/2\theta_0) & (\text{case(b)}), \\ \theta_0 & (\text{case(c)}). \end{cases} \quad (3\text{-}9)$$

These relationships between θ_0 and ω_0 are shown in Fig. 3-3. Consequently, if angle ω_0 is found so that there are no capacitance changes under the magnetic field, θ_0 can be determined using Fig. 3-3.

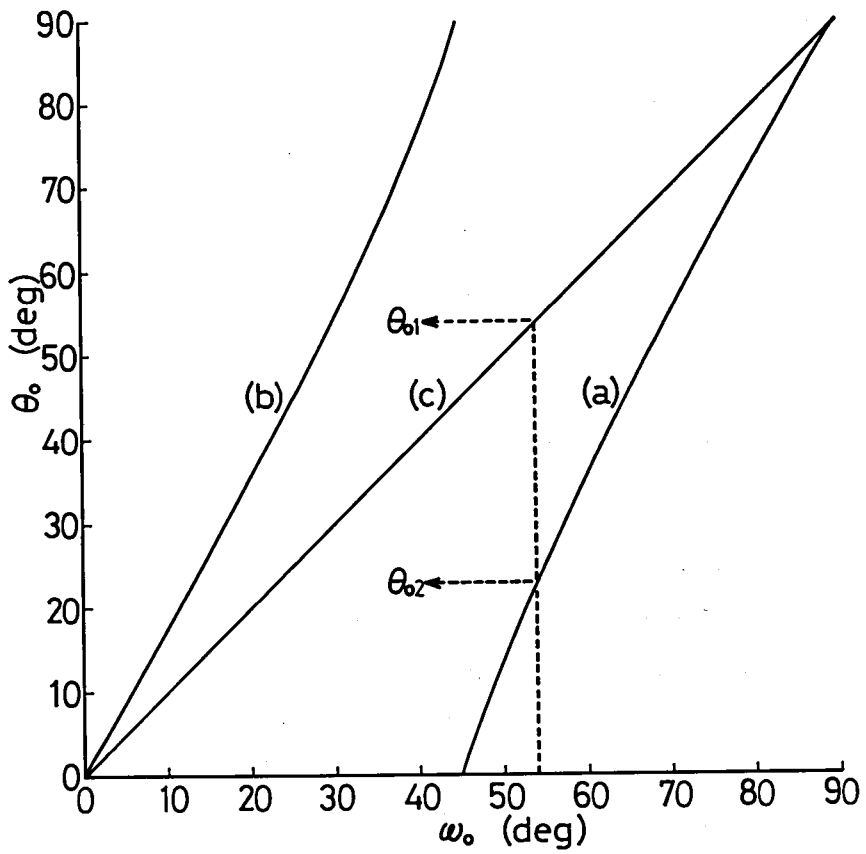

Fig. 3-3 Calculated relationships between interfacial liquid-crystal alignment angle θ_0 and angle ω_0 for applied magnetic field which causes no capacitance change.

Although two different θ_0 values, θ_{01} and θ_{02}, are generally obtained for a measured ω_0 from Fig. 3-3, it is easy to find a physically relevant value of θ_0 from the ω-H characteristics of the liquid-crystal layer capacitance. The principle is based on the fact that θ_{01} is for a uniformly tilted alignment case (c) and θ_{02} is for a distorted alignment case (a) or (b). The uniformly tilted and the distorted alignments have entirely different features from each other and are easily distinguished, as follows. Equation (3-8) was derived under the assumption that applied magnetic field strength H is large enough so that almost all liquid-crystal molecules are parallel to $\vec{H}$ and that the presence of a transition layer can be neglected. When H is not so large, however, different distortion cases exist, according to the sign of ω, as is shown in Fig. 3-4. It is obvious from Fig. 3-4, that, in cases (a) and (b), liquid-crystal layer capacitance C_H values are equal for the two distortion patterns (aI) and (aII), and (bI) and (bII). On the contrary, C_H differs for distortion patterns (cI) and (cII). When the field $\vec{H}$ is rotated, the ω-H characteristics of C_H lack symmetry with respect to $\omega = 0°$ in the uniformly tilted alignment case (c) in Fig. 3-1 which does not possess a mirror symmetry with respect to the x-y plane[9], whereas the ω-H characteristics show symmetry with respect to $\omega = 0°$ in the distorted alignment cases (a) and (b) in Fig. 3-1 which possess a mirror symmetry with respect to the x-y plane.

Some other magneto-capacitance characteristics support distinguishing uniformly tilted and distorted alignments. That is, for uniformly tilted alignment (c), the magnetic field in $-\theta_{01}$ direction causes transient capacitance changes in contrast to the magnetic field in $+\theta_{01}$ direction which causes no capacitance changes. In addition, the magnetic field in $(\theta_{01} - 90°)$ direction causes a critical Freedericksz transition for the uniform alignment case[10]. For distorted alignment cases (a) and (b), however, the liquid-crystal alignment mirror symmetry, with respect to the x-y plane,

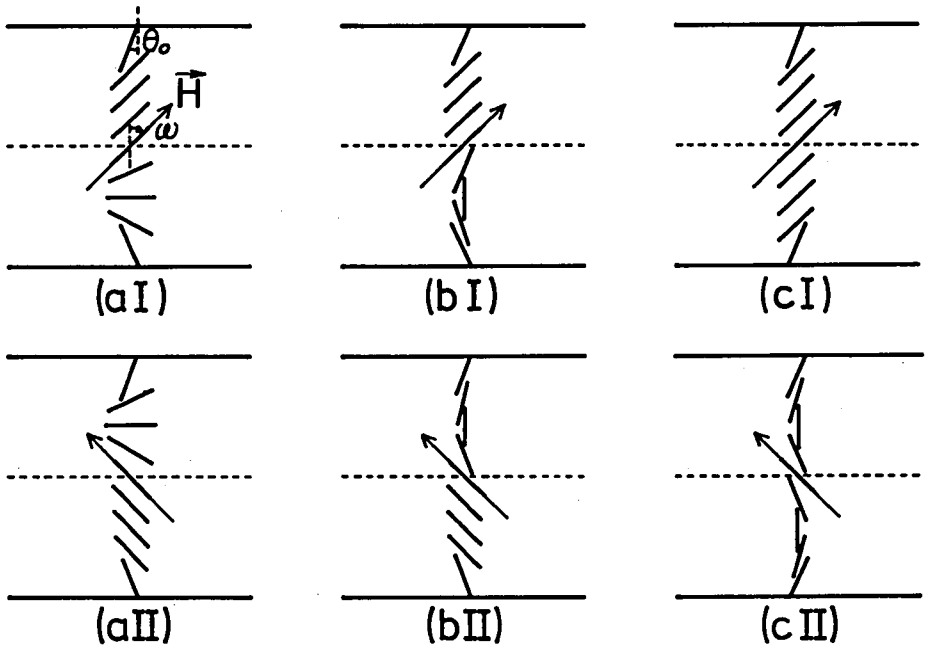

Fig. 3-4 Possible distortion patterns for nematic liquid-crystal molecular alignments in the presence of magnetic field $\vec{H}$. Symbols a, b, and c correspond to zero-field alignment cases (a), (b), and (c) in Fig. 3-1.

leads to the same capacitance change characteristics as for cases where the magnetic field is in $+\theta_{02}$ and $-\theta_{02}$ directions, and does not allow any critical Freedericksz transition for the magnetic field in the x-z plane. Polarizing microscopic and conoscopic observations are also used to confirm the determination[11].

3-2-2. Total-reflection method

When a light ray falls from optically dense glass material into optically sparse nematic liquid-crystal layer, its path changes according to director distributions, as shown in Fig. 3-5. Nematic liquid crystals are considered to be optically active unipolar materials, and their main refractive constants are put to be n_ω for or-

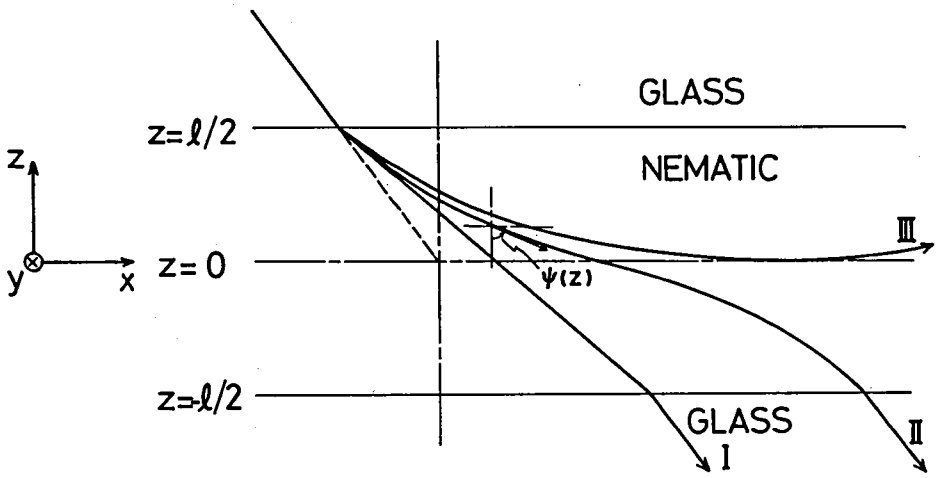

Fig. 3-5 Extraordinary light-ray paths in a liquid-crystal layer. I: unperturbed state, II: perturbed state (transmission), and III: perturbed state (total reflection).

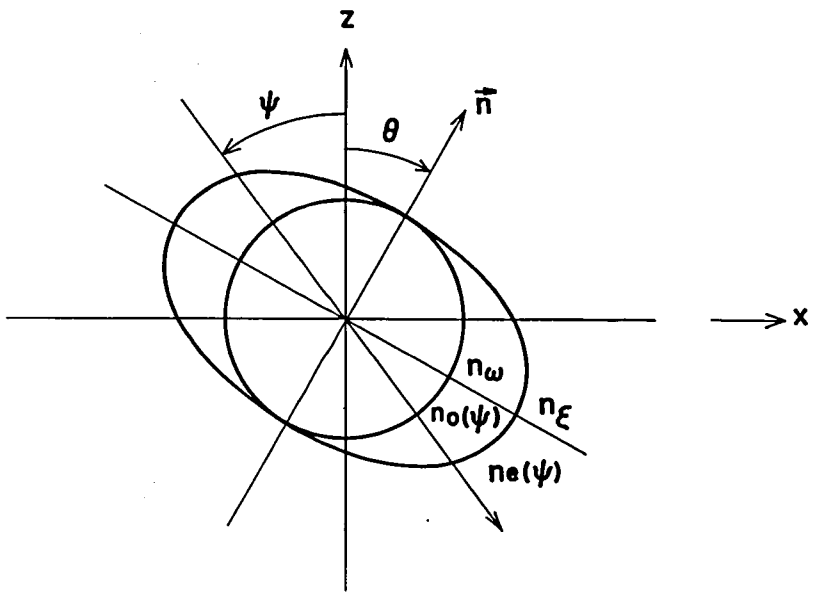

Fig. 3-6 Director index-ellipsoid.

dinary ray and n_ε for extraordinary ray ($n_\omega < n_\varepsilon$). When the director makes an angle $\theta(z)$ with respect to the z-axis as is shown in Fig. 3-6, the refractive constants for the light ray, passing in the direction

of angle $\psi(z)$ with respect to the z-axis, are represented as follows:

$$n_o(z,\psi) = n_\omega$$
$$n_e(z,\psi) = n_\varepsilon n_\omega / [\, n_\omega^2 \sin^2(\theta+\psi) + n_\varepsilon^2 \cos^2(\theta+\psi)\,]^{1/2} , \tag{3-10}$$

where the subscripts o and e represent the values for ordinary and extraordinary rays, respectively. Here, both the director and the incident light ray are assumed to be in the x-z plane. As n_o is constant ($n_o = n_\omega$), independent of director distribution $\theta(z)$, the total reflection of ordinary ray always occurs at the interface ($z = \ell/2$) and the critical angle for the total reflection is always given by

$$\psi_{co} = \arcsin (n_\omega / n_g) , \tag{3-11}$$

where n_g is the refractive index of glass material ($n_g > n_\varepsilon > n_\omega$). On the other hand, the critical angle ψ_{ce} for the total reflection of extraordinary ray depends on director distribution $\theta(z)$, as is considered in the following.

We consider the case where there is no director distortion, that is, $\theta(z) = \Theta$ = constant . In this case, n_e is constant at everywhere in the liquid-crystal layer. Consequently, the total reflection of extraordinary ray also occurs at the interface between glass substrate and liquid-crystal layer ($z = \ell/2$). The insertion of $\theta(\ell/2) = \Theta$ and $\psi(\ell/2) = \pi/2$ into Eq. (3-11) yields

$$n_e(\ell/2 , \pi/2) = n_\omega n_\varepsilon / (n_\omega^2 \cos^2\Theta + n_\varepsilon^2 \sin^2\Theta)^{1/2} . \tag{3-12}$$

The critical angle for the total reflection ψ_{ce} , therefore, is given by

$$\psi_{ce} = \arcsin [\, n_\omega n_\varepsilon / n_g (n_\omega^2 \cos^2\Theta + n_\varepsilon^2 \sin^2\Theta)^{1/2}] . \tag{3-13}$$

If the liquid crystal n_ω and n_ε values are known, Θ can be derived from ψ_{ce} measurement by using Eq. (3-13) for when no director dis-

tortions exist. Further, the following explains that Θ can be obtained, even when n_ω and n_ε values are unknown.

Here, consider the case when some director distortions exist ($d\theta/dz < 0$, *e.g.* see Fig. 3-4 (cI)) . The incident light wavelength, herein, is considered to be sufficiently small, as compared with the spatial distortion length in the director field. In this $d\theta/dz < 0$ case, $n_e(z,\psi)$ decreases going along the incident light ray, and the total reflection of extraordinary ray occurs at the median $z = 0$ (see Fig. 3-5). The insertion of $\theta(0) = \theta_M$ and $\psi(0) = \pi/2$ into Eq. (3-10) yields

$$n_e(0,\pi/2) = n_\omega n_\varepsilon / (n_\omega^2 \cos^2 \theta_M + n_\varepsilon^2 \sin^2 \theta_M)^{1/2} \quad , (3\text{-}14)$$

and then

$$\psi_{ce} = \arcsin [n_\omega n_\varepsilon / n_g (n_\omega^2 \cos^2 \theta_M + n_\varepsilon^2 \sin^2 \theta_M)^{1/2}] \ . \quad (3\text{-}15)$$

As $\theta_M = \Theta$ for when no director distortions exist, Eq. (3-13) degenerated into Eq. (3-15) . Consequently, for cases $d\theta/dz \leqq 0$, the critical angle for total reflention of extraordinary ray is always given by Eq. (3-15) .

Now, consider changes in ψ_{ce} caused by director realignment under a magnetic field. The magnetic field has an angle ω with respect to the z-axis and strength H which is sufficiently large.
(i) In cases of $\pi/2 \geqq \omega > \Theta$ (Fig. 3-4(cI)) , the condition $d\theta/dz < 0$ is satisfied and Eq. (3-15) holds. When field strength H is sufficiently large, θ_M is derived to equal ω in Section II ($\omega = 90°$ in Fig. 2-9). Consequently, from Eq. (3-15) , ψ_{ce} is obtained as

$$\psi_{ce} = \arcsin [n_\omega n_\varepsilon / n_g (n_\omega^2 \cos^2 \omega + n_\varepsilon^2 \sin^2 \omega)^{1/2}] \ , \quad (3\text{-}16)$$

and ψ_{ce} decreases as ω increases.
(ii) When $\omega = \Theta$, no distortions can occur in the director distribution, how much strong the field is. For this case, ψ_{ce} is constant,

in spite of the external magnetic field, and Eq. (3-13) holds. That is, in this $\omega = \Theta$ case, too, ψ_{ce} is represented by Eq. (3-16) .

(iii) When $0 \leqq \omega < \Theta$, a qualitative discussion can be yielded, as follows. If $\beta = 0$, the director is considered to align along the magnetic field $\vec{H}$, that is, $\theta(z) = \omega = \text{constant}$. In this case, total reflection always takes place at the interface between glass substrate and liquid-crystal layer ($z = \ell/2$). The critical angle ψ_{ce} is obtained by changing Θ of Eq. (3-13) to ω, that is Eq. (3-16) . When $\beta \neq 0$, on the contrary, some director distortions occur by applying magnetic field $\vec{H}$. In this $0 \leqq \omega < \Theta$ case, however, the director distribution is such as $d\theta/dz > 0$, and $n_e(z,\psi)$ increases going along the incident light ray. Consequently, the total reflection of extraordinary ray occurs at the interface ($z = \ell/2$). We obtain

$$\psi_{ce} = \arcsin \left[n_\omega n_\varepsilon / n_g \left(n_\omega^2 \cos^2 \theta_0 + n_\varepsilon^2 \sin^2 \theta_0 \right)^{1/2} \right] , \tag{3-17}$$

where $0 \leqq \omega < \theta_0 < \Theta$. At the infinite case, where $\beta = \infty$, as θ_0 coincides with Θ, ψ_{ce} is given by the same expression as Eq. (3-13) .

The above discussions on the ω - dependence of ψ_{ce} are summarized as follows:

$$\begin{cases} H=0 & \psi_{ce}=\arcsin[n_\omega n_\varepsilon/n_g (n_\omega^2\cos^2\Theta+n_\varepsilon^2\sin^2\Theta)^{1/2}] \quad (3\text{-}13) \\ H\neq 0 \ (H \gg H_c') & \begin{cases} \Theta \leqq \omega \leqq \pi/2 & \psi_{ce}=\arcsin[n_\omega n_\varepsilon/n_g (n_\omega^2\cos^2\omega+n_\varepsilon^2\sin^2\omega)^{1/2}] \quad (3\text{-}16) \\ 0 \leqq \omega < \Theta & \begin{cases} \beta = 0; & \psi_{ce}=\arcsin[n_\omega n_\varepsilon/n_g (n_\omega^2\cos^2\omega+n_\varepsilon^2\sin^2\omega)^{1/2}] \quad (3\text{-}16) \\ \beta \neq 0; & \psi_{ce}=\arcsin[n_\omega n_\varepsilon/n_g (n_\omega^2\cos^2\theta_0+n_\varepsilon^2\sin^2\theta_0)^{1/2}] \quad (3\text{-}17) \\ \beta = \infty; & \psi_{ce}=\arcsin[n_\omega n_\varepsilon/n_g (n_\omega^2\cos^2\Theta+n_\varepsilon^2\sin^2\Theta)^{1/2}] \quad (3\text{-}13) \end{cases} \end{cases} \end{cases}$$

By considering the relations $0 \leqq \omega < \theta_0 < \Theta \leqq \pi/2$ and $n_\varepsilon > n_\omega$ and comparing Eqs. (3-16), (3-17), and (3-13) , ψ_{ce} in the $0 \leqq \omega < \Theta$ case is found to decrease as β increases. Consequently, the relation between ψ_{ce} and ω , under a sufficiently strong magnetic field, is obtained as shown in Fig. 3-7 . In Fig. 3-7(b) , the ψ_{ce} vs ω curves represented by Eq. (3-17) exist in a shadowed region.

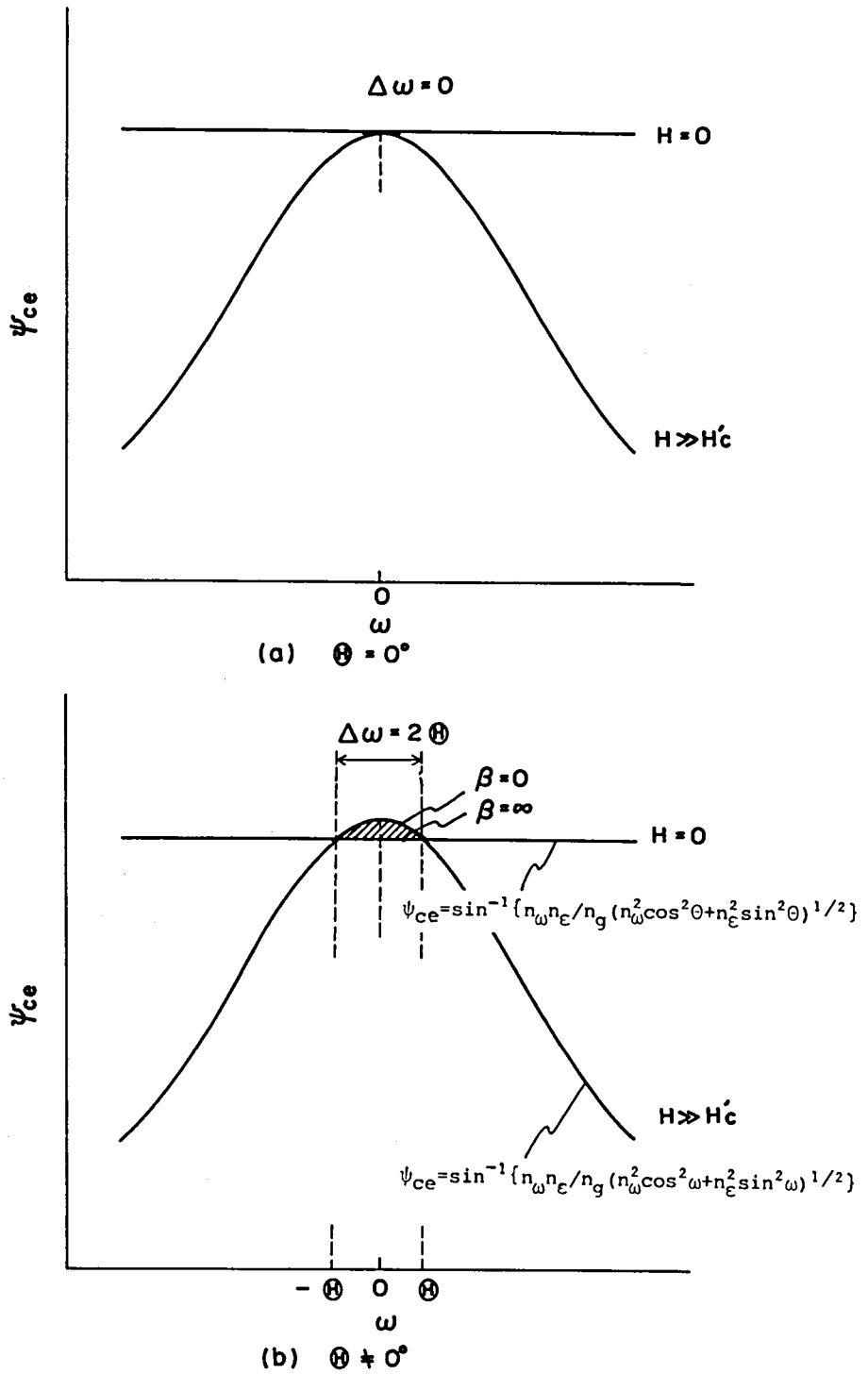

Fig. 3-7 Relations between critical angle ψ_{ce} for total reflection and applied magnetic-field direction.

Easy-axis angle Θ is obtained by a set of ψ_{ce} measurements. As is shown in Fig. 3-7 , the ψ_{ce} vs ω curve intersects with the line $\psi_{ce} = \arcsin [n_\omega n_\varepsilon / n_g (n_\omega^2 \cos^2\Theta + n_\varepsilon^2 \sin^2\Theta)^{1/2}]$ at two points $\omega = \omega_1 \ (=\Theta)$ and $\omega = \omega_2 \ (=-\Theta)$. Consequently, by measuring ψ_{ce} under no magnetic field and the ω-dependence of ψ_{ce} under sufficiently strong magnetic field, the Θ value can be derived by using the relation

$$\Theta = (1/2)\,\Delta\omega\,, \tag{3-18}$$

where $\Delta\omega = \omega_1 - \omega_2$. Note that, if the glass n_g value is known, it is possible to obtain liquid-crystal refractive indices, n_ω and n_ε , besides Θ by measuring ψ_{co} and ψ_{ce} under a magnetic field and using the relations, Eq. (3-11), (3-13), and (3-18) .

3-3. Principle of The Freedericksz-Transition Measurements

3-3-1. Magneto-capacitance method

Director distribution changes under a magnetic field, considered in Section II , can be observed as electric capacitance changes based on the director dielectric anisotropy. As this magneto-capacitance method is well known and is being widely used, the explanation in this section is concentrated upon anchoring parameters dependence of the electric-capacitance vs magnetic field strength characteristics.

Now, consider a nematic liquid-crystal layer between z and $z + dz$ where the director makes an angle θ with the z-axis. Electric capacitance dC per unit area of the liquid-crystal layer between z and $z + dz$ is given by

$$dC = (\varepsilon_{\parallel} - \Delta\varepsilon \sin^2\theta)\, dz \ . \tag{3-19}$$

When no external magnetic field exists, the relation $\theta(z) = \Theta = \text{constant}$ holds. The electric capacitance per unit area of liquid-crystal layer with thickness ℓ is represented as

$$C_0 = (\varepsilon_{//} - \Delta\varepsilon \sin^2 \Theta) / \ell \ . \qquad (3\text{-}20)$$

On the other hand, electric capacitance C for a liquid-crystal layer distorted under a magnetic field is obtained by

$$\begin{aligned} 1/C &= \lim_{z \to 0} \Sigma (dC)^{-1} \\ &= \int_{-\ell/2}^{\ell/2} (\varepsilon_{//} - \Delta\varepsilon \sin^2 \theta)^{-1} \, dz \\ &= 2\xi_0 \int_{\theta_0}^{\theta_M} (\varepsilon_{//} - \Delta\varepsilon \sin^2\theta)^{-1} [(1+K \sin^2\theta)/(1/k^2 - \sin^2\theta)]^{1/2} d\theta \\ &= \ell \int_{\theta_0}^{\theta_M} (\varepsilon_{//} - \Delta\varepsilon \sin^2\theta)^{-1} [(1+K\sin^2\theta)/(1/k^2 - \sin^2\theta)]^{1/2} d\theta \\ &\quad / \int_{\theta_0}^{\theta_M} [(1+K\sin^2\theta)/(1/k^2 - \sin^2\theta)]^{1/2} d\theta \ . \end{aligned} \qquad (3\text{-}21)$$

The electric capacitance increase ΔC by the applied magnetic field is obtained by comparing Eqs. (3-20) and (3-21) as

$$\begin{aligned} \Delta C/C_0 = \ & (\varepsilon_{//} - \Delta\varepsilon \sin^2\theta)^{-1} \int_{\theta_0}^{\theta_M} f(\theta,k) \, d\theta \\ & / \int_{\theta_0}^{\theta_M} (\varepsilon_{//} - \Delta\varepsilon \sin^2 \theta)^{-1} f(\theta,k) \, d\theta \ - \ 1 \ , \end{aligned} \qquad (3\text{-}22)$$

where

$$f(\theta,k) = [(1 + K \sin^2 \theta) / (1/ k^2 - \sin^2 \theta)]^{1/2} \ . \qquad (3\text{-}23)$$

The equilibrium θ_0 and θ_M values and $\theta(z)$, under the applied magnetic field, which should be inserted into Eq. (3-22) , are obtained as presented in Section II as functions of anchoring parameters, Θ and B_θ .

As an example of anchoring-parameters dependence of the $\Delta C/C_0$ vs normalized magnetic field strength h curves, we consider the $\Theta = 0°$ case. The h - dependence of θ_0 and θ_M obtained in Section 2-4 (see Fig. 2-10) and Eq. (3-22) . The results are shown in Fig. 3-8(a) . The constant values used for the calculations were selected, as an example, from reported values, such as for MBBA

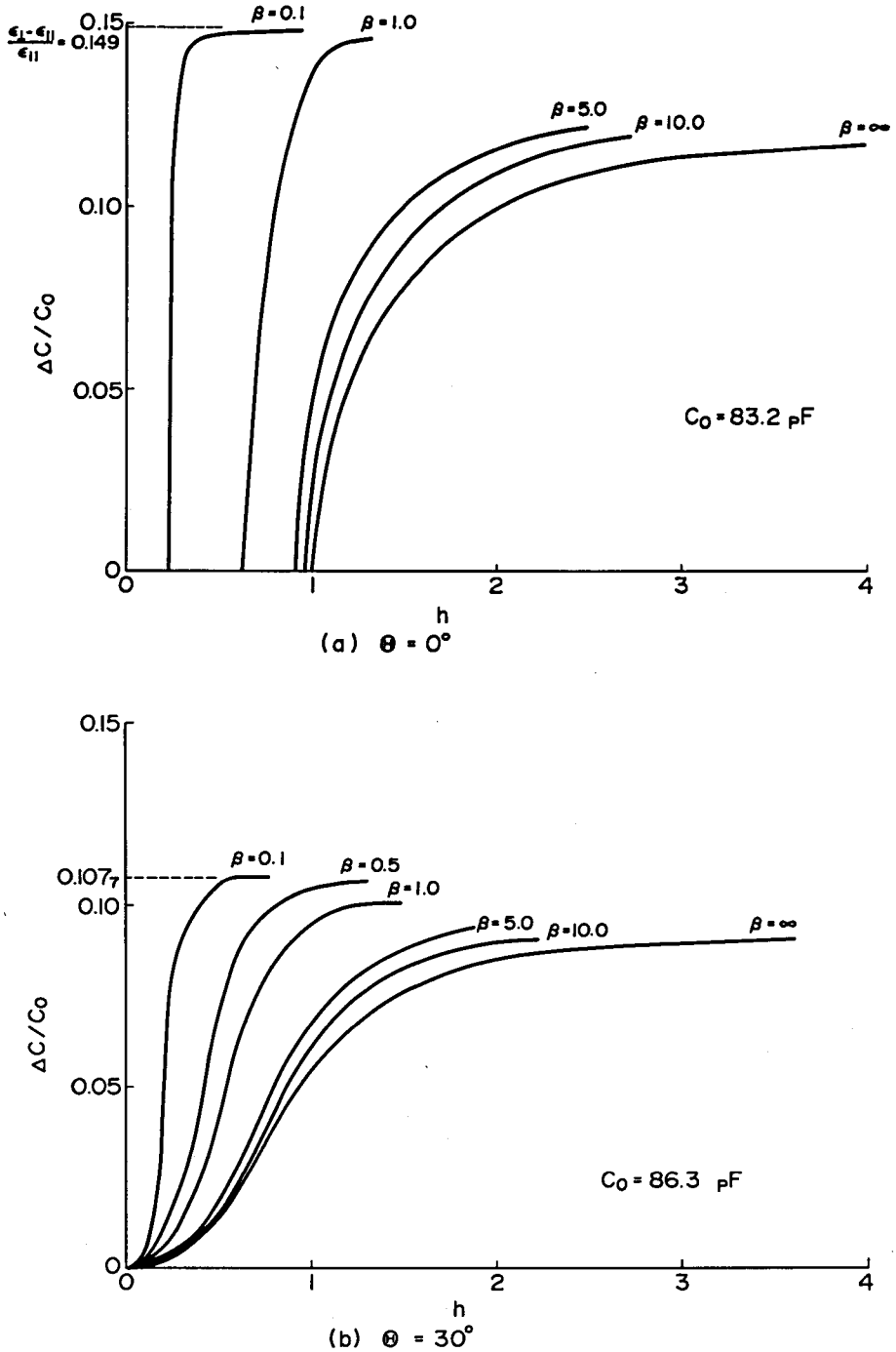

Fig. 3-8 Magnetic field strength h dependence of $\Delta C/C_0$ for various β values.

$\varepsilon_{//} = 4.7$

$\varepsilon_{\perp} = 5.4$

$\chi_a = 9.7 \times 10^{-8}$

$K_{11} = 6.0 \times 10^{-7}$ dyn

$K_{33} = 7.5 \times 10^{-7}$ dyn

and $\ell = 50\,\mu m$. The angle θ_M increases with h, and $\Delta C/C_0$ increases up to some saturated values, because $\Delta\varepsilon < 0$ ($\varepsilon_{//} < \varepsilon_{\perp}$) for MBBA. The saturated $\Delta C/C_0$ values increase as β decreases, because of diminishing transition layers near each substrate, where directors are strongly affected by the interfacial anchoring force and do not align along the magnetic field. This h - dependence of $\Delta C/C_0$ corresponds to the h - dependence of θ_M and θ_0 shown in Fig. 2-10, and critical magnetic field strengths for the electric capacitance change coincide with h_c for director distortions.

Another example of the h - dependence of $\Delta C/C_0$ calculations is for $\Theta = 30°$, which is shown in Fig. 3-8(b). In this $\Theta \neq 0°$ case, any critical phenomenon is not observed in the h - dependence of $\Delta C/C_0$ as well as in the h - dependence of θ_M and θ_0 (see Fig. 2-10). The β dependence of saturated $\Delta C/C_0$ values is in the same tendency as those in the above-mentioned $\Theta = 0°$ case, and also corresponds to β dependence of (θ_0 , θ_M) vs h curves in Fig. 2-10. Moreover, tangent of $\Delta C/C_0$ vs h curves coincides with that of θ_M vs h curve by superimposing the line $\Delta C/C_0 = 0$ on the line $\Theta = 30°$. This guarantees that the intercept point for a tangent of $\Delta C/C_0$ vs h curve and the $\Delta C/C_0 = 0$ line gives h_c, which is defined in Section 2-4 for $\Theta \neq 0°$ cases. Thus, by measuring the h - dependence of $\Delta C/C_0$, we can obtain critical magnetic field strength h_c for the Freedericksz transition.

3-3-2. Total-reflection method

As the expression (3-15) holds for any director distortion in $d\theta/dz < 0$ form, we can derive the h - dependence of ψ_{ce} corresponding

to the Freedericksz transition, by combining Eq. (3-15) and the h - dependence of θ_M obtained in Section 2-4 (see Fig. 2-10) . Calculations were performed using the constant values for MBBA, $n_\omega = 1.54$ and $n_\varepsilon = 1.75$, and putting $n_g = 1.878$. The ψ_{ce} vs h curves calculated for various β values in $\Theta = 0°$ and $10°$ cases are shown in Fig. 3-9.

In $\Theta = 0°$ case, critical changes in ψ_{ce} are expected and the critical magnetic field strength equals h_c discussed in Section 2-4. When $\Theta = 10°$, on the other hand, ψ_{ce} gradually changes according to the h - dependence of θ_M shown in Fig. 2-10 . Note that, in these total-reflection measurements, saturated ψ_{ce} values under a strong magnetic field are the same for any β value. This is because ψ_{ce} is determined by θ_M , which coincides with the magnetic field angle independent of β values, when the magnetic field is sufficiently strong. Consequently, as mentioned in Section 3-2-2, we can derive n_ω , n_ε , and Θ values by measuring ψ_{co} and ψ_{ce} , when no magnetic field is applied and ψ_{ce} under sufficiently strong magnetic field and using Eqs. (3-11) , (3-13) , and (3-18). This enables curve fitting for measured ψ_{ce} vs h curves, which allows more precise β derivation than the method using h_c vs $1/\beta$ curves (Fig. 2-12) and h_c values obtained from the intercept of a ψ_{ce} vs h curve tangent and a line $\psi_{ce} = \arcsin[n_\omega n_\varepsilon / n_g (n_\omega^2 \cos^2 \Theta + n_\varepsilon^2 \sin^2 \Theta)^{1/2}]$.

3-4. Summary

Improved magneto-capacitance method and newly developed total-reflection method, presented in this section, have been compared with conventional methods for both interfacial alignment angle θ_0 measurements and the Freedericksz-transition observation in Table 3-1. Details are as follow.

1) Easy-axis angle Θ has been derived from director interfacial

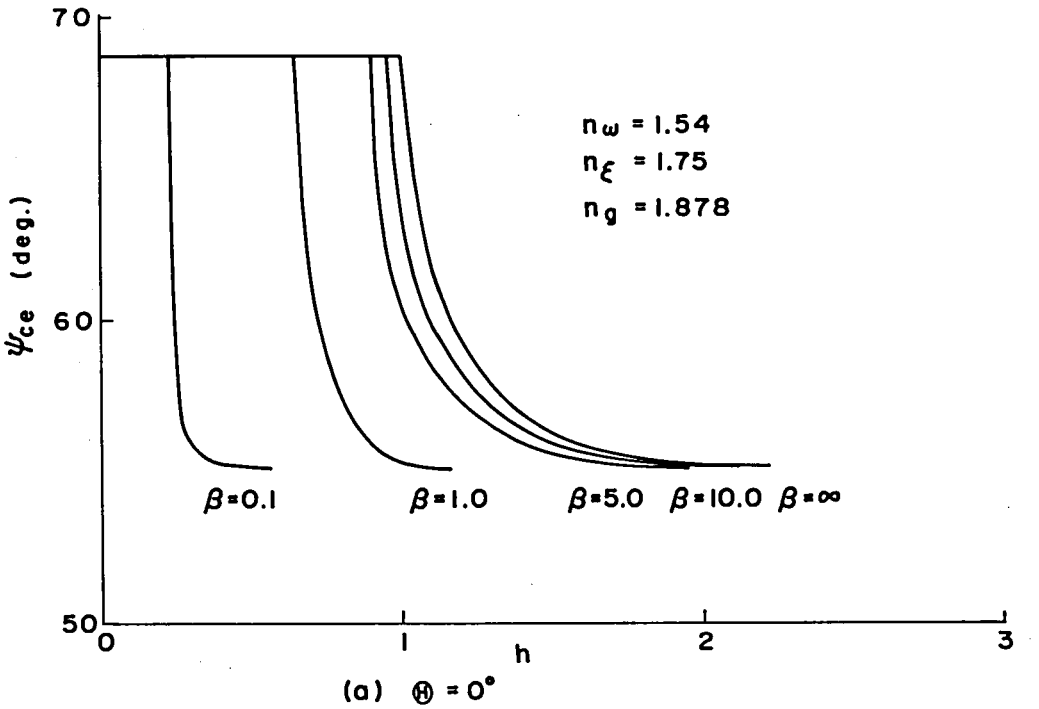

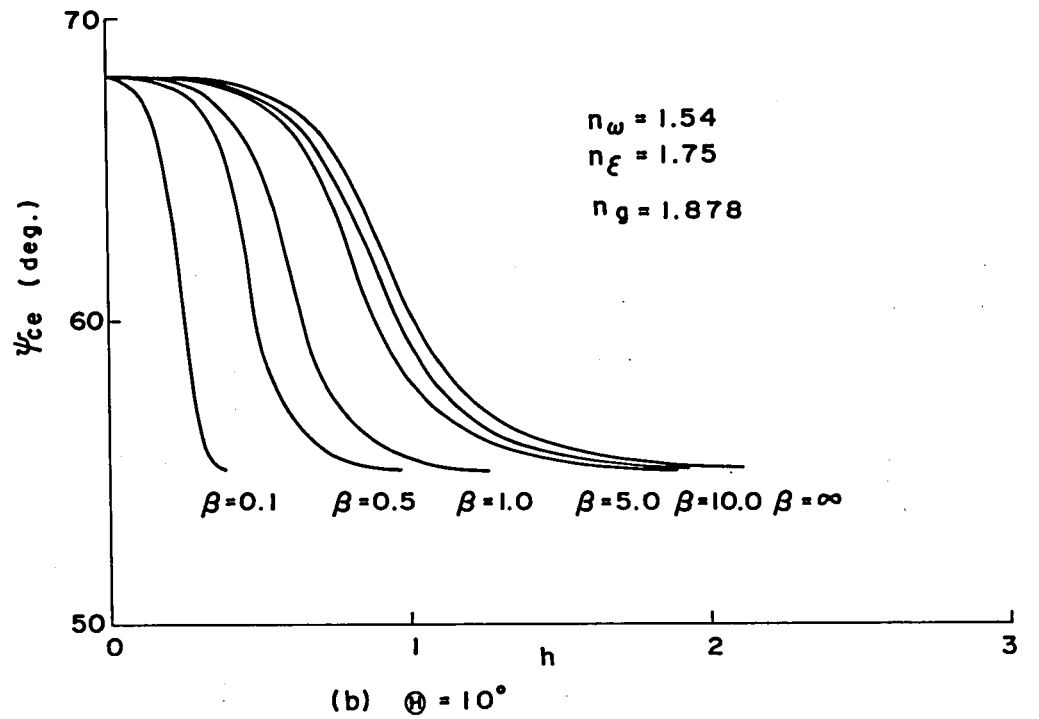

Fig. 3-9 Magnetic field strength h dependence of ψ_{ce} for various β values.

Table 3-1 Comparison of developed and conventional methods for both interfacial alignment angle measurements and the Freedericksz-transition observation.

		INTERFACIAL ALIGNMENT-ANGLE θ_0 MEASUREMENTS		FREEDERICKSZ-TRANSITION OBSERVATION	INSULATING SUBSTRATE CASES
		UNIFORM ALIGNMENT $\Theta = \theta_0$	DISTORTED ALIGNMENT $\Theta \leq \theta_0$ $(d\theta/dz < 0)$ $\Theta \geq \theta_0$ $(d\theta/dz > 0)$		
CONVENTIONAL	OPTICAL METHOD	○	×	×	○
CONVENTIONAL	CAPACITANCE METHOD	○	×	○*	×
THIS WORK	IMPROVED CAPACITANCE METHOD	○	○		
THIS WORK	NEWLY DEVELOPED TOTAL-REFLECTION METHOD	○	×	○	○

ANCHORING-STRENGTH DERIVATION

○ POSSIBLE
× IMPOSSIBLE

* Anchoring-strength dependence of the electric capacitance changes, according to the Freedericksz transition, is calculated in this work.

alignment angle θ_0 measurements, when no director distortions exist ($d\theta/dz = 0$) .

2) In cases of existing some director distortions, Θ has been regarded as $\Theta \leqq \theta_0$ ($d\theta/dz < 0$ case) or $\Theta \geqq \theta_0$ ($d\theta/dz > 0$ case) .

3) A magneto-capacitance method has been introduced, which is applicable for the director distribution ($d\theta/dz < 0$, $d\theta/dz = 0$, $d\theta/dz > 0$) determination and θ_0 measurements.

4) A total-reflection method for θ_0 measurements has been developed, which is applicable even for insulating-substrate samples.

5) The total-reflection method, as well as the magneto-capacitance method, has also been used to measure the critical field strength H_c' for the Freedericksz transition.

6) The anchoring-strength coefficient B_θ can be derived for various liquid-crystal substrate interfaces, including insulating substrate cases, by using the magneto-capacitance or the total-reflection method and measuring Θ and H_c'.

References

[1] E. Guyon, P. Pieranski, and M. Boix, Lett. Appl. Eng. Sci., 1, 19 (1973)

[2] W. Urbach, M. Boix, and E. Guyon, Appl. Phys. Lett., 25, 479 (1974)

[3] E. P. Raynes, Rev. Phys. Appl., 10, 117 (1975)

[4] D. Meyerhofer, Phys. Lett., A51, 407 (1975)

[5] W. A. Crossland, J. H. Morrissy, and B. Needham, J. Phys., D9, 2001 (1976)

[6] G. Baur, V. Wittwer, and D. W. Berreman, Phys. Lett., A56, 142 (1976)

[7] K. Toriyama and T. Ishibashi, in *Nonemissive Electrooptic Displays*, edited by A. R. Kmetz and F. K. von Willisen (Plenum, New York, 1976)

[8] T. J. Scheffer and J. Nehring, J. Appl. Phys., 48, 1783 (1977)

[9] H. Onnagawa and K. Miyashita, Jpn. J. Appl. Phys., 13, 1741 (1974)

[10] H. Onnagawa, M. Kuwahara, and K. Miyashita, J. Phys. (Paris), C3-40, C3-519 (1979)

[11] G. Porte, J. Phys. (Paris), 37, 1245 (1976)

IV. EXPERIMENTAL DERIVATION OF ANCHORING PARAMETERS

4-1. Introduction

In order to obtain some relationships between surfactant structure or substrate material and anchoring parameters, Θ and B_θ, anchoring-parameter measurements were performed for various surface-treated substrates. The magneto-capacitance and the total-reflection methods were used for Θ and h_c measurements, and the calculated B_θ vs h_c relationships were used for B_θ derivations. In Section 4-2, experimental equipment and procedures for magneto-capacitance and total-reflection measurements are presented. Section 4-3 provides liquid-crystal cell constructions and substrate surface treatment procedures. Anchoring parameters were derived for the interfaces between a nematic liquid crystal, MBBA, and In_2O_3 - evaporated or bare glass substrates with various organic surfactant layers. The experimental results are presented in Section 4-4. In Section 4-5, effects of both surfactant and substrate materials on anchoring parameters are discussed. A summary is presented in Section 4-6.

4-2. Measuring Equipment

4-2-1. Magneto-capacitance measurements

Capacitance magnetic-field strength and direction dependence measurements were performed by setting a liquid-crystal cell in an electric magnet and rotating the cell in the magnetic field. The magnetic field strength was detected by a Hall element attached to a magnetic pole.

A Yokogawa-Hewlett-Packard 4270A Automatic Capacitance Bridge

was used to measure the liquid-crystal cell capacitance. In order to suppress a fringing electric field around the measuring electrode, an annular guard electrode surrounds the circular measuring electrode on one of the cell substrates. The gap between the measuring and the guard electrodes (20 μm) is less than a typical measuring electrode separation (∿50 μm) from a counter electrode on the other substrate. The measuring and guard electrodes are connected to capacitance bridge LO and ground terminals, respectively, because the LO terminal potential is nearly the same as ground potential, when the bridge is balanced. The counter electrode is connected to the capacitance bridge HI terminal.

4-2-2. Total-reflection measurements

(i) Experimental equipment

Experimental equipment for total-reflection measurements is shown in Fig. 4-1 . Linearly polarized 6328Å light beam is produced by He-Ne laser tube (GLG2031, Nippon Electric Co., Ltd.) and its polarization plane is rotated by rotating a half wave plate. When the polarization plane is parallel (perpendicular) to the page, the incident light ray is an ordinary (extraordinary) one for the nematic liquid-crystal layer in the sample cell. In order to improve the light beam linearity, a polarizer is put in front of the half wave plate, and rotated by 90° corresponding to the half wave plate 45° rotation. The light beam is introduced through two prisms into a magnetic field and falls on the sample liquid-crystal cell through a 1 mmϕ aperture. The transmitted light beam goes through an analyzer and its one component, whose polarization plane coincides with that of the incident light beam, is detected by a solar cell.

The sample cell is constructed by two glass substrates in a cylindrical structure, which allows the incident light beam to always fall perpendicularly on the cell surface. The cell construction is

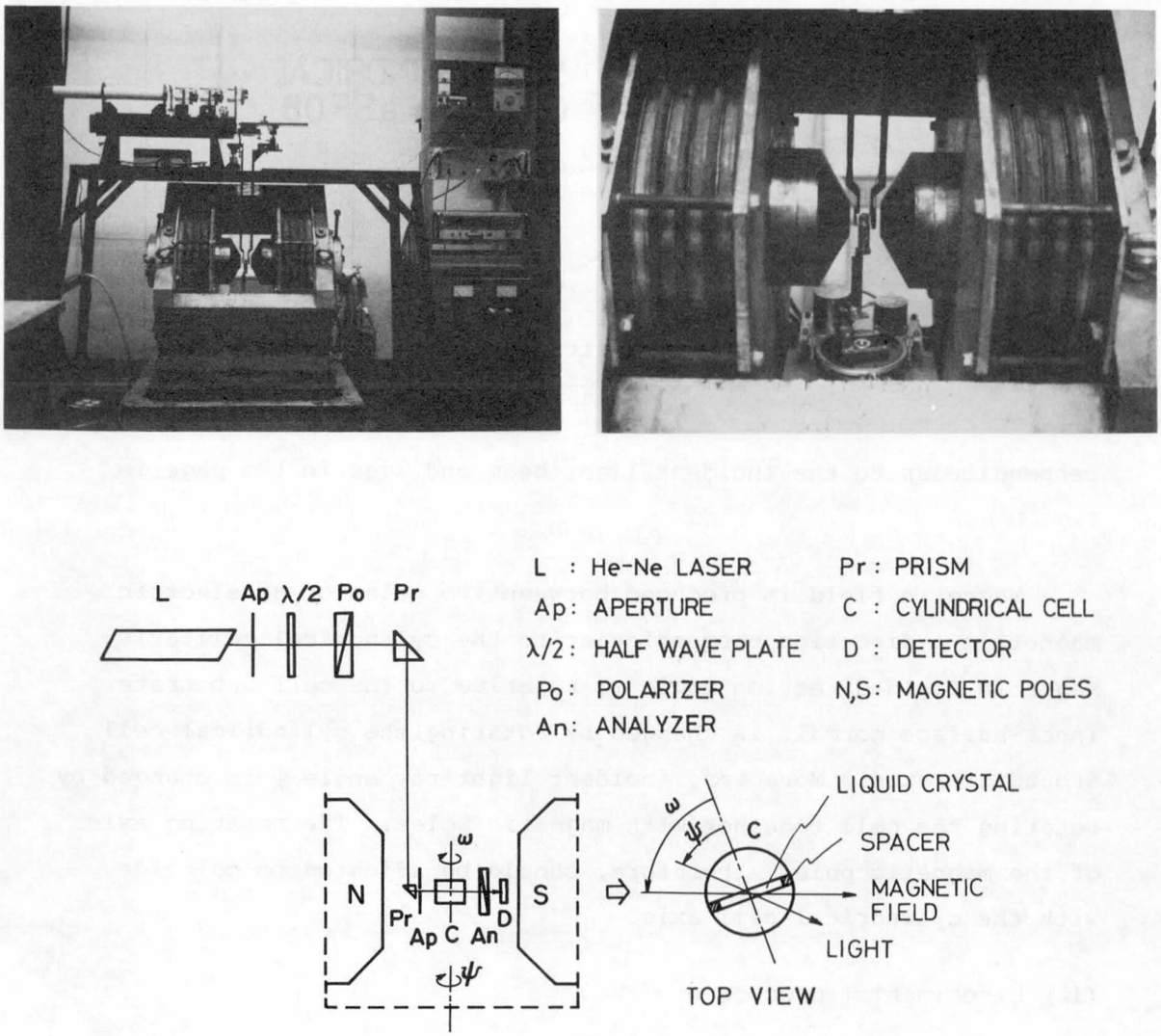

Fig. 4-1 Experimental equipment for total-reflection measurements.

shown in Fig. 4-2 . The glass material is Lanthan-Schwer-Flint glass, LaSF-08, which is a lead glass with lanthanum as its main ingredient. The LaSF-08 refractive index is 1.8782 for 6328Å wavelength, which is large enough for producing a total reflection at an interface with an MBBA layer with refractive index $n_\varepsilon \simeq 1.75$. The two glass substrates are separated by teflon film spacers, and contain a liquid-crystal layer between them. This cylindrical cell is set so that its axis is

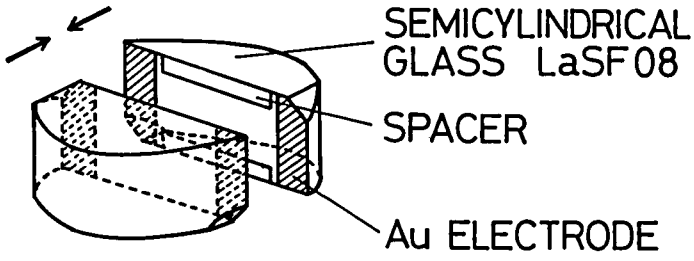

Fig. 4-2 Sample-cell structure for total-reflection measurements.

perpendicular to the incident light beam and lies in the page in Fig. 4-1 .

Magnetic field is produced between two poles of an electric magnet in a direction perpendicular to the cylindrical cell axis. Magnetic field direction angle ω, relative to the cell substrate inner-surface normal, is changed by rotating the cylindrical cell around its axis. Moreover, incident light-ray angle ψ is changed by rotating the cell together with magnetic poles. The rotating axis of the magnetic poles, therefore, should be adjusted to coincide with the cylindrical cell axis.

(ii) Experimental procedures

The cylindrical cell is constructed by pressing together two semicylindrical pieces with teflon film spacers. The cell gap is obtained by measuring the electric capacitance between two Au electrodes evaporated partly on substrate inner faces (see Fig. 4-2) .

Some revisions are necessary in determining total-reflection critical angles ψ_{ce} . The reason is that some discrepancies exist between ψ_{ce} and cell rotation angle ψ where transmissive light diminishes. When an incident light beam has a $2a$ diameter, as is shown in Fig. 4-3 , the incident angle differs spatially and the

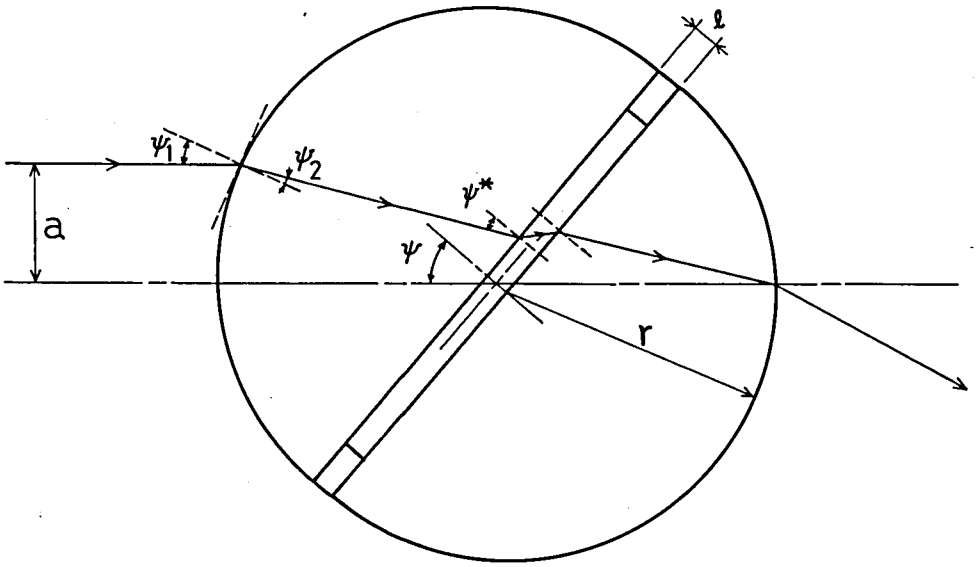

Fig. 4-3 Light-ray path in cylindrical cell.

transmitted light expands in a direction perpendicular to both the cylindrical-cell axis and the incident light beam. When the transmitted light diminishes, a condition ψ^* (an incident angle at the light beam edge) = ψ_{ce} holds and cell rotation angle ψ is less than ψ^* . The difference ($\psi^*-\psi$) is calculated to be 1°44' ± 2' , by using relations

$$\psi^* = \psi - \psi_1 + \psi_2$$

$$\psi_1 = \arcsin\{[a - (\ell/2)\sin\psi]/r\}$$

$$\psi_2 = \arcsin\{[a - (\ell/2)\sin\psi]/n_g r\}$$

and values

a = 0.5 mm

ℓ = 0.05 mm

r = 7.5 mm

n_g = 1.8782

Revision values were also obtained experimentally by filling

the cell with several test liquids, such as water, ethanol, and glycerol. The differences between measured and calculated ψ_{ce} values are 3°05'∿3°25', which are almost twice larger than the above-estimated value (Table 4-1). Sequently, it is necessary to determine the revision value from total-reflection critical-angle measurements for a vacant cell, before practising measurements for liquid-crystal containing cells.

Table 4-1 Total-reflection critical angles for test materials.

MATERIALS	REFRACTIVE INDICES*	ψ_c(Calc.)	ψ_c(Meas.)	REVISION VALUES
AIR	1.000	32°10'	35°25'	3°15'
WATER	1.332	45°10'	48°15'	3°05'
ETHANOL	1.361	46°26'	49°40'	3°14'
GLYCEROL	1.471	51°35'	55°00'	3°25'

* *Smithsonian Physical Tables*, 9th revised ed. (Smithsonian Institution, 1964)

After the revision-value derivation, the cell is filled with liquid-crystal materials by capilarity, and submitted for easy-axis angle measurements and Freedericksz-transition observations. The angle Θ measurements are performed by changing ω discretely by 1°∿2° and observing ψ_{ce} (see Fig. 3-7). Applied magnetic field strength H is typically 6 kOe which is sufficiently larger than typical H_c' values, 1.5∿2.0 kOe, for $\ell \simeq 50$ μm. The angle ψ_{ce} measurements are performed alternatively for $H = 0$ and $H \gg H_c'$ at each ω. For Freedericksz-transition observations, the cell is fixed in $\omega = 90°$ position, which is critically determined from the foregoing Θ measurements.

4-3. Cell preparation

The surfactants used in the present study are cationic (ammonium salts), nonionic (amines and an alcohol), and amphoteric (Lecithin and Cepharin) surfactants with relatively long hydrocarbon chains (Tokyo Chemical Industry Co., Ltd.). In cationic surfactants, a perfluorocarbon material, FS150 (Dainippon Ink and Chemicals Inc.) [1], is included. All of these surfactants adsorb physically on substrates, not by chemical bondings. Cationic silane coupling agents, nS (n = 10,12,14,16,18, Toray Silicone Co., Ltd.)[2] and 18AS (Tokyo Chemical Industry Co., Ltd.), which have chemisorption ability, were also examined.

Although substrate surface-treatment procedures are slightly different in detail for each surfactant family, the surfactant layer is commonly deposited by dipping a substrate in a surfactant solution. The solvents used are water for FS150 and silanes nS, ethanol for ammonium salts, amines, and an alcohol, and *n*-hexane for Lecithin, Cepharin, and 18AS. The surfactant concentration is chosen so that the adsorbed molecular density is enough to produce liquid-crystal alignments, independent of surfactant concentration[3] (for surfactant-concentration effects, see Section 5-4-1). After bare or In_2O_3-evaporated glass substrates are dipped in the surfactant solution, typically for five minutes, they are smoothly withdrawn and dried on a clean bench. In general, the substrates are finally cured at $\sim$100°C. Especially, in silane coupling agent nS cases, the substrates, withdrawn from surfactant solutions, are dipped and rinsed in water. After rinsing, the residual water on substrates was blown away by dry nitrogen gas.

Liquid-crystal material used is MBBA (Fuji Pigment Co., Ltd.) in the nematic phase. The nematic $\rightarrow$ isotropic transition temperature of MBBA used was 44.0°C, and measurements were performed at room

temperature (23∿25 °C) .

4-4. Experimental Results

Elastic constants of MBBA were derived from H_c' measurements, before anchoring-parameters derivation is carried out. Measurements were accomplished for MBBA on In_2O_3 - evaporated glasses coated with FS150, 18S, Lecithin, and *n*-hexadecylamine, by using the magneto-capacitance method. For whole samples with various thickness ℓ values, Θ values were derived to be zero. Moreover, critical magnetic field strength H_c' values were measured and plotted versus reciprocal thickness in Fig. 4-4 . As is shown in Fig. 4-4 , decreasing nematic layer thickness ℓ makes H_c' less than the value given by $(\pi/\ell)(K_{33}/\chi_a)^{1/2}$. This is because β decreases in proportion to ℓ. So, precise K_{33} determination from the formula $H_c' = (\pi/\ell)(K_{33}/\chi_a)^{1/2}$ should be made in a region of small $1/\ell$ values. In this region, the tangent angle of H_c' vs $1/\ell$ curves is nearly constant for every surfactant, which gives the value $K_{33} = (9.5 \pm 0.7)\times10^{-7}$ dyn. This elastic constant value is rather larger than previously reported values[4]. One of the reasons for the smaller measured elastic constants in previous papers may be the assumption of strong anchoring in the analysis. The details of previously reported methods for elastic constant measurements and derived K_{33} values are presented in Appendix A. By using homogeneously surface-treated substrates, K_{11} was determined to be $(8.4 \pm 0.6)\times10^{-7}$ dyn. For the magnetic anisotropy, the value $\chi_a = 1.16\times10^{-7}$ [5] was adopted for further discussions as a reliable value.

4-4-1. Surfactant-structure effects on anchoring parameters

In order to investigate surfactant structure effects on anchoring parameters, surfactants were chosen from the viewpoints of alkyl chain length, chain properties (hydrocarbon or fluorocarbon),

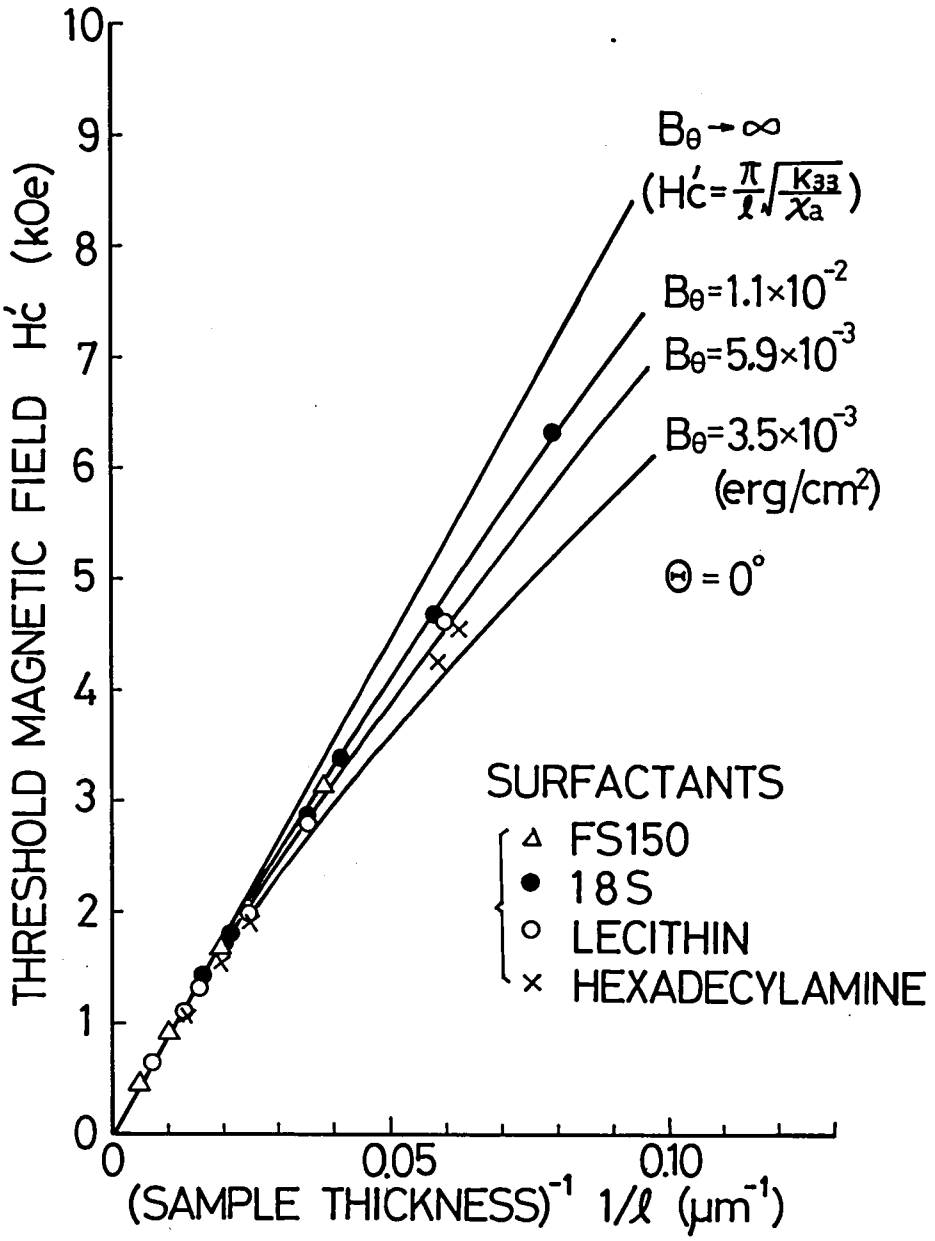

Fig. 4-4 Threshold magnetic field versus sample thickness for MBBA on In_2O_3 - evaporated glasses coated with various surfactants. The points represent experimental results: the solid lines are calculated with $K_{33} = 9.5\times10^{-7}$ dyn and $\chi_a = 1.16\times10^{-7}$ parameter values.

adsorption-group properties (chemisorption or physisorption), and ionic properties (cationic, nonionic or amphoteric).

Surfactants examined were homologous series of *n*,*n*-dimethyl-*n*-alkyl-3-aminopropyltrimethoxysilyl chloride, *n*-alkyltrimethylammonium salts, and *n*-alkylamines as well as some other cationic, nonionic, and amphoteric surfactants. Their chemical formulas are shown in Table 4-2. Substrates used were In_2O_3 - evaporated glasses. The easy-axis angle Θ and the critical field strength H_c' were measured by the magneto-capacitance method and used to derive B_θ values by using the calculated relationships between B_θ and H_c', such as shown in Fig. 2-12.

Table 4-2 Derived easy-axis angles Θ and anchoring-strength coefficients B_θ on interfaces between MBBA and In_2O_3 - evaporated glass substrates with various surfactants (x; concentration, S; withdrawing speed, T; temperature).

(a) SILANE COUPLING AGENTS

C_nH_{2n+1}
$N^+CH_2CH_2CH_2Si(OCH_3)_3 \cdot C\ell^-$
CH_3 CH_3

x=1.0×10^{-3} mol/l in WATER
S=∿300 mm/s
T=21.5∿23.5 °C

CODES	n	Θ(deg)	B_θ (×10^{-3}erg/cm^2)
18S	18	0	12 ± 6
16S	16	0	36 ± 7
14S	14	0	32 ± 8
12S	12	0	21 ± 9
10S	10	0	16 ± 2

$C_nH_{2n+1}Si(OC_2H_5)_3$

x=1.0×10^{-3} mol/l in n-HEXANE
S=∿300 mm/s
T=22.0 °C

CODES	n	Θ(deg)	B_θ (×10^{-3}erg/cm^2)
18AS	18	0	2.2 ± 0.8

(b) CATIONIC SURFACTANTS

$C_nH_{2n+1}N^+(CH_3)_3 \cdot C\ell^-$

$x=3.0\times10^{-3}$ mol/l in ETHANOL
S=∿ 1 mm/s (∿ 300 mm/s for 16Cl)
T=21.5∿ 25.0 °C

CODES	n	Θ(deg)	B_θ ($\times10^{-3}$erg/cm^2)
18Cl	18	0	2.7 ± 0.3
16Cl	16	0	∿7.6
12Cl	12	0	2.7 ± 1.2
10Cl	10	0	2.1 ± 0.7

$C_nH_{2n+1}N^+(CH_3)_3 \cdot Br^-$

$x=3.0\times10^{-3}$ mol/l in ETHANOL
S=∿ 1 mm/s
T=22.5∿ 24.5 °C

CODES	n	Θ(deg)	B_θ ($\times10^{-3}$erg/cm^2)
14Br	14	0	∿9
12Br	12	0	∿7
10Br	10	∿0	4.4 ± 0.7
8Br	8	∿75	<1
6Br	6	∿75	<1

$C_nF_{2n+1}SO_2NHCH_2CH_2CH_2N^+(CH_3)_3 \cdot I^-$

$x=6.9\times10^{-4}$ mol/l in WATER
S=∿ 300 mm/s
T=23.0∿ 23.5 °C

CODES	n	Θ(deg)	B_θ ($\times10^{-3}$erg/cm^2)
FS150	8	0	10 ± 2

(c) NONIONIC SURFACTANTS

$C_nH_{2n+1}NH_2$

$x=3.0\times10^{-2}$ mol/l in ETHANOL
S=∿ 300 mm/s
T=22.0∿24.0 °C

CODES	n	Θ(deg)	B_θ ($\times10^{-3}$erg/cm^2)
18A	18	0	2.5 ± 0.6
16A	16	0	3.5 ± 1.2
14A	14	0	4.0 ± 0.7
12A	12	∿ 3	>1.5
10A	10	∿ 3	>1.9
8A	8	∿12	∿0.32
6A	6	∿24	∿0.22

$C_nH_{2n+1}OH$

$x=4.1\times10^{-3}$ mol/l in ETHANOL
S=∿ 300 mm/s
T=23.0 °C

CODES	n	Θ(deg)	B_θ ($\times10^{-3}$erg/cm^2)
16OH	16	0	∿4.8

(d) AMPHOTERIC SURFACTANTS

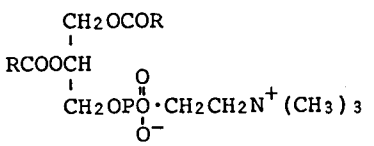

x=0.1 wt% in n-HEXANE
S=∿ 300 mm/s
T=22.5∿23.0 °C

CODES	Θ(deg)	B_θ ($\times10^{-3}$erg/cm^2)
LECITHIN	0	5.9 ± 1.3

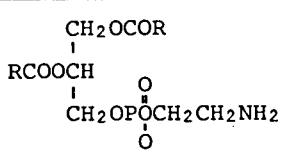

x=0.1 wt% in n-HEXANE
S=∿ 300 mm/s
T=24.0 °C

CODES	Θ(deg)	B_θ ($\times10^{-3}$erg/cm^2)
CEPHARIN	∿5	∿6.3

A summary of experimental results is given in Table 4-2. Table 4-2(a) presents derived anchoring parameters for homologous series of *n*,*n*-dimethyl-*n*-alkyl-3-aminopropyltrimethoxysilyl chloride nS (n = 10,12,14,16,18, n corresponds to the number of carbon atoms in alkyl chain), which have both chemisorption group $-Si(OCH_3)_3$ and cationic physisorption group $R-N^+(CH_3)_2CH_2CH_2CH_2-$. The result for *n*-alkyltriethoxysilane 18AS with one chemisorption group $-Si(OC_2H_5)_3$ is also presented. The angle $\Theta = 0°$ was obtained for all the examined nS ($n \geq 10$). The B_θ values for these materials are on the order of 10^{-2} erg/cm^2 and B_θ becomes maximum for n = 14 or 16. The n-dependence of B_θ for nS is shown in Fig. 4-5. For 18AS, $\Theta = 0°$ and comparatively small B_θ ($(2.2 \pm 0.8) \times 10^{-3}$ erg/cm^2) were obtained.

Table 4-2(b) shows the results for cationic surfactants, *n*-alkyltrimethylammonium halide nCl (n = 10,12,16,18) and nBr (n = 6,8, 10,12,14) with hydrocarbon chain containing n carbon atoms and FS150 with perfluorocarbon chain containing 8 carbon atoms. The angle $\Theta = 0°$ was obtained in $n \geq 10$ cases for hydrocarbon materials nCl and nBr and even in n = 8 case for perfluorocarbon material FS150. (The angle $\Theta = 0°$ was also obtained for another material, FC805, with perfluorocarbon chain containing 8 carbon atoms (see Table 5-7).) The B_θ values are on the order of 10^{-3} erg/cm^2 for nCl and nBr ($n \geq 10$). They also depend on alkyl chain length and exhibit a maximum for n = 14 or 16. FS150 shows larger B_θ ($(10 \pm 2) \times 10^{-3}$ erg/cm^2) than maximum B_θ for nCl and nBr (see Fig. 4-5). In case of n = 8 or 6, Θ value is rather large and therefore ϕ - dependent interaction term takes part in molecular aligning forces. This brings about a conical configuration or texture (Fig. 4-6). This configuration is strongly affected by the liquid-crystal molecule flow. Polarized microscopic observation gives a director distribution drawing, as shown in Fig. 4-6. Parallel dark lines in the liquid-crystal flow direction (x-axis) indicate $\partial\phi/\partial x \simeq 0$. Their darkness becomes maximum under the crossed-nicols condition, that means $\partial\phi/\partial z = 0$. $\partial\phi/\partial y = 2\pi/c\ell$ (*c* is

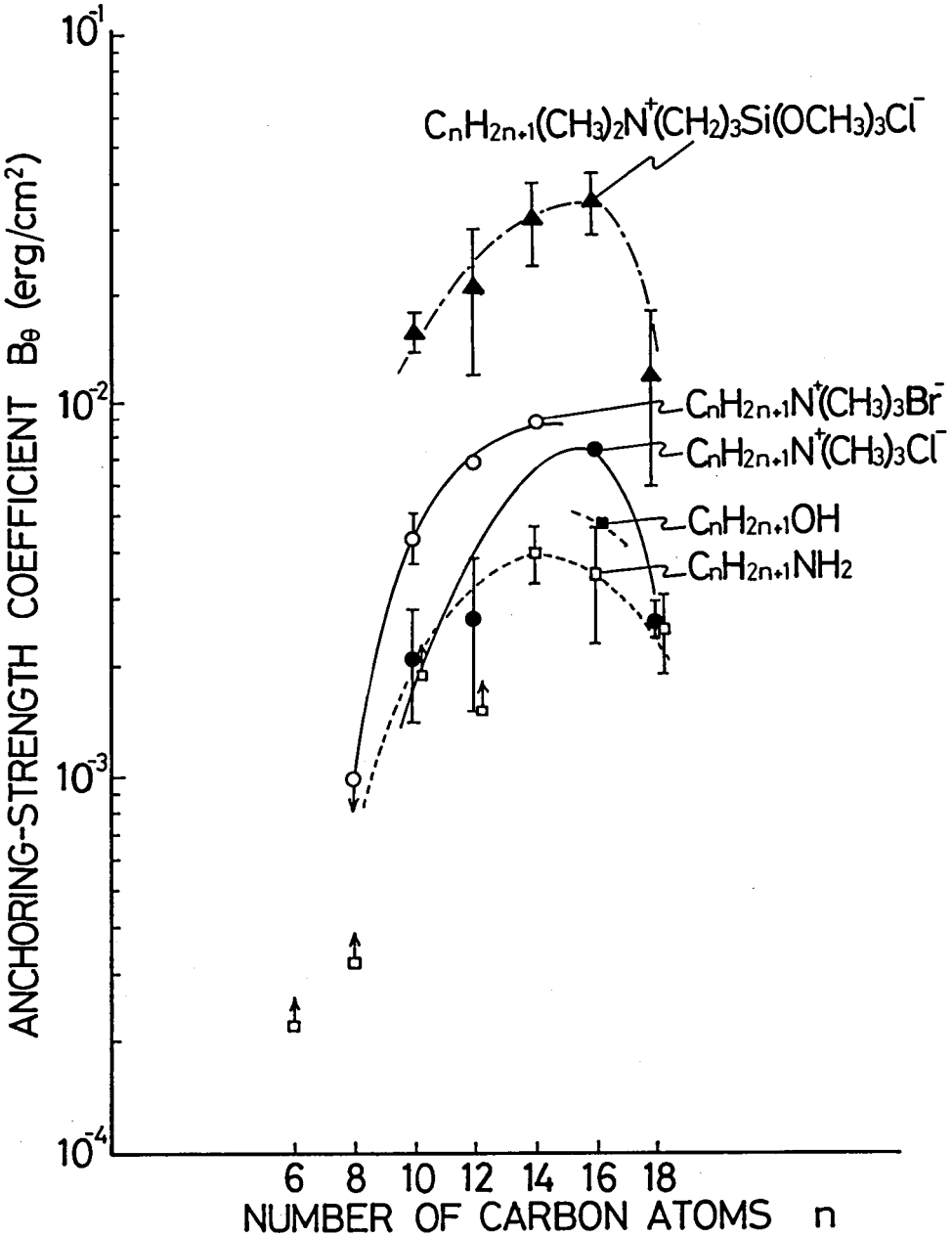

Fig. 4-5 Relations between anchoring-strength coefficient B_θ and number of carbon atoms n in surfactant alkyl chain.

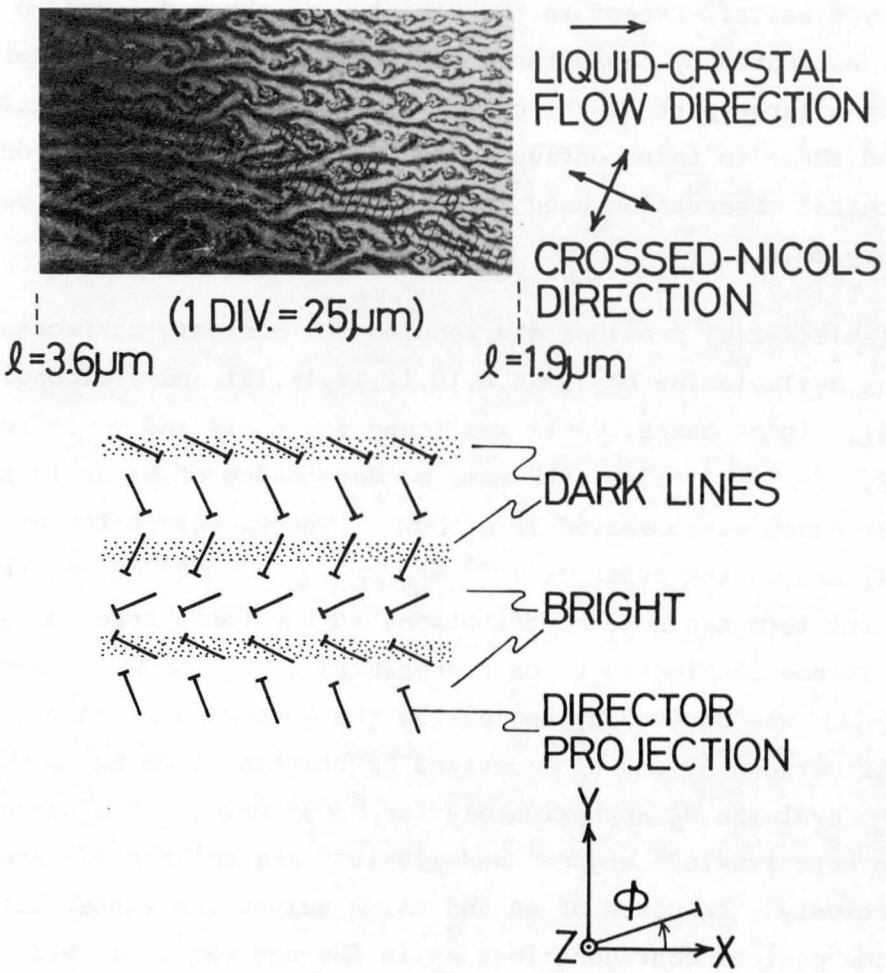

Fig. 4-6 Polarized-microscopic observation of conical configuration (wedge cell, *n*-hexyltrimethylammonium bromide).

a constant) is obtained by the observation for a wedge cell. In case of larger ℓ values, $\partial\phi/\partial y$ becomes nearly equal to zero and the configuration is something like a planar structure. Thermal treatment breaks the conical configuration. If the cell is heated above the nematic → isotropic transition temperature and then cooled slowly under a magnetic field perpendicular to the substrates, a different configuration is obtained. In this configuration, several regions

of different ϕ values are divided by surface disclination lines and Néel type walls. Except in the vicinity of those defects, Θ value can be estimated by capacitance measurements with the assumption of $\theta = \Theta$ in a large part of the cell. The angle $\Theta = 75°$ was obtained for 6Br and 8Br. In this configuration, B_θ values were estimated by the topological observation used in ref. 6. They are of the order of 10^{-4} erg/cm^2.

Table 4-2(c) provides the results for nonionic surfactants, such as *n*-alkylamine nA (n = 6,8,10,12,14,16,18) and *n*-alcohol nOH (n = 16). In nA cases, $\Theta = 0°$ was found for n = 14 and $\Theta \simeq 3°$ for n = 10 and 12. In $\Theta = 0°$ cases, the same n-dependence of B_θ as in nS, nCl, and nBr cases was observed (Fig. 4-5). The B_θ values for nA and nOH ($n \geqq 14$) are on the order of 10^{-3} erg/cm^2. In $\Theta \neq 0°$ cases, the ϕ-dependent term has some contributions to the total free energy, which is now considered to be represented by Eq. (2-11). Although Eq. (2-11) was derived by neglecting the ϕ-dependent term, the relations between B_θ and H_c', derived by starting from Eq. (2-11), were used to evaluate B_θ approximately for $\Theta \simeq 3°$ cases. Evaluated B_θ values were 1.5×10^{-3} erg/cm^2 and 1.9×10^{-3} erg/cm^2 for 12A and 10A, respectively. In cases of 6A and 8A, Θ values are rather large and the same conical configurations as in 6Br and 8Br cases were observed. The Θ values were estimated to be about 12° for 8A and about 24° for 6A by the same capacitance measurements that were used for 6Br and 8Br. The Néel-type-wall widths give B_θ estimations of 3.2×10^{-4} erg/cm^2 and 2.2×10^{-4} erg/cm^2 for 8A and 6A, respectively.

Table 4-2(d) presents the results for amphoteric surfactants, Lecithin and Cepharin. The anchoring-parameter values were found to be $\Theta = 0°$ and $B_\theta = (5.9 \pm 1.3)\times10^{-3}$ erg/cm^2 for Lecithin and $\Theta = \sim5°$ and $B_\theta = 6.3\times10^{-3}$ erg/cm^2 for Cepharin.

Throughout the results in Table 4-2, the n-dependence of B_θ

was clearly shown and B_θ values were found to be larger for silanes nS than cationic surfactants nBr and nCl with the same chain length, and B_θ values for nonionic surfactants nA and nOH are the smallest. The comparatively large B_θ values for nS are considered not to be the result of chemisorption group $-Si(OCH_3)_3$ only. The reason is found in Table 4-2(a), where B_θ for 18AS is shown not to be as large as 18S and to be comparative with 18Cl or 18A. Comparison of B_θ values for these materials, 18A, 18Cl, 18AS, and 18S, are again shown in Fig. 4-7 .

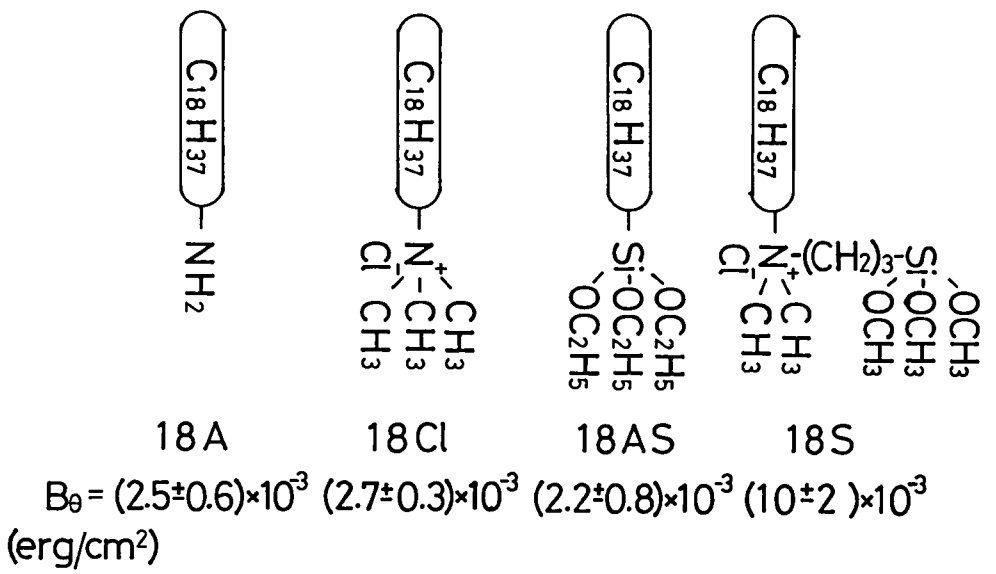

Fig. 4-7 Molecular structures and anchoring-strength coefficients B_θ for surfactants 18A, 18Cl, 18AS, and 18S.

4-4-2. Substrate-material effects on anchoring parameters

In order to examine substrate-material effects on anchoring parameters, Θ and B_θ were derived for MBBA on bare glass substrates with some surfactant layers used before. The total-reflection meth-

od was used for Θ and H_c' measurements.

Figure 4-8 shows a typical experimental result for 18S as a surfactant. Figure 4-8(a) shows a result of the Freedericksz-transition measurement which gives the threshold magnetic field $H_c' = 1.70$ kOe. The result of Θ measurement is shown in Fig. 4-8(b) which gives $\Theta = 0°$.

In repetition of these measurements for samples with various thickness ℓ, B_θ for 18S was found to be 6.1×10^{-3} erg/cm^2. The derived Θ and B_θ values for several surfactants are listed in Table 4-3. The B_θ values for the insulating glass substrates are smaller than those for the In_2O_3 - evaporated conductive substrates.

In addition, the principal refractive indices are determined from the measured values of Θ, ψ_{co}, and ψ_{ce} under zero magnetic field. Values of $n_o = 1.540$ and $n_e = 1.753$ were obtained for MBBA from the data in Fig. 4-8. These values are in good agreement with previously reported values[7]. This fact guarantees the accuracy of the present total-reflection method.

Table 4-3 Derived easy-axis angles Θ and anchoring-strength coefficients B_θ on interfaces between MBBA and substrates with various surfactants.

SURFACTANTS	In_2O_3/GLASS		GLASS	
	Θ(deg)	B_θ(erg/cm^2)	Θ(deg)	B_θ(erg/cm^2)
FS150	0	$1.0\pm0.2\times10^{-2}$	0	6.4×10^{-3}
18S	0	$1.1\pm0.4\times10^{-2}$	0	6.1×10^{-3}
LECITHIN	0	$5.9\pm1.3\times10^{-3}$	0	3.1×10^{-3}
HEXADECYLAMINE	0	$3.5\pm1.2\times10^{-3}$	0	2.6×10^{-3}

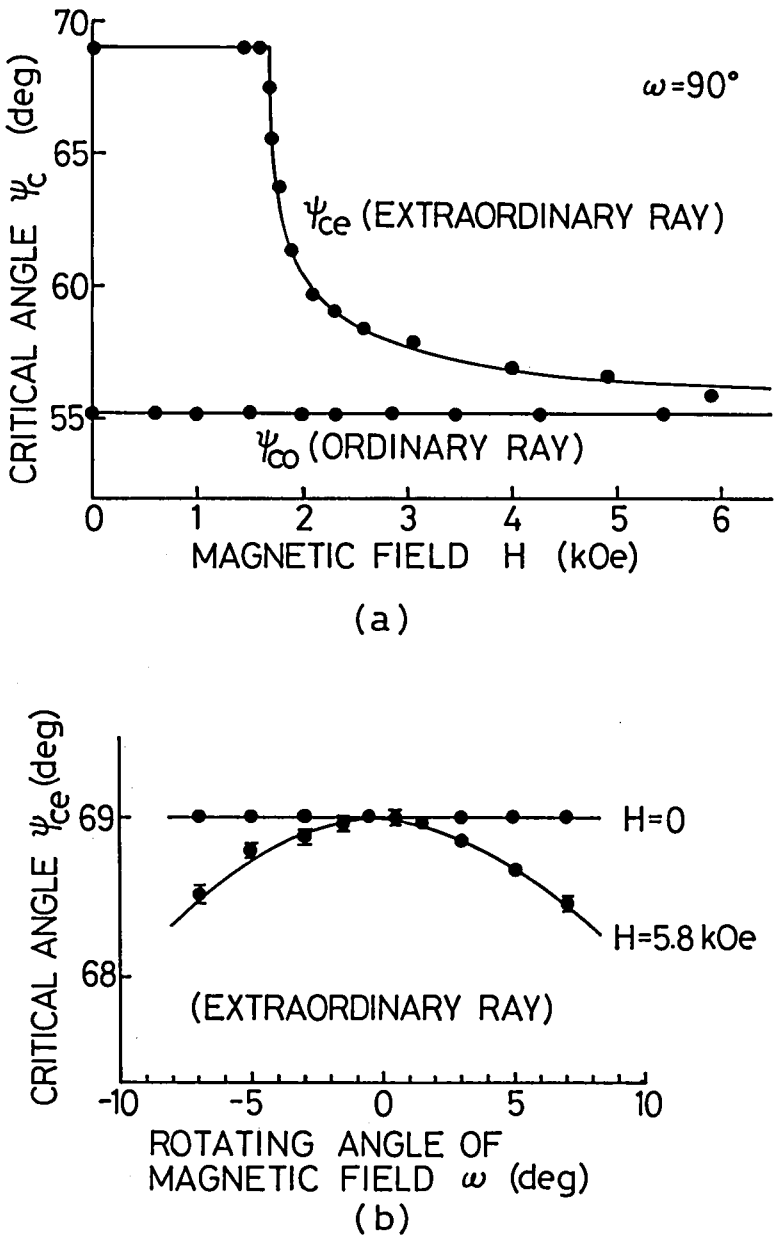

Fig.4-8 Observed changes in the critical angle of total reflection for MBBA/18S/LaSF-08 glass sample at room temperature (25.0 ± 0.5 °C), cell thickness is 49.0 μm. (a) Critical angle of total reflection for both an ordinary ray and an extraordinary ray (λ = 6328 Å) as a function of the applied magnetic field (ω = 90°) and (b) critical angle of total reflection for an extraordinary ray (λ = 6328 Å) as a function of the rotating angle of magnetic fields (H = 0, 5.8 kOe).

4-5. Discussions

In order to assure precise discussions on measured B_θ values in regard to surfactant molecular structures, much more information is needed, such as adsorbed molecular density, and it is necessary to consider differences in substrate surface smoothness, for example, in discussing substrate-material effects.

Although some uncertainty remains, as mentioned above, the experimental results in this section show the following tendency. Easy-axis angle θ value is zero (homeotropic alignment) for the long-chain surfactants and increases as chain length decreases. The necessary chain length for MBBA homeotropic alignment is on the order of $n \geqq 10$ for hydrocarbon chains. For perfluorocarbon chains, $n = 8$ seems to be enough. Anchoring-strength coefficient B_θ depends on both the hydrophobic chain and the hydrophilic group of the surfactants. That is, decreasing the chain length makes B_θ value smaller, and B_θ values for cationic surfactants are larger than those for nonionic surfactants of the same chain length. Moreover, B_θ values for surfactants with two adsorption groups are larger than those for surfactants with one adsorption group. Also, substrate materials influence B_θ. That is, for cationic surfactants, glass substrates reduce B_θ values by almost half as compared with In_2O_3 - evaporated glass substrates. These results help in understanding mechanisms of liquid-crystal molecular alignment on substrates.

One explanation for the relations between θ and n is what is called steric effects. It is known that liquid-crystal molecules align homeotropically, when the alkyl chains of surfactants are perpendicular on the substrate, and align parallel when they are parallel on the substrate[3]. It is considered that surfactant alkyl chains tend to align perpendicular if they are sufficiently long, and liquid-crystal molecules lie parallel to the chains because of

dispersive forces. Actually, the long alkyl chains of surfactants were found to be aligning perpendicular on the substrate. Figures 4-9(a) and (b) show reflective electron diffraction patterns for In_2O_3 - evaporated substrates without surfactants and with *n*-tetradecyltrimethylammonium bromide layer, respectively. Figure 4-9(b) shows a vertical line of spots, which suggests a perpendicular alignment of alkyl chains on the substrate.

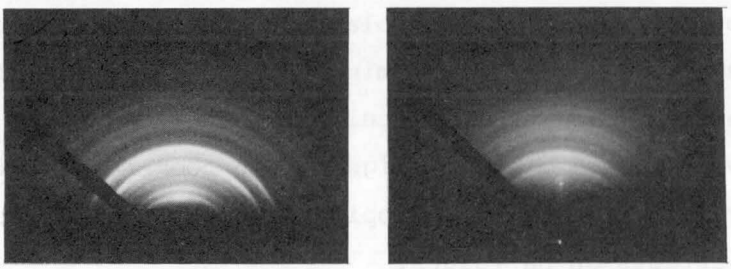

(a) (b)

Fig. 4-9 Reflective electron-diffraction patterns. (a) In_2O_3 - evaporated glass surface and (b) *n*-tetradecyltrimethylammonium bromide layer on In_2O_3 - evaporated glass.

Observed n - dependence of B_θ introduces a hypothesis in regard to screening effect. That is, although substrate materials have such effects on B_θ as mentioned in Section 4-4-2, surfactant layers act to screen the substrate surface potential. If surfactant alkyl chain is short and lies parallel to a substrate surface, the surfactant-layer screening effect is weak and independent of surfactant alkyl-chain length. When surfactant alkyl chain is long and lies perpendicular to a substrate surface, the substrate surface potential is screened effectively and the screening effect depends on the surfactant alkyl-chain length. In longer alkyl chain cases, the alkyl chain increases in flexibility and the screening effect is considered to rather decrease.

The surfactant polar group effects and the substrate-material

effects on B_θ values suggest that polar interactions play several roles in the molecular aligning forces. According to Proust *et al.* [8], dipole↔dipole interactions are dominant in the liquid-crystal molecular alignment at a humid glass surface. The dipole↔dipole interaction acts to align MBBA molecules parallel on such a glass substrate. The glass substrate surface potential, which produces MBBA parallel alignment, is screened by a surfactant layer with alkyl chains, and actual MBBA alignment on the surfactant layer is determined by a balance between polar and nonpolar (dispersive) forces. Dispersive forces are dominant in the interfacial interactions between liquid-crystal molecules and the long-chain surfactant layer, and promote homeotropic alignment in cooperation with steric effects. Even in case of homeotropic alignment, polar interactions have latent effects on B_θ values.

The above discussions suggest that it is important to consider the surface energy of surface-treated substrates by dissociating polar and nonpolar components. This consideration is developed in the following Sections V∿VII.

4-6. Summary

In this section, the equipment used for the anchoring-parameters measurements has been described and shown graphically. The liquid-crystal anchoring parameters, Θ and B_θ, have been derived on various surface-treated substrates. The results are summarized as follows:

1) liquid-crystal interfacial alignment angle θ_0 is affected by surfactant alkyl-chain length, and the angle θ_0 is 0° (homeotropic alignment, $\Theta = 0°$) for long-chain surfactants (typically $n \geqq 10$) and increases as chain length decreases,

2) the liquid-crystal anchoring strength is affected by surfactant alkyl-chain length and shows maximum value when $n = 14$ or $n = 16$,

3) the liquid-crystal anchoring strength also depends on surfactant adsorption group properties, and B_θ values for cationic surfactants are slightly larger than those for nonionic surfactants of the same chain length, and

4) for cationic surfactants, polished glass substrates reduce the liquid-crystal anchoring strength by almost half as compared with In_2O_3 - evaporated glass substrates.

For the n - dependence of Θ and B_θ, (1) and (2), a hypothesis has been presented concerning a surfactant layer screening effect. Moreover, substrate-surface energy considerations by dissociating polar and nonpolar components have been suggested to be necessary for understanding liquid-crystal alignment mechanisms, including polar force effects (3) and (4).

References

[1] Surfactant FS150 is commercially available as "Surfin-150" from Dainippon Ink and Chemicals, Inc.

[2] Silanes 10S, 12S, 14S, and 16S were produced experimentally, and 18S is commercially available as "SRX-679".

[3] J. E. Proust, L. Ter-Minassian-Saraga, and E. Guyon, Solid State Commun., 11, 1227 (1972)

[4] W. H. de Jeu, W. A. P. Claassen, and A. M. J. Spruijt, Mol. Cryst. Liq. Cryst., 37, 269 (1976)

[5] H. Gasparoux and J. Prost, J. Phys. (Paris), 32, 953 (1971)

[6] G. Porte, J. Phys. (Paris), 37, 1245 (1976)

[7] I. Haller, H. A. Huggins, and M. J. Freiser, Mol. Cryst. Liq. Cryst., 16, 53 (1972)

[8] J. E. Proust and L. Ter-Minassian-Saraga, J. Phys. (Paris), C1-36, C1-77 (1975)

V. EXPERIMENTAL INVESTIGATIONS ON RELATIONS BETWEEN INTERFACIAL ALIGNMENT ANGLE AND SUBSTRATE SURFACE ENERGIES

5-1. Introduction

The experimental results in Section IV suggest that both polar and nonpolar forces play individual roles in liquid-crystal interfacial alignment mechanisms. The knowledge, concerning which kind of interaction force is dominant for each interface between liquid-crystals and surface-treated substrates, will be a great help for understanding the liquid-crystal alignment mechanisms and improving substrate-surface treatment procedures for desirable liquid-crystal interfacial alignment conditions. For this purpose, this section reports results of measuring polar and nonpolar surface-energy components separately for various surface-treated substrates. Their compositions were investigated in comparison with liquid-crystal alignment angles at those substrate surfaces.

Section 5-2 presents principles of substrate surface-energy measurements, separating its polar and nonpolar components. Section 5-3 is devoted to explaining the materials used and sample preparation procedures. The relationships were obtained between liquid-crystal alignment angles and surface-energy components for substrates treated with various concentration of surfactant solutions. Other relationships were observed between liquid-crystal alignment angles and surface-energy components of substrates with various surfactant materials. These experimental results are presented in Section 5-4 and discussions are given in Section 5-5. Section 5-6 summarizes the experimental investigations in Section V.

5-2. Principle of Substrate Surface-Energy Measurements

Polar components γ_S^p and nonpolar components γ_S^d for substrate surface-energies are determined by measuring polar-liquid contact-angles α. The principle is as follows. A liquid substrate interfacial energy W_{SL} is represented as

$$W_{SL} = \gamma_S + \gamma_L - W_a \quad , \tag{5-1}$$

by using substrate surface-energy γ_S, liquid surface-energy γ_L, and work of adhesion W_a. Each term in Eq. (5-1) consists of various components, such as London dispersion force, dipole↔dipole interactions, hydrogen bonding interactions, π-bonding interactions, etc. When it is assumed that the dispersion-force origin is independent of that of the other interaction forces and that a dispersion-force component and the total of the other interaction-force components are additive, it is possible to express each term in Eq. (5-1) as follows:

$$\begin{aligned} \gamma_S &= \gamma_S^d + \gamma_S^p \quad , \\ \gamma_L &= \gamma_L^d + \gamma_L^p \quad , \\ W_a &= W_a^d + W_a^p \quad , \end{aligned} \tag{5-2}$$

where superscripts d and p mean the dispersion (nonpolar) component and the total of polar components, respectively. When the liquid substrate interaction forces are entirely dispersion forces, Fowkes [1] derived a formula,

$$W_{SL}^d = \gamma_S^d + \gamma_L^d - 2(\gamma_S^d \gamma_L^d)^{1/2} \quad , \tag{5-3}$$

that is,

$$W_a^d = 2(\gamma_S^d \gamma_L^d)^{1/2} \quad . \tag{5-4}$$

For W_a^p, it can be written as

$$W_a^p = W_a^{p\text{-}p} + W_a^{p\text{-}i} + W_a^b \quad , \tag{5-5}$$

where $W_a^{p\text{-}p}$ is the dipole↔dipole component, $W_a^{p\text{-}i}$ the dipole↔in-

duced-dipole component and W_a^b the total of various bonding components. Because the tested polar liquids in this study (see Table 5-1) possess neither steric structures, which hinder the proximity of permanent dipoles, nor groups with large polarizabilities, W_a^{p-i} is considered to be smaller than W_a^{p-p} as generally accepted for ordinary polar liquids. For the present tested liquids, moreover, the origin of W_a^b, if any, is considered to be caused by hydrogen bondings, which are usually considered to be electrostatic interactions between the pertinent groups. In Eq. (5-5), the dipole $\leftrightarrow$ dipole interaction components for the electrostatic intermolecular forces are introduced totally as W_a^{p-p}. In neglecting multipole contributions to the electrostatic interactions, therefore, it is possible to omit the bonding-interaction term W_a^b. Thus, as a first approximation, only the dipole $\leftrightarrow$ dipole interaction component is considered as the polar intermolecular force. For W_a^{p-p}, Wu[2] gave a formula,

$$W_a^{p-p} = 2(\gamma_S^p \gamma_L^p)^{1/2} \quad , \tag{5-6}$$

using a semi-continuum model. When considering both London dispersion and dipole $\leftrightarrow$ dipole interaction components as predominant liquid substrate interfacial energies and using the energy additivity concept, the following formula is obtained:

$$W_{SL} = \gamma_S + \gamma_L - 2[(\gamma_S^d \gamma_L^d)^{1/2} + (\gamma_S^p \gamma_L^p)^{1/2}] \quad . \tag{5-7}$$

On the other hand, W_{SL} is related to liquid contact-angle α by the formula,

$$W_{SL} = \gamma_S - \gamma_L \cos \alpha \quad . \tag{5-8}$$

By combining Eqs. (5-7) and (5-8), we have

$$1 + \cos\alpha = 2[(\gamma_S^d \gamma_L^d)^{1/2} + (\gamma_S^p \gamma_L^p)^{1/2}] / \gamma_L \quad . \tag{5-9}$$

By using Eq. (5-9) and the least square method, it is possible to determine γ_S^d and γ_S^p.

Liquids (Tokyo Chemical Industry Co., Ltd.) used for the con-

tact-angle measurements are listed in Table 5-1, together with their polar components γ_L^p and nonpolar components γ_L^d of surface energies [1,3]. Contact angles α were calculated using the following equation,

$$\alpha = 2 \arctan (2h/d) \ . \qquad (5\text{-}10)$$

Height h and diameter d values for a sessile drop on a substrate were measured from a photograph taken with a contact-angle meter, as shown in Fig. 5-1 .

Table 5-1 Liquid surface energies (from Refs. 1 and 3).

No.	LIQUIDS	SURFACE ENERGIES (erg/cm^2) γ_L^d	γ_L^p	γ_L
I	WATER	22.0	50.2	72.2
II	GLYCEROL	34.0	30.0	64.0
III	FORMAMIDE	32.3	26.0	58.3
IV	di-IODOMETHANE	48.5	2.3	50.8
V	α-BROMONAPHTHALENE	44.6	0.0	44.6
VI	n-HEXADECANE	27.6	0.0	27.6
VII	n-TETRADECANE	26.7	0.0	26.7
VIII	n-DODECANE	25.4	0.0	25.4
IX	n-DECANE	23.9	0.0	23.9
X	n-OCTANE	21.8	0.0	21.8
XI	n-HEXANE	18.4	0.0	18.4

5-3. Sample Preparation

Substrates used are bare and In_2O_3 - evaporated glass plates. The substrates were coated with organic layers. The organic layer

(a)

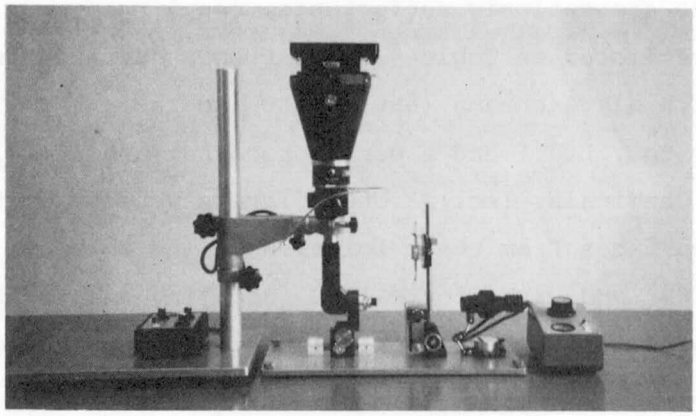

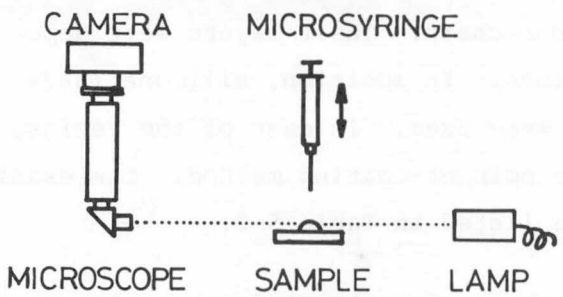

(b)

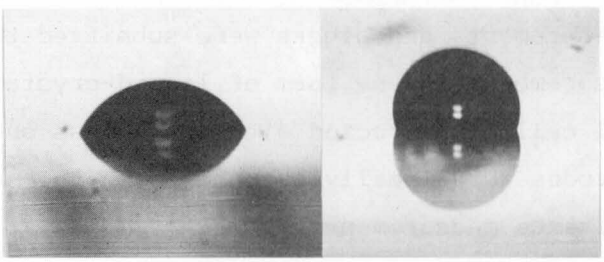

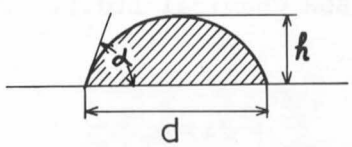

$$\alpha = 2\tan^{-1}(2h/d)$$

Fig. 5-1 Contact-angle measurement set-up.
(a) Contact-angle meter and (b) example photographs taken by this contact-angle meter.

materials are cationic surfactants, coupling agents, and resins, which are listed in Table 5-2. Cationic surfactants are ammonium salts with alkyl chains (6Br and 8Br in Table 5-2, Tokyo Chemical Industry Co., Ltd.) and a perfluorocarbon chain (FS150, Dainippon Ink and Chemicals, Inc.). Their layers were deposited on the substrate surfaces from their solutions. The solvents are ethanol for 6Br and 8Br and water for FS150. Coupling agents are homologous series of silanes nS (n = 10,12,14,16,18, Toray Silicone Co., Ltd.), a chromium complex (Edoran, Mitsubishi Gas Chemical Co., Ltd.) with alkyl chains, and another chromium complex (FC805, 3M Co.) with a perfluorocarbon chain. Their layers were deposited using their aqueous solutions. In addition, silicone (SR2411, Toray Industries, Inc.) resins were used. In case of the resins, the layers were formed by the spinner-coating method. The examined organic-layer materials are listed in Table 5-2.

Some of the surface-treated substrates were submitted to contact-angle measurements and others were submitted to liquid-crystal alignment measurements in the form of liquid-crystal cells. In the liquid-crystal cells constructed with bare glass substrates, In_2O_3 monitor electrodes were locally evaporated on the substrates for magneto-capacitance measurements.

Liquid-crystal materials used are 4'-methoxybenzylidene-4-*n*-butyl-aniline (MBBA, Fuji Pigment Co., Ltd.) and 4-cyano-4'-*n*-pentylbiphenyl (5CB, BDH Chemical Ltd.). Their molecular structures are shown in Fig. 5-2 .

5-4. Experimental Results

5-4-1. Concentration effects of surfactant solution

Surface-energy components γ_S^d and γ_S^p for bare glass substrates

Table 5-2 Examined organic layer materials.

CODES	FORMULAS
SURFACTANTS	
6Br	$C_6H_{13}N^+(CH_3)_3Br^-$
8Br	$C_8H_{17}N^+(CH_3)_3Br^-$
FS150	$C_8F_{17}SO_2NHCH_2CH_2CH_2N^+(CH_3)_3I^-$
COUPLING AGENTS	
10S	$[C_{10}H_{21}(CH_3)_2NCH_2CH_2CH_2Si(OCH_3)_3]^+Cl^-$
12S	$[C_{12}H_{25}(CH_3)_2NCH_2CH_2CH_2Si(OCH_3)_3]^+Cl^-$
14S	$[C_{14}H_{29}(CH_3)_2NCH_2CH_2CH_2Si(OCH_3)_3]^+Cl^-$
16S	$[C_{16}H_{33}(CH_3)_2NCH_2CH_2CH_2Si(OCH_3)_3]^+Cl^-$
18S	$[C_{18}H_{37}(CH_3)_2NCH_2CH_2CH_2Si(OCH_3)_3]^+Cl^-$
EDORAN	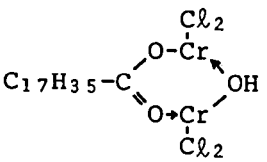
FC805	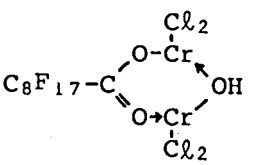
RESINS	
SR2411	SILICONE
VERSAMID940	POLYAMIDE
TORAYNEECE	POLYIMIDE

treated with 12S and FS150 solutions of various molarities x(mol/l) were obtained by using the method described in Section 5-2. Measured contact-angle values α are shown in Tables 5-3 and 5-4, and derived x-dependence of surface-energy components, γ_S^p and γ_S^d, is shown in

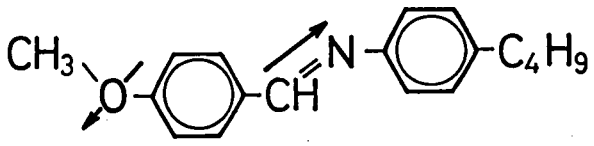

(a)

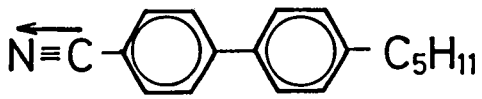

(b)

Fig.5-2 Molecular structures for MBBA and 5CB. (a) MBBA, (b) 5CB.

Figs. 5-3 and 5-4. In the case of 12S-treated glass substrates (Fig. 5-3), γ_S^d slightly increases as x for the region where $x \geqq 6\times10^{-5}$, whereas γ_S^p decreases as x in the region $10^{-5} \lesssim x \lesssim 10^{-4}$, and becomes very small and constant for $x > 10^{-4}$. On the other hand, in the case of FS150-treated glass substrates (Fig. 5-4), both γ_S^d and γ_S^p values decrease as x in the region $4\times10^{-7} \lesssim x \lesssim 10^{-5}$ and saturate for $x > 4\times10^{-5}$. For the saturated values, γ_S^d is smaller than γ_S^p, in contrast to the case of 12S treatments.

Alignment angles θ_0 for MBBA and 5CB were measured at the same glass surfaces as used in the above-mentioned contact-angle measurements, by utilizing the monitor electrodes and using the magneto-capacitance method described in Section 3-2-1. The determined values are listed in Table 5-5. The x-dependence of θ_0 values is also shown in Figs. 5-3 and 5-4 for easy comparison with the previously measured x-dependence of γ_S^d and γ_S^p values. In Figs. 5-3 and 5-4, it is found that uniform liquid-crystal alignments with different θ_0 values (0° and 90° for MBBA and 0° and 23° for 5CB) are obtained for substrates with different surface-energy components. The following two subsections describe the MBBA and 5CB alignment-angle measurements in detail.

Table 5-3 Measured liquid contact-angles on 12S-treated glass substrates.

LIQUIDS	CONTACT ANGLES α (deg)					
	12S MOLARITY x (mol/l)					
	0.0	1.2×10^{-5}	5.9×10^{-5}	1.2×10^{-4}	5.9×10^{-4}	1.2×10^{-3}
WATER	3.5	10.6	38.6	73.6	78.9	84.7
GLYCEROL	9.1	16.4	34.8	67.5	74.3	73.3
FORMAMIDE	3.5	4.4	31.3	50.0	61.1	57.4
di-IODOMETHANE	46.8	47.5	48.4	52.4	53.0	51.9
α-BROMONAPHTHALENE	10.7	11.2	13.2	20.7	34.4	35.6

Table 5-4 Measured liquid contact-angles on FS150-treated glass substrates.

LIQUIDS	CONTACT ANGLES α (deg)							
	FS150 MOLARITY x (mol/l)							
	1.3×10^{-7}	3.9×10^{-7}	1.3×10^{-6}	3.9×10^{-6}	1.3×10^{-5}	3.9×10^{-5}	1.3×10^{-4}	3.9×10^{-4}
WATER	16.9	10.6	20.0	41.2	61.1	69.1	66.9	71.3
GLYCEROL	14.5	28.8	33.8	57.0	77.7	88.3	83.8	83.6
FORMAMIDE	8.6	12.5	23.3	39.4	48.9	52.6	52.6	53.4
di-IODOMETHANE	44.8	53.1	53.7	66.8	89.2	93.8	94.4	98.5
α-BROMONAPHTHALENE	14.2	24.0	28.5	55.0	79.2	89.5	90.1	88.9

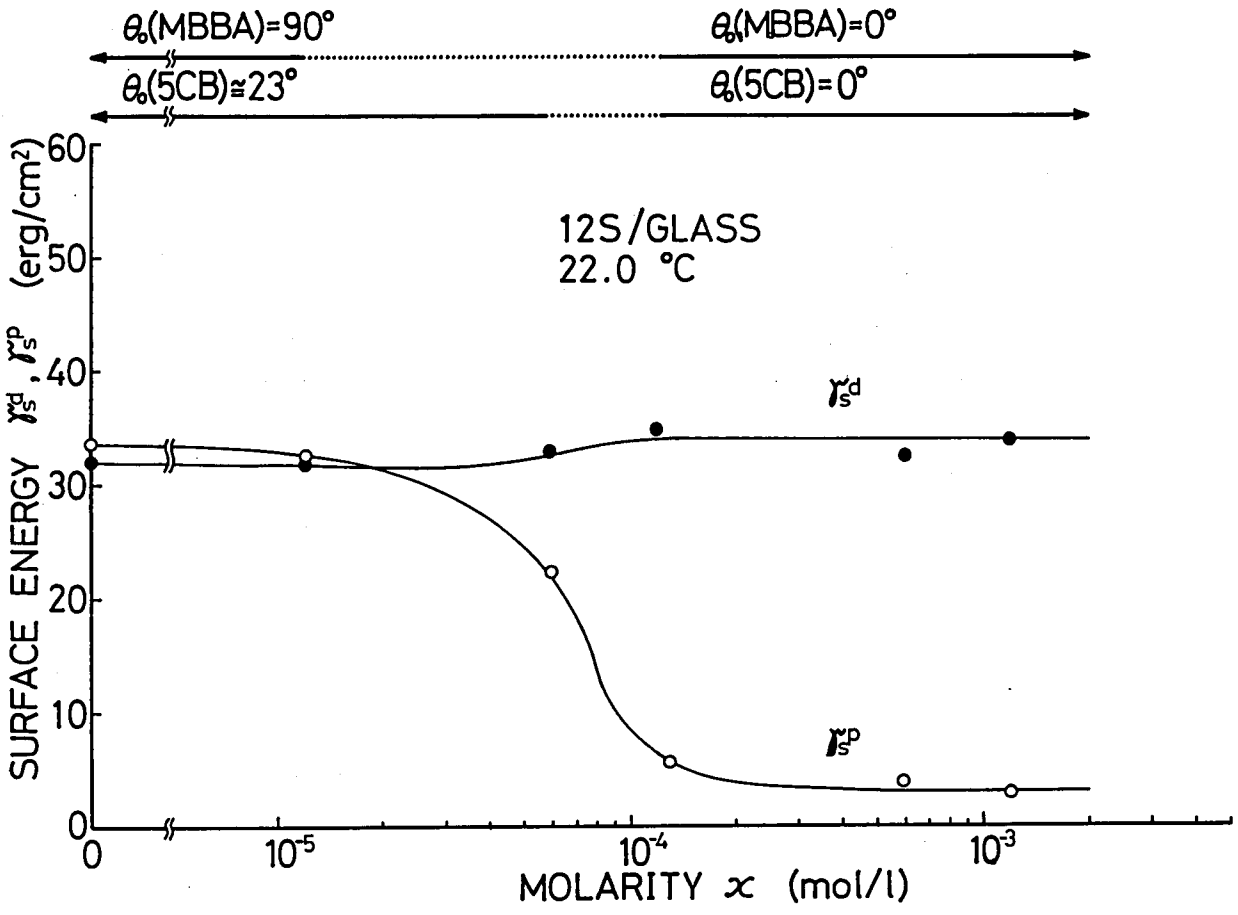

Fig. 5-3 Measured substrate surface-energy γ_S^d and γ_S^p versus surfactant 12S molarity x in solution for surface treatment.

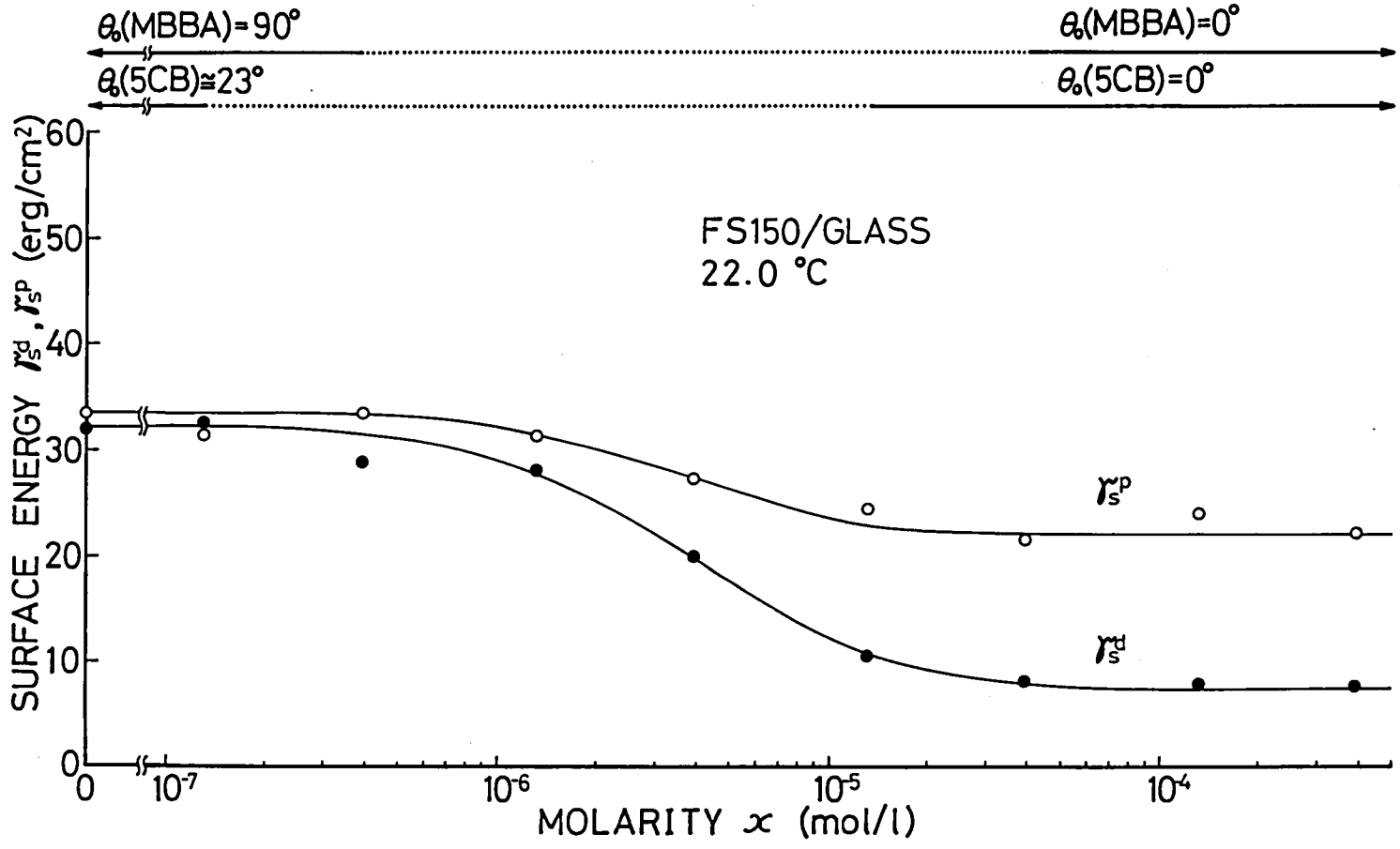

Fig. 5-4 Measured substrate surface-energy γ_S^d and γ_S^p versus surfactant FS150 molarity x in solution for surface treatment.

Table 5-5 Determined liquid-crystal interfacial alignment angles.

LIQUID CRYSTALS	INTERFACIAL ALIGNMENT ANGLES θ_0 (deg)							
	12S MOLARITY x (mol/l)							
	0.0	1.2×10^{-5}	5.9×10^{-5}	1.2×10^{-4}	5.9×10^{-4}	1.2×10^{-3}		
MBBA	90	90	X	0	0	0		
5CB	23	23	23	0	0	0		
	FS150 MOLARITY x (mol/l)							
	1.3×10^{-7}	3.9×10^{-7}	1.3×10^{-6}	3.9×10^{-6}	1.3×10^{-5}	3.9×10^{-5}	1.3×10^{-4}	3.9×10^{-4}
MBBA	90	90	X	X	X	0	0	0
5CB	23	X	X	X	0	0	0	0

X; NON-UNIFORM ALIGNMENTS

i. MBBA alignment angles

The values of ω_0 were measured at 0° for 12S-treated glass substrate with $x \geqq 1.2\times10^{-4}$ and for FS150-treated glass substrate with $x \geqq 3.9\times10^{-5}$. For these cases, $\theta_0 = 0°$ is uniquely obtained from Fig. 3-3, and homeotropic alignments ($\theta_0 = 0°$) were conoscopically confirmed. When x is smaller, on the contrary, the liquid-crystal alignment was strongly affected by the liquid-crystal flow at the injection into a cell. In polarized microscopic observations under the crossed-nicols condition, the darkest field was obtained when the liquid-crystal flow direction (x-axis in Fig. 3-2) coincided with one of the nicol directions, and the field became brightest when the crossed-nicols were rotated 45°. From this observation, it was concluded that $\phi = 0°$[4] and, therefore, $\partial\theta/\partial x = \partial\theta/\partial y = 0$. Moreover, the magneto-capacitance measurement gave $\omega_0 = 90°$, which gives $\theta_0 = 90°$ from Fig. 3-3. Therefore, it was concluded that the liquid-crystal molecules are parallel to the substrate surface and directed to the liquid-crystal flow directions (parallel alignments, $\theta_0 = 90°$) for those cells with rather small x values ($x \leqq 1.2\times10^{-5}$ for 12S-treated glass substrates and $x \leqq 3.9\times10^{-7}$ for FS150-treated glass substrates). On nontreated glass substrates ($x = 0$), the liquid-crystal molecules also took parallel alignments. For intermediate values of x, no uniform alignment could be obtained. The non-uniform alignments are represented as X in Table 5-5.

ii. 5CB alignment angles

Homeotropic alignments were observed for 12S-treated glass substrates with $x \geqq 1.2\times10^{-4}$ and for FS150-treated glass substrates with $x \geqq 1.3\times10^{-5}$. In contrast with the MBBA parallel alignment, however, distorted and tilted alignments were obtained in cases of $x \leqq 5.9\times10^{-5}$ for 12S- and $x \leqq 1.3\times10^{-7}$ for FS150-treated glass substrates. Interfacial alignment angle θ_0 values for these cases were determined as follows. Realization of $\phi = 0°$ and $\partial\theta/\partial x = \partial\theta/\partial y = 0$ was confirmed

from the same microscopic observations with rotating crossed-nicols as used in MBBA cases. Thus, 5CB alignment was also concluded to be one of Fig. 3-1(a), (b) or (c). The magneto-capacitance measurements gave $\omega_0 = 54°$ as shown in Fig. 5-5(a). From Fig. 3-3, therefore, θ_0 values should be either 54° (Case (c) in Fig. 3-1) or 23° (Case (a) in Fig. 3-1). Finally, 5CB alignment was found to be the case (a) in Fig. 3-1 with $\theta_0 = \theta_{02} = 23°$ from the symmetry of the ω-dependence of capacitance C in Fig. 5-5(a) and the consideration described in Section 3-2-1.

In order to confirm the distorted alignment, the magneto-capacitance measurements for the ω-H characteristics of capacitance C described in Section 3-2-1 were performed (Fig. 5-5(b)). First, magnetic-field strength was scanned for $\omega = \pm 54°$ in the x-z plane. For both $\omega = +54°$ and $\omega = -54°$ cases, no capacitance changes were observed, when applied magnetic-field strength H was increased. These results indicate that the x-y plane is a mirror symmetric plane for the liquid-crystal alignment, as explained in Section 3-2-1. Next, H was scanned for $\omega = \pm(90°-54°)$ in the x-z plane. In these cases, the capacitance increased with H, and no critical Freedericksz transitions were observed. These results exclude a possibility of homogeneously tilted alignment with $\theta_0 = 54°$. In addition, conoscopic observations supported excluding the possibility of homogeneously tilted alignment.

From all of observations and discussions in Section 3-2-1, it seems most reasonable to assign the distorted alignment of Fig. 3-1(a). Thus, it was concluded that $\theta_0 = 23°$ for 5CB alignment at 12S-treated glass surfaces with $x \leqq 5.9\times10^{-5}$ and for FS150-treated glass surfaces with $x \leqq 1.3\times10^{-7}$. This distorted and tilted alignment with $\theta_0 = 23°$ was also observed at non-treated glass surfaces ($x = 0$). For the FS150-treated substrates with $x = 3.9\times10^{-7} \sim 3.9\times10^{-6}$, no uniform alignment could be obtained.

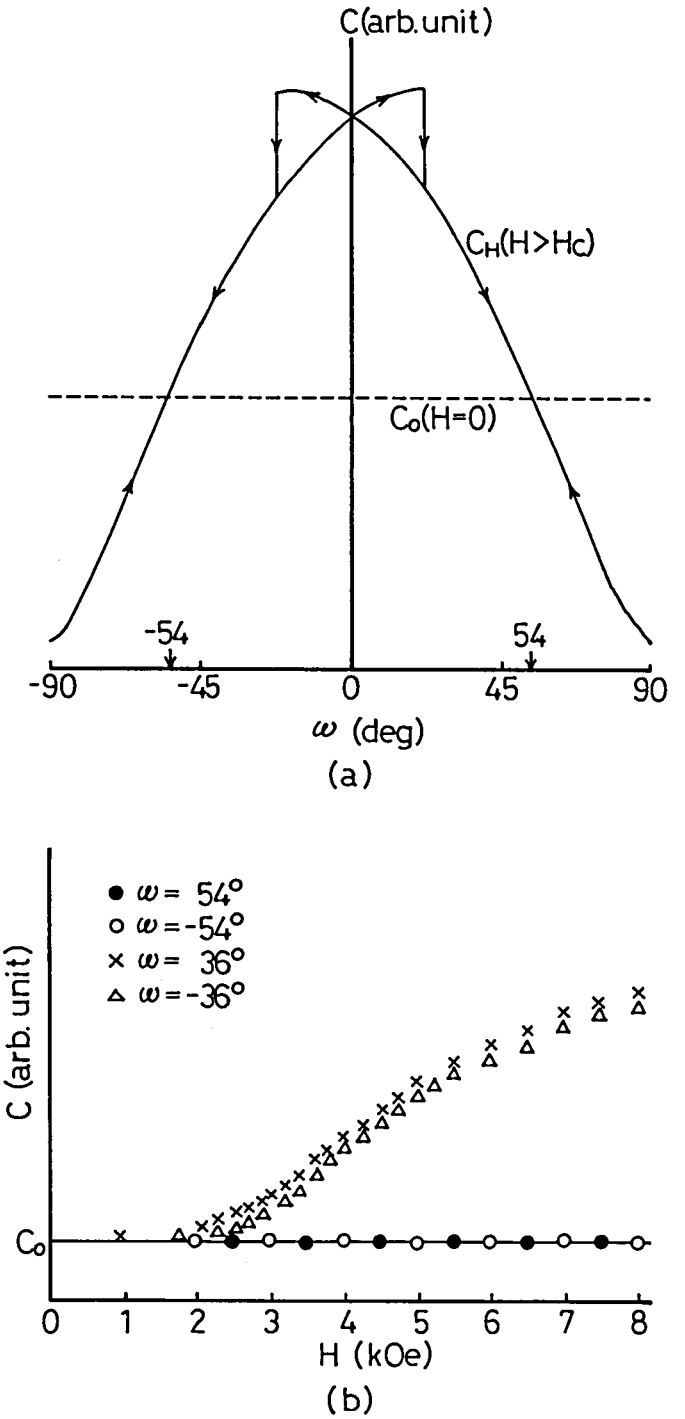

Fig. 5-5 Magneto-capacitance measurements for 5CB. (a) Measured liquid-crystal layer capacitance C versus angle ω for applied magnetic field and (b) measured liquid-crystal layer capacitance C versus applied magnetic field strength H.

5-4-2. Surfactant-material effects

Contact-angle α values were measured for the substrates as shown in Table 5-2. Measured α values are shown in Table 5-6. The substitution of these α, γ_L^d, and γ_L^p values into Eq. (5-9) and the use of the least square method, γ_S^d and γ_S^p values were derived for each substrate with the organic layer in Table 5-2. The results are listed in Table 5-7.

Table 5-7 Derived substrate surface-energy components and measured MBBA alignment angles.

	γ_S^d	γ_S^p	θ_0 (MBBA)
	(erg/cm^2)		(deg)
GLASS	32.0	33.6	90
SURFACTANTS			
6Br (C_6H_{13}-, CATION)	34.6	23.7	∿75
8Br (C_8H_{17}-, ——)	32.4	15.2	∿75
FS150 (C_8F_{17}-, ——)	7.7	22.2	0
COUPLING AGENTS			
10S ($C_{10}H_{21}$-, SILANE)	34.0	3.5	0
12S ($C_{12}H_{25}$-, ——)	33.9	3.0	0
14S ($C_{14}H_{29}$-, ——)	31.1	3.3	0
16S ($C_{16}H_{33}$-, ——)	33.2	2.4	0
18S ($C_{18}H_{37}$-, ——)	32.2	2.2	0
EDORAN($C_{17}H_{35}$-, CHROME COMPLEX)	33.1	1.1	0
FC805 (C_8F_{17}-, ——)	14.2	7.4	0
RESINS			
SR2411 (SILICONE)	16.6	0.4	0
VERSAMID940 (POLYAMIDE)	30.8	0.2	0
TORAYNEECE (POLYIMIDE)	38.9	6.5	90

Table 5-6 Measured liquid contact-angles on glass substrates with various surfactants.

		SURFACTANTS			COUPLING AGENTS							RESINS		
LIQUIDS	GLASS	6Br	8Br	FS150	10S	12S	14S	16S	18S	EDRAN	FC805	SR2411	VERSAMID 940	TORAY-NEECE
WATER	3.5	31.1	56.4	71.3	80.9	84.7	82.2	83.9	84.0	86.5	97.3	106.8	104.6	70.4
GLYCEROL	9.1	38.4	52.5	83.6	70.6	73.3	76.2	74.7	77.4	84.1	75.7	99.4	98.5	58.6
FORMAMIDE	3.5	19.9	29.5	53.4	61.1	57.4	64.2	67.2	70.3	73.2	69.1	99.5	94.7	45.5
di-IODOMETHANE	46.8	40.4	52.6	98.5	52.5	51.9	54.2	53.0	55.9	54.3	77.6	88.2	70.1	38.4
α-BROMONAPHTHALENE	10.7	9.3	25.1	88.9	30.8	35.6	40.9	34.5	34.1	32.0	90.0	67.8	27.4	17.6
n-HEXADECANE	9.6	5.6	14.8	76.3		∿0		∿0		4.1	66.2			
n-TETRADECANE	∿0	4.0	4.3	74.8						8.6	62.2	30.8	10.8	6.2
n-DODECANE		∿0	∿0	70.4						5.9	59.3	24.1	4.1	8.3
n-DECANE				67.1							47.5	15.0	5.7	6.9
n-OCTANE				60.9							26.0	∿0	∿0	∿0
n-HEXANE				44.4							7.2			

The actual MBBA alignment angles θ_0 at the substrate surfaces were measured by the magneto-capacitance method on the monitoring In_2O_3 electrodes, and confirmed by conoscopic observations on the bare glass area. The results are also summarized in Table 5-7.

The derived γ_S^d and γ_S^p values as well as MBBA alignment angles for each substrate are shown in Fig. 5-6 . In Fig. 5-6 , circles represent the MBBA homeotropic alignment ($\theta_0 = 0°$) and crosses represent the MBBA non-homeotropic alignment ($\theta_0 \neq 0°$) . Dotted lines in Fig. 5-6 , which start at the "GLASS" point and end at the "FS150" and "12S" points, connect measured γ_S^d and γ_S^p values for different concentrations x of FS150 and 12S aqueous solutions used for the substrate surface-treatments, respectively, which are obtained in Section 5-4-1. Thus, different intermolecular-forces contributions were exhibited for each MBBA homeotropic alignment.

5-5. Discussions

As is clearly seen in the measured results, in Fig. 5-6 , the liquid-crystal interfacial alignments are determined by the competition between polar and dispersive interactions at the liquid-crystal substrate interface, and either low γ_S^d or low γ_S^p substrate tends to produce MBBA homeotropic alignment. The reason why MBBA aligns homeotropically on low γ_S^d or low γ_S^p substrate is subject to Section VI . In this section, discussions are made on the origin of substrate surface-energy compositions shown in Table 5-7, which are characteristic to the surface layer materials.

The bare glass surface has rather large surface energy, $\gamma_S^d = 32.0$ erg/cm^2 and $\gamma_S^p = 33.6$ erg/cm^2 . On such a substrate surface, MBBA molecules tend to align parallel to the substrate surface. In order to make MBBA molecules align homeotropically on glass substrates, it

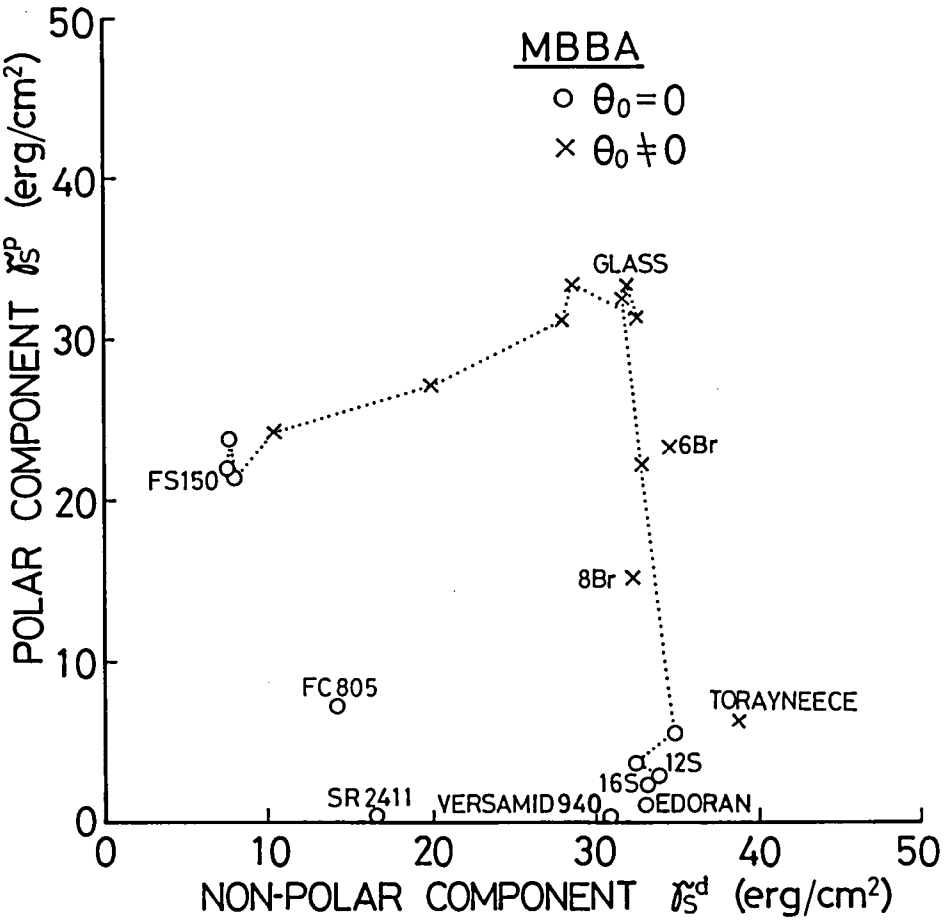

Fig. 5-6 Measured substrate surface-energy components γ_S^d and γ_S^p and MBBA alignment angles θ_0.

is necessary to reduce either polar or dispersive surface-energy components of glass substrates.

Organic layers are considered to screen the surface electrostatic-field of glass substrates and reduce their polar surface-energies. Obtained polar surface-energies are rather large for cationic surfactants (6Br, 8Br, FS150) as compared with those for coupling agents (10S, 18S, Edoran, FC805). The rather large γ_S^p values for 6Br and

8Br are considered to be caused by their ionic characteristics and comparatively short alkyl chains insufficient to screen the glass surface-potential. In addition, in the FS150 case, its polar $-SO_2NH-$ group is considered to play some roles to make γ_S^p rather large. On the other hand, the coupling-agent layers show rather small γ_S^p values, which are thought to be produced by their chemisorption characteristics in such a manner as changing polar silanol groups on glass surfaces into siloxane bondings. For both the surfactant and the coupling-agent layers, a tendency can be found wherein γ_S^p decreases as the alkyl-chain length becomes longer. This will be an evidence of the above-mentioned screening effect and explains the empirical condition that comparatively long alkyl chains are needed for surfactants to produce the liquid-crystal homeotropic alignment.

Another evidence of the screening effect can be found in the x-dependence of γ_S^p for the substrates treated with 12S aqueous solutions, which was shown in Fig. 5-3. If 12S richer solutions are used for surface treatments, 12S molecules are considered to be deposited with higher density on glass substrates. Such a 12S high-density layer will screen the glass surface-potential more effectively than a lower-density layer. This will be the reason why 12S richer solutions make the substrate polar surface-energy smaller.

In comparison with these γ_S^p reducing materials, FS150 is characterized by its small γ_S^d. This γ_S^d reducing effect is thought to be caused by the FS150 perfluorocarbon chain which is well known to exhibit a small γ_S^d value. The x-dependence of γ_S^d for substrates treated with FS150 solutions, shown in Fig. 5-4 , clearly exhibits that the FS150 layer with higher density produces smaller γ_S^d value. The small γ_S^d value caused by perfluorocarbon chains is also found for a coupling agent FC805. The γ_S^d values for surfactants and coupling agents with hydrocarbon chains are almost the same. This is characteristic of the terminal $-CH_3$ group.

The extremely small γ_S^p values obtained by the resins are considered to be the result of their rather thick layers which were formed by the spinner-coating method. The Torayneece layer shows somewhat large γ_S^p value compared with the other resins. This is considered to be characteristic of the polyimide imino group =NH.

5-6. Summary

In this section, the principle and experimental results have been described for dispersive and polar substrate surface-energy components measurements. Substrate surface-energy components, γ_S^d and γ_S^p, exhibit different compositions in accordance with the surfactant concentration in its solution used for surface treatment, and liquid-crystal interfacial alignment angle θ_0 depends on substrate surface-energy compositions.

From observations for relationships between θ_0 and substrate surface-energy components, γ_S^d and γ_S^p, of various surface-treated substrates, MBBA has been found to exhibit a tendency to align homeotropically either on low γ_S^d or low γ_S^p substrates. Low γ_S^p values are obtained by screening the surface electrostatic field of glass substrates. As for the screening effect, surfactants without polar groups and coupling agents with chemisorption ability seem effective and relatively long alkyl chains are desired. In addition, a rather thick layer of some resins is also preferable for reducing γ_S^p values. On the other hand, surfactant perfluorocarbon chains are effective to reduce substrate-surface γ_S^d values.

References

[1] F. M. Fowkes, Adv. Chem. Series, 43, 99 (1964)

[2] S. Wu, J. Adhesion, 5, 39 (1973)

[3] J. R. Dann, J. Colloid Interface Sci., 32, 302 (1970)

[4] This polarized microscopic observation gives two possibilities, $\phi = 0°$ and $90°$. However, $\phi = 0°$ is defined from another optical observation using liquid crystal doped with a preochroic dye.

VI. DERIVATION OF SUBSTRATE SURFACE-ENERGY DEPENDENCE OF EASY-AXIS ANGLE

6-1. Introduction

The relationships between liquid-crystal interfacial alignment angle θ_0 and substrate surface-energy components, γ_S^d and γ_S^p, have been experimentally exhibited in Section V. Both MBBA and 5CB homeotropic alignments ($\theta_0 = 0°$) have been shown to be realized for low γ_S^d or low γ_S^p substrates. On substrates with rather large surface energied γ_S^d and γ_S^p, MBBA aligns parallel to the substrate and 5CB exhibits tilted alignments. The interpretations for these (γ_S^d, γ_S^p)-dependence of θ_0 are left for this section.

In order to obtain the easy-axis angle Θ, for which the liquid-crystal substrate interfacial-interaction energy becomes minimum, the liquid-crystal surface energy should be represented in a surface alignment-angle dependent form. In Section 6-2, a proper formula in such a form is given for liquid-crystal surface energy γ_{LC}. By using this γ_{LC} formula, the easy-axis angle is calculated for various γ_S^d and γ_S^p values. In Section 6-3-1, calculated results are compared with the previous experimental results. Moreover, the validity of existing γ_c-hypothesis is discussed in Section 6-3-2. Section 6-4 summarizes the contents in this section.

6-2. Interfacial Interaction Energy Representation

The liquid-crystal molecular alignment has to minimize the total free energy per substrate unit-area,

$$W = W_L + W_S \ , \qquad (6\text{-}1)$$

where W_L is the free energy per unit volume and W_S is the interfacial free-energy per unit area. Here, consider the case when liquid-crystal interfacial alignment is uniform. In such a case, no director distortions exist in the liquid-crystal bulk under no external magnetic or electric field, and the equilibrium liquid-crystal alignment is determined by minimizing W_S instead of W. Moreover, by choosing the coordinates system to satisfy ϕ_0 (the director azimuthal angle) = 0°, W_S is represented as a single-variable function of θ_0, the director polar angle. In the following, therefore, interfacial-energy density $W_S(\theta_0)$ is considered instead of the total free-energy W. The interfacial-energy density W_S is represented as

$$W_S = \gamma_S + \gamma_{LC} - W_a \quad , \tag{6-2}$$

by using substrate surface-energy γ_S, liquid-crystal surface-energy γ_{LC} and work of adhesion W_a which is needed to separate the liquid-crystal bulk infinitely from the substrate surface. It is assumed that each term in Eq. (6-2) is a sum of dispersive and polar force components, whose origins are independent of each other,

$$\begin{aligned} \gamma_S &= \gamma_S^d + \gamma_S^p \quad , \\ \gamma_{LC} &= \gamma_{LC}^d + \gamma_{LC}^p \quad , \\ W_a &= W_a^d + W_a^p \quad , \end{aligned} \tag{6-3}$$

where superscripts d and p represent dispersive and polar components, respectively.

Dispersive terms in W_S According to Fowkes[1], W_a^d is given by a formula,

$$W_a^d = 2[\gamma_S^d \gamma_{LC}^d(\theta)]^{1/2} \quad . \tag{6-4}$$

Therefore, the dispersive term of $W_S(\theta)$ becomes

$$\begin{aligned} W_S^d &= \gamma_S^d + \gamma_{LC}^d(\theta) - W_a^d \\ &= [\gamma_S^{d\,1/2} - \gamma_{LC}^d(\theta)^{1/2}]^2 \quad . \end{aligned} \tag{6-5}$$

The dispersive component of liquid-crystal surface-energy γ^d_{LC} originates from the London-Van der Waals force. Parsons[2] derived a formula,

$$\gamma^d_{LC} = \gamma^d_1(S) + \gamma^d_2(S)(\vec{n}\cdot\vec{k}) \quad , \tag{6-6}$$

where S is the scalar order parameter, $\vec{n}$ is the director, and $\vec{k}$ is the surface normal. As long as we are concerned in the liquid-crystal alignment-angle dependence of the interfacial energy, it is possible to consider that $\gamma^d_1(S)$ and $\gamma^d_2(S)$ are constant. Therefore, γ^d_{LC} is represented in the form of Eq. (6-6) as

$$\gamma^d_{LC}(\theta) = \gamma^d_{L0} + \Delta\gamma^d_L \sin^2\theta \quad . \tag{6-7}$$

Polar terms in W_S According to Girifalco[3], the work of adhesion between semi-infinite volumes of i- and j-molecules is given by

$$W_{a\,ij} = (n_i n_j A_{ij} / 6d_{ij}^2)[1/2 - 1/(m-4)] \quad , \tag{6-8}$$

where n_i and n_j are molecular volume-densities, d is the equilibrium separation between the volumes of i- and j-molecules, A_{ij} is an attraction constant, and m is the repulsive exponent in the Lennard-Jones potential function. The Debye-Keesom theory gives a formulation for A_{ij} caused by the dipole$\leftrightarrow$dipole interactions,

$$A^p_{ij} = 2\mu_i^2\mu_j^2 / 3kT \quad . \tag{6-9}$$

Here, μ is the permanent-dipole moment, k is the Boltzman constant, and T is the temperature. Similarly, the work of cohesion W_c is given by

$$W_{c\,ij} = (n_i^2 A_{ii} / 6 d_{ii}^2)[1/2 - 1/(m-4)] \quad , \tag{6-10}$$

and

$$A^p_{ij} = 2\mu_i^4 / 3kT \quad . \tag{6-11}$$

By assuming

$$d_{ij} = (d_{ii}\, d_{jj})^{1/2} \quad , \tag{6-12}$$

Eqs. (6-8) ∿ (6-11) lead to

$$W^p_{a\,ij} = (W^p_{c\,ii}\, W^p_{c\,jj})^{1/2} \quad . \tag{6-13}$$

By considering

$$W^p_{c\,ii} = 2\gamma^p_i \quad , \tag{6-14}$$

we obtain

$$W^p_{a\,ij} = 2\,(\gamma^p_i \gamma^p_j)^{1/2} \tag{6-15}$$

By putting i = S and j = LC , we have

$$W^p_a = 2\,[\, \gamma^p_S \gamma^p_{LC}(\theta)\,]^{1/2} \quad . \tag{6-16}$$

Therefore, the polar term of $W_S(\theta)$ becomes

$$\begin{aligned} W^p_S(\theta) &= \gamma^p_S + \gamma^p_{LC}(\theta) - W^p_a \\ &= [\, \gamma^{p\ 1/2}_S - \gamma^p_{LC}(\theta)^{1/2}\,]^2 \quad . \end{aligned} \tag{6-17}$$

The origins of polar forces are dipole↔dipole interactions between permanent-charge distributions, dipole↔induced-depole interactions between a permanent-charge distribution and an induced moment, and bonding interactions, such as hydrogen bonding. The hydrogen bonding, however, is considered to be the electrostatic interaction between pertinent groups, such as OH and NH. Since it is generally accepted that the dipole↔dipole interaction is predominant for ordinary polar liquids, it is plausible to assume the dipole↔dipole interaction is the dominant term in γ^p_{LC}. Parsons[4] derived that $\gamma^p_{LC}(\theta)$ becomes minimum for $(\vec{n}\cdot\vec{k}) = 0$, when the permanent dipole is parallel to the molecular axis. By taking this result into consideration, it is possible to represent $\gamma^p_{LC}(\theta)$ in a similar form to Eq. (6-7) for $\gamma^d_{LC}(\theta)$. At the interface, however, breakdown occurs in liquid-crystal molecular antiparallelism, which yields a linear term for $(\vec{n}\cdot\vec{k})$ in the $\gamma^p_{LC}(\theta)$ formula. In the bulk, the average S

of quadrupole moment in the director direction is used as the liquid-crystal order-parameter, while the average P of dipole moment in the director direction becomes zero. On the contrary, the order parameter P should be taken into consideration for the dipole $\leftrightarrow$ dipole interaction at the interface, because P order exists ($P \neq 0$) close to the interface. Therefore, a pertinent formula is,

$$\gamma_{LC}^{p} = \gamma_{1}^{p}(S) + \gamma_{2}^{p}(S)\,(\vec{n}\cdot\vec{k})^{2} + \gamma_{3}^{p}(P)\,(\vec{n}\cdot\vec{k}) \quad . \qquad (6\text{-}18)$$

For further calculations, it is convenient to represent γ_{LC}^{p} as a function of θ in the form of

$$\gamma_{LC}^{p}(\theta) = \gamma_{L0}^{p} + \Delta\gamma_{L}^{p} \sin^{2}(\theta - \Theta_{p}) \quad . \qquad (6\text{-}19)$$

Here, Θ_{p} was introduced to represent the contribution of $\gamma_{3}^{p}(P)$ in Eq. (6-18) .

By adding $W_{S}^{d}(\theta)$ and $W_{S}^{p}(\theta)$, we have

$$W_{S}(\theta) = [\,\gamma_{S}^{d\,1/2} - \gamma_{LC}^{d}(\theta)^{\,1/2}\,]^{2} + [\,\gamma_{S}^{p\,1/2} - \gamma_{LC}^{p}(\theta)^{\,1/2}\,]^{2} \quad , \qquad (6\text{-}20)$$

where $\gamma_{LC}^{d}(\theta) = \gamma_{L0}^{d} + \Delta\gamma_{L}^{d} \sin^{2}\theta$ and $\gamma_{LC}^{p}(\theta) = \gamma_{L0}^{p} + \Delta\gamma_{L}^{p} \sin^{2}(\theta - \Theta_{p})$.

For given values of substrate surface energies, γ_{S}^{d} and γ_{S}^{p} , and liquid-crystal characteristic parameters, γ_{L0}^{d} , $\Delta\gamma_{L}^{d}$, γ_{L0}^{p} , $\Delta\gamma_{L}^{p}$, and Θ_{p} , it is possible to obtain the θ value which minimizes $W_{S}(\theta)$ in Eq. (6-20) , that is the easy-axis angle Θ at the interface. Practical Θ calculations for each γ_{S}^{d} and γ_{S}^{p} corresponding to the previous experimental conditions are performed and are compared with experimental results in the following section.

6-3. Calculations for Easy-Axis Angles

As no precise values for the liquid-crystal surface-energy para-

meters are available, reported values, which were measured or estimated as those at free surfaces, were used for γ_{L0}^d, $\Delta\gamma_L^d$, γ_{L0}^p, and $\Delta\gamma_L^p$. The other parameter Θ_p was estimated from reported molecular-alignment measurements at the free surface of the liquid-crystal layer. For MBBA, Θ_p is evaluated to be $0°$, so that MBBA free-surface energy $\gamma_{LC}(\theta_0) = \gamma_{LC}^d(\theta_0) + \gamma_{LC}^p(\theta_0)$ becomes minimum for $\theta_0 = 0°$. Thus, the present model, Eqs. (6-7) and (6-19), predicts the observed MBBA homeotropic-alignment tendency at the free surface[5]. For 5CB, Θ_p is evaluated to be around $90°$. Although the choice $\Theta_p = 0°$ for MBBA and $\Theta_p = 90°$ for 5CB is an assumption, it explains the difference between MBBA and 5CB permanent-dipole directions, which are almost perpendicular for MBBA and parallel for 5CB to the molecular longitudinal axis (see Fig. 5-2), and leads to reasonable results as presented in the following sections.

6-3-1. Comparison with experimental results

The following subsections present results of calculations on MBBA and 5CB preferred alignments on substrates with various γ_S^d and γ_S^p values, using Eq. (6-20) and estimated γ_{L0}^d, $\Delta\gamma_L^d$, γ_{L0}^p, $\Delta\gamma_L^p$, and Θ_p values.

i. MBBA

For MBBA, dispersive and polar components of the surface energy are reported as $\gamma_{LC}^d = 29.0$ erg/cm^2 and $\gamma_{LC}^p = 9.0$ erg/cm^2[6]. In addition, MBBA surface energy anisotropy is estimated to be 4.5×10^{-2} erg/cm^2 (see Appendix B). By taking these results into consideration, MBBA characteristic parameters were estimated as $(\gamma_{L0}^d, \Delta\gamma_L^d, \gamma_{L0}^p, \Delta\gamma_L^p, \Theta_p) = (29.0, 4.5\times10^{-2}, 9.0, 4.5\times10^{-2}, 0°)$. By using these material constants and Eq. (6-20), a relationship between Θ and γ_S^p for $\gamma_S^d = 32.0$ erg/cm^2 was obtained and is shown in Fig. 6-1. In Fig. 6-1, another computation result is also shown in the case of $\Delta\gamma_L^d = \Delta\gamma_L^p = 1.0$ erg/cm^2 which is a rather large value used in pertinent literature[4].

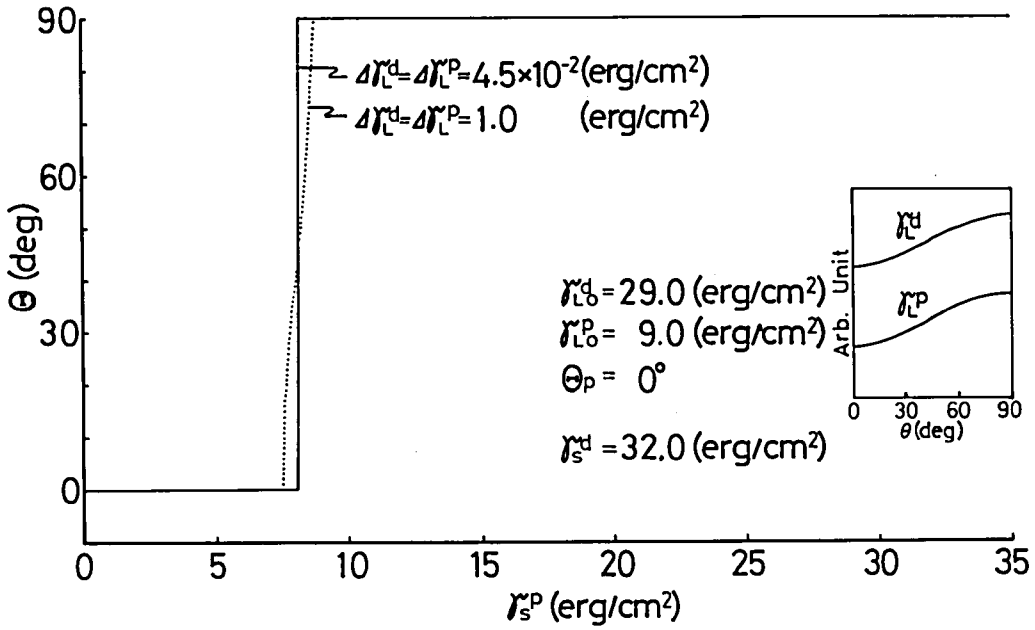

Fig. 6-1 Calculated relations between easy-axis angle Θ and polar component of substrate surface-energy γ_S^p (MBBA, $\gamma_S^d = 32.0$ erg/cm^2).

As is shown in Fig. 6-1, $\Delta\gamma_L^d$ and $\Delta\gamma_L^p$ values do not so much affect the upper limit of γ_S^p value, which is needed to realize $\Theta = 0°$ (homeotropic alignment) for constant γ_S^d. Figure 6-1 shows that, in the case of $\gamma_S^d = 32.0$ erg/cm^2, it is necessary that $\gamma_S^p < \sim 7$ erg/cm^2 for $\Theta = 0°$. This is in fairly good agreement with experimental results in Fig. 5-3, which show that the MBBA homeotropic alignment is obtained where $\gamma_S^p = 3 \sim 6$ erg/cm^2 and $\gamma_S^d = 32.5 \sim 35$ erg/cm^2.

The relationships between Θ and γ_S^p for several γ_S^d values were calculated, as shown in Fig. 6-2. Figure 6-2 shows that the upper limit of γ_S^p value for producing MBBA homeotropic alignment depends on γ_S^d value. A region of γ_S^d and γ_S^p, where $\Theta = 0°$ is obtained as an energetically stable alignment, is shown in Fig. 6-3. In Fig. 6-3, the upper region corresponds to $\Theta > 0°$ and, in almost all the upper region except very close to the boundary, $\Theta = 90°$ is obtained as an energeti-

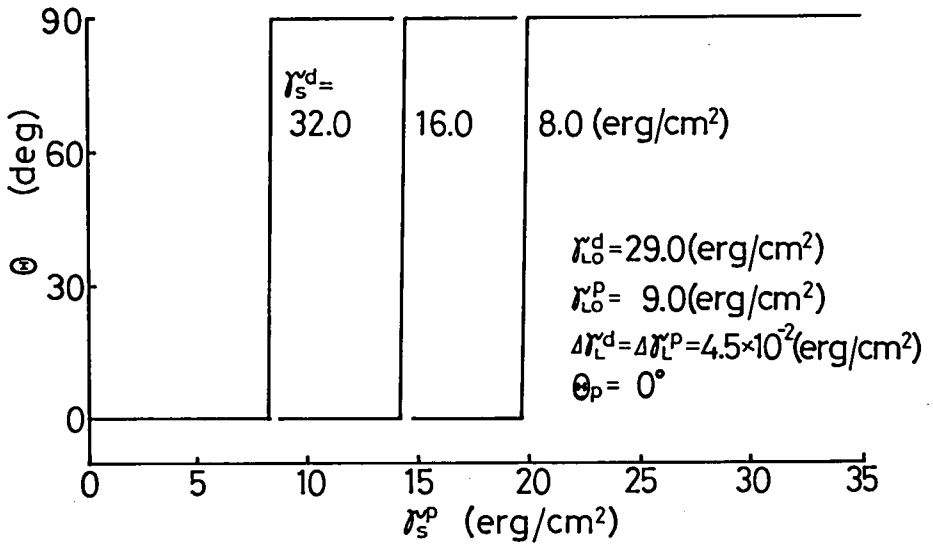

Fig. 6-2 Calculated relations between MBBA easy-axis angle Θ and substrate surface-energy γ_S^p (γ_S^d = 8.0, 16.0, 32.0 erg/cm^2) .

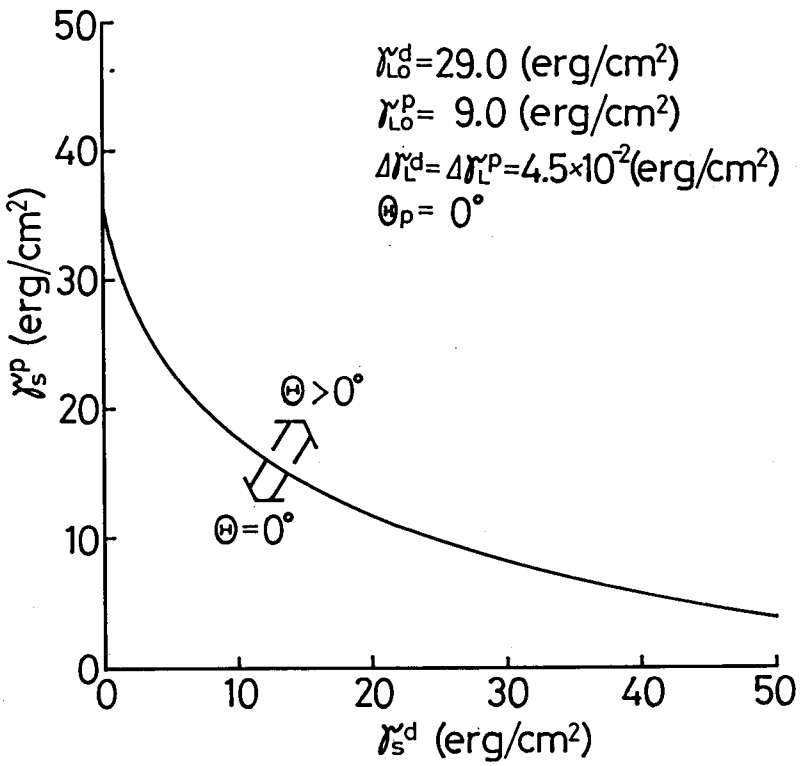

Fig. 6-3 Calculated substrate surface-energy condition for MBBA homeotropic alignment (Θ = 0°) .

cally stable alignment. The region where Θ has an intermediate value between 0° and 90°, increases as $\Delta\gamma_L$ increases.

The calculated diagram, Fig. 6-3, was overlapped on the experimental results in Fig. 5-6, as in Fig. 6-4. Figure 6-4 shows that the present considerations in Section 6-2 explain the observed (γ_S^d, γ_S^p)-dependence of Θ for MBBA very well.

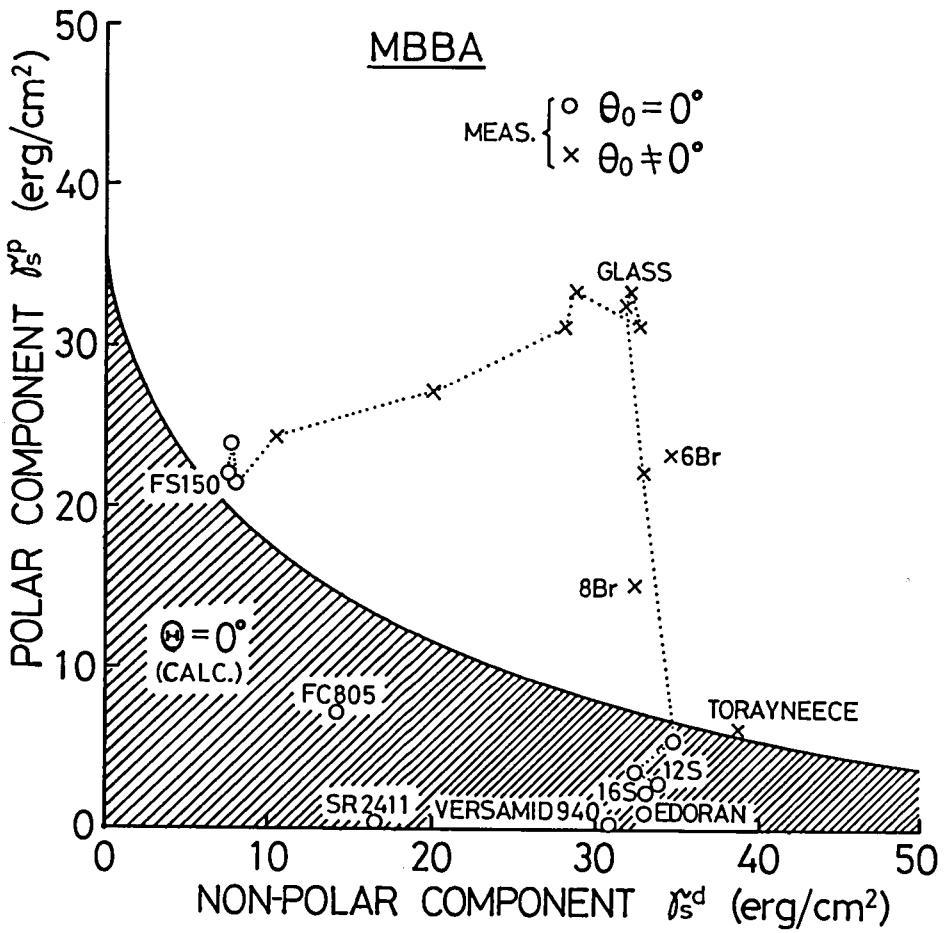

Fig. 6-4 Measured substrate surface-energy components γ_S^d and γ_S^p and MBBA alignment angles θ_0.

ii. 5CB

For 5CB, $\gamma_L^d = 40.5$ erg/cm^2 [6], $\gamma_L^p = 0$ [6], and $\Delta\gamma_L = 5\times10^{-3}$ erg/cm^2 [7] are reported. Calculations were performed by using these 5CB material constants as γ_{L0}^d and γ_{L0}^p, but $\Delta\gamma_L^d = \Delta\gamma_L^p = 1.0$ erg/cm^2 and $\theta_p = 90°$. These rather large $\Delta\gamma_L^d$ and $\Delta\gamma_L^p$ values were adopted to illustrate a gradual θ change from 90° to 0° in the θ vs γ_S^p curve. As is shown in Fig. 6-1, the increase in $\Delta\gamma_L^d$ and $\Delta\gamma_L^p$ makes the θ transition gradient in the θ vs γ_S^p curve small, but does not exert such great influence upon qualitative considerations of a critical γ_S^p value for the θ transition.

Calculated relationships between θ and γ_S^p for the cases of $\gamma_S^d = 32.0$ erg/cm^2 and $\gamma_S^d = 7.8$ erg/cm^2 are shown in Fig. 6-5, representing that $\theta = 0°$ is obtained for almost all γ_S^p values. These results explain the observed 5CB homeotropic alignment in the case of $\gamma_S^d = 32 \sim 35$ erg/cm^2 and $\gamma_S^p = 2 \sim 5$ erg/cm^2 for 12S-treated glass substrates (Fig. 5-3) and $\gamma_S^d = 7 \sim 10$ erg/cm^2 and $\gamma_S^p = 22 \sim 25$ erg/cm^2 for FS150-treated glass substrates (Fig. 5-4). However, these calculated relationships (Fig. 6-5) cannot explain the observed tilted alignment with $\theta_0 = 23°$ for the $\gamma_S^d = 32$ erg/cm^2 and $\gamma_S^p = 22 \sim 34$ erg/cm^2 cases (Figs. 5-3 and 5-4). In order to illustrate that non-zero θ can exist for $\gamma_S^d = 32$ erg/cm^2 and rather large γ_S^p conditions, some other calculations were performed, using different θ_p values. For example, the calculated result for $\theta_p = 113°$, keeping the other constants the same as before, is shown in Fig. 6-6. As is shown in Fig. 6-6, a non-zero θ region exists for larger γ_S^p values than those which produce $\theta = 0°$.

Under a boundary condition of $0° < \theta < 90°$ and the mirror symmetry condition of liquid-crystal alignment with respect to the x-y plane, a flow-induced almost parallel alignment (Fig. 6-7(a)) will be reduced into a distorted and tilted alignment with the interfacial alignment angle θ_0 between θ and 90° (Fig. 6-7(b)) as a result of the

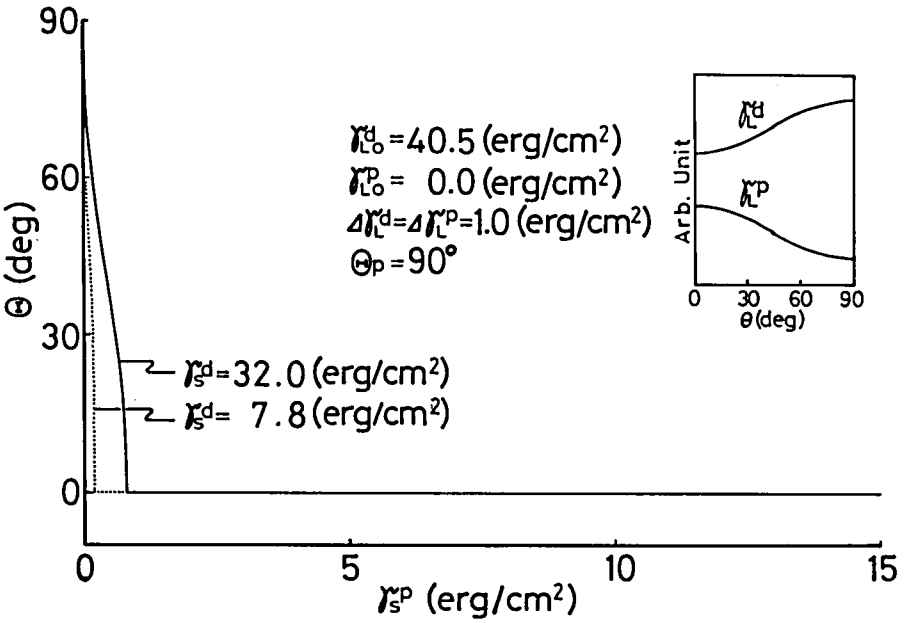

Fig. 6-5 Calculated relations between easy-axis angle Θ and polar component of substrate surface-energy γ_S^p (5CB, $\Theta_p = 90°$, $\gamma_S^d = 7.8$, 32.0 erg/cm^2).

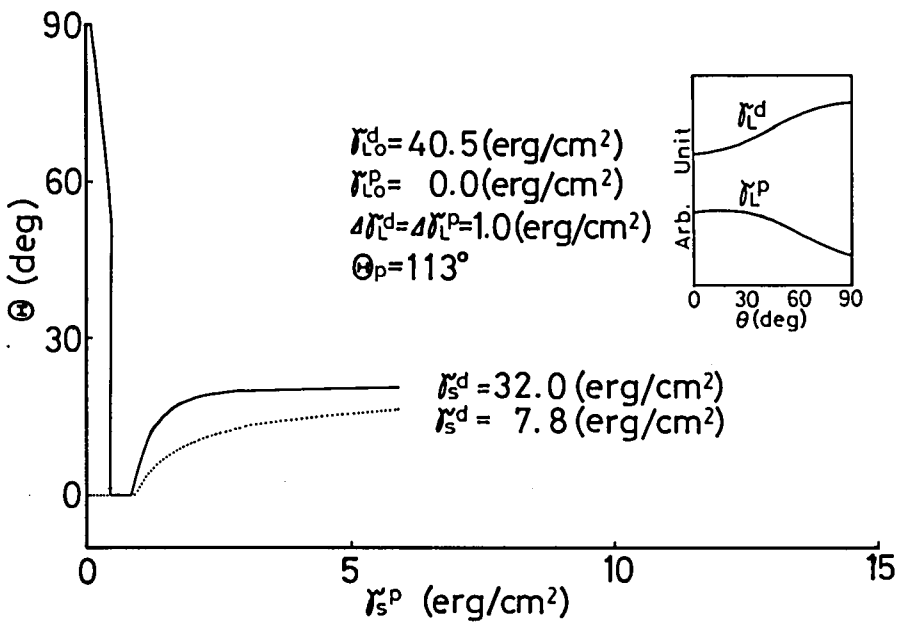

Fig. 6-6 Calculated relations between easy-axis angle Θ and polar component of substrate surface-energy γ_S^p (5CB, $\Theta_p = 113°$, $\gamma_S^d = 7.8$, 32.0 erg/cm^2)

competition between bulk distortion energy, which prefers $\theta_0 = 90°$, and interfacial interaction energy, which prefers $\theta_0 = \Theta < 90°$. If the mirror symmetry condition is removed, a uniformly tilted alignment will exist with $\theta_0 = \Theta$ (Fig. 6-7(c)) as an energetically stable alignment. However, because of relatively weak anchoring strength to restrict the liquid-crystal molecular azimuthal angle at a substrate surface[8], the liquid-crystal molecular flow will easily produce the mirror symmetric alignment condition with respect to the x-y plane. Therefore, when the liquid-crystal molecules are at rest, their alignment will finally be reduced into the distorted configuration (Fig. 6-7(b)), as observed for 5CB on the substrates with rather large γ_S^p components ($\gamma_S^p = 22 \sim 34$ erg/cm^2 for $\gamma_S^d = 32$ erg/cm^2). That is, the present model can illustrate the possible distorted alignment, although the calculated critical γ_S^p value for dividing $\Theta = 0°$ and non-zero Θ conditions is smaller than the measured value. In the 5CB case, the γ_{L0}^p deviation at the real interface from γ_L^p at the free surface, which is used as γ_{L0}^p in the present calculations, is assumed to be rather large because of a breakdown in dipole antiparallelism[6,9]. That is, the real γ_{L0}^p is considered not to be zero. It was calculated that the critical γ_S^p for non-zero Θ increases as γ_{L0}^p increases. Supported by these facts, precise determination of 5CB material constants is expected to give quantitative agreements of the present calculated results and observations for 5CB alignments.

As a result, the present considerations give qualitative explanation of the liquid-crystal alignment observations, especially concerning the liquid-crystal material (MBBA and 5CB) dependence, which was experimentally exhibited in Section 5-4-1, and substrate surface energy γ_S^d and γ_S^p dependence, which was observed in detail for MBBA in Section 5-4.

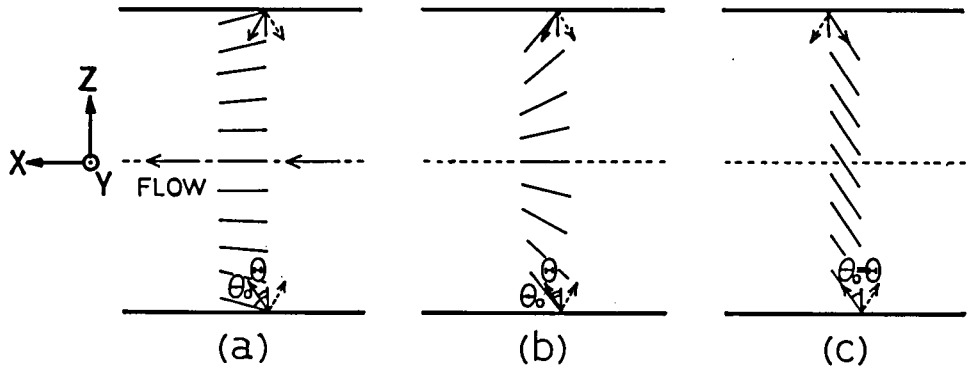

Fig. 6-7 Liquid-crystal molecular alignment models. (a) Flow alignment under weak-anchoring condition to restrict liquid-crystal molecular azimuthal angle ϕ, (b) reduced alignment with flow-induced mirror-symmetric alignment condition with respect to the x-y plane, and (c) uniformly tilted alignment when mirror-symmetric alignment condition with respect to the x-y plane is not produced.

6-3-2. Interpretation to the γ_c-hypothesis

In order to find the correlations with interfacial alignment angles θ_0, critical surface tensions γ_c for various substrates were measured. Measurements were performed on glass substrates treated with 16S ($x = 1.0\times10^{-3}$) and FS150 ($x = 3.9\times10^{-4}$). In order to determine γ_c, α values were measured for each substrate by using liquids I~XI in Table 5-1, and are listed in Table 6-1. The cosine function $\cos\alpha$ values were plotted as a function of γ_L, as in Fig. 6-8. The critical surface-tension γ_c is defined by the intercept of the line $\cos\alpha = 1$ with the extrapolated straight line of $\cos\alpha$ vs γ_L plot[10]. Values were found to be $\gamma_c(16S) = 34$ erg/cm^2 and $\gamma_c(FS150) = 11$ erg/cm^2. In addition, γ_S^d values for these substrates were found to be $\gamma_S^d(16S) = 33.2 \pm 2.1$ erg/cm^2 and $\gamma_S^d(FS150) = 9.7 \pm 2.0$ erg/cm^2 by using measured α (Table 6-1) and the method described in Section 5-2. According to Fig. 6-8, it is found that γ_c is approximately equal to γ_S^d component

Table 6-1 Measured liquid contact-angles on 16S- and FS150-treated glass substrates.

LIQUIDS	CONTACT ANGLES α (deg)	
	16S ($x=1.0\times10^{-3}$)	FS150 ($x=3.9\times10^{-4}$)
WATER	83.9 ± 3.3	71.3 ± 1.5
GLYCEROL	74.7 ± 3.9	83.6 ± 4.4
FORMAMIDE	67.2 ± 3.0	53.4 ± 3.0
di-IODOMETHANE	53.0 ± 1.8	98.5 ± 5.0
α-BROMONAPHTHALENE	34.5 ± 9.3	88.9 ± 3.7
n-HEXADECANE	0	76.3
n-TETRADECANE	0	74.8
n-DODECANE	0	70.4
n-DECANE	0	67.1
n-OCTANE	0	60.9
n-HEXANE	0	44.4

for the substrate surface energies. Therefore, it can be considered that the γ_c-hypothesis, which says that a homeotropic alignment is obtained in the case of $\gamma_c < \gamma_{LC}(\theta_0)$, is valid, only when the interfacial energy polar component can be neglected. Actually, this is clearly shown in Fig. 6-9 , as explained in the following. Equation (6-20) shows that there is no polar interfacial energy contribution if $\gamma_S^p = \gamma_{LC}^p(\theta_0)$ or $\gamma_S^p = \gamma_{L0}^p$ in the case of $\Delta\gamma_L^p \ll \gamma_{L0}^p$, which is valid for MBBA. For the MBBA case, therefore, $\gamma_S^p = 9.0$ erg/cm^2 ($=\gamma_{L0}^p$) condition corresponds to the no polar component case. In Fig. 6-9 , $\Theta = 0°$ is obtained in a region of $\gamma_S^d \leq 29.0$ erg/cm^2 for $\gamma_S^p = 9.0$ erg/cm^2. This critical γ_S^d value (29.0 erg/cm^2) is equal to the MBBA γ_{L0}^d value, which is nearly equal to $\gamma_{LC}^d(\theta_0)$ under the $\Delta\gamma_L^d \ll \gamma_{L0}^d$ condition. In addition, as mentioned above, γ_S^d is nearly equal to γ_c . Thus,

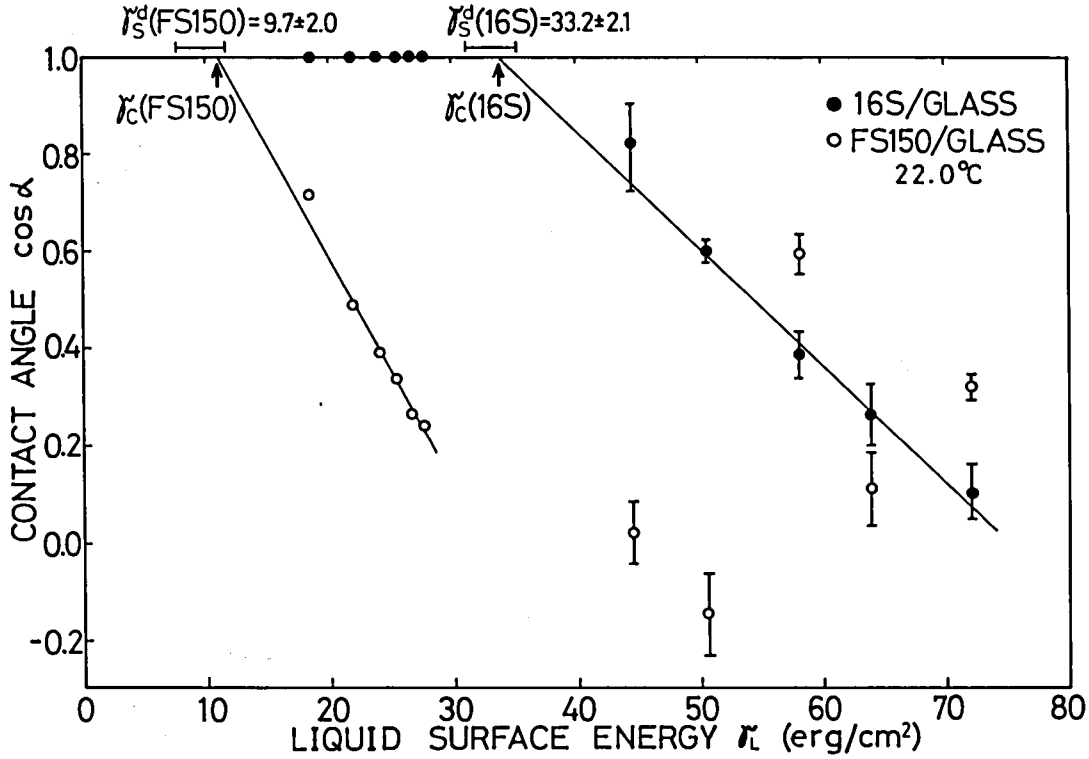

Fig. 6-8 Measured contact-angle cosine ($\cos\alpha$) versus liquid surface-energy γ_L for critical surface-tension γ_c determination.

$\gamma_S^d \leqq 29.0$ erg/cm² condition for MBBA homeotropic alignment in the no polar component case is the same as $\gamma_c \leqq \gamma_{LC}^d(\theta_0)$, which means that the γ_c-hypothesis is valid when there exist no polar interfacial energy components. Figure 6-9 also shows that, in the case of $\gamma_S^p > \gamma_{LC}^p \simeq 9.0$ erg/cm² , the upper limit of γ_S^d values for $\Theta = 0°$ (part A of the curve in Fig. 6-9) is less than γ_{L0}^d value (29.0 erg/cm²). That is, even if γ_c ($\simeq \gamma_S^d$) $< \gamma_{LC}^d$ ($\simeq \gamma_{L0}^d = 29.0$ erg/cm²), MBBA homeotropic alignment cannot always be obtained when the interfacial energy has some polar components (region B in Fig. 6-9) .

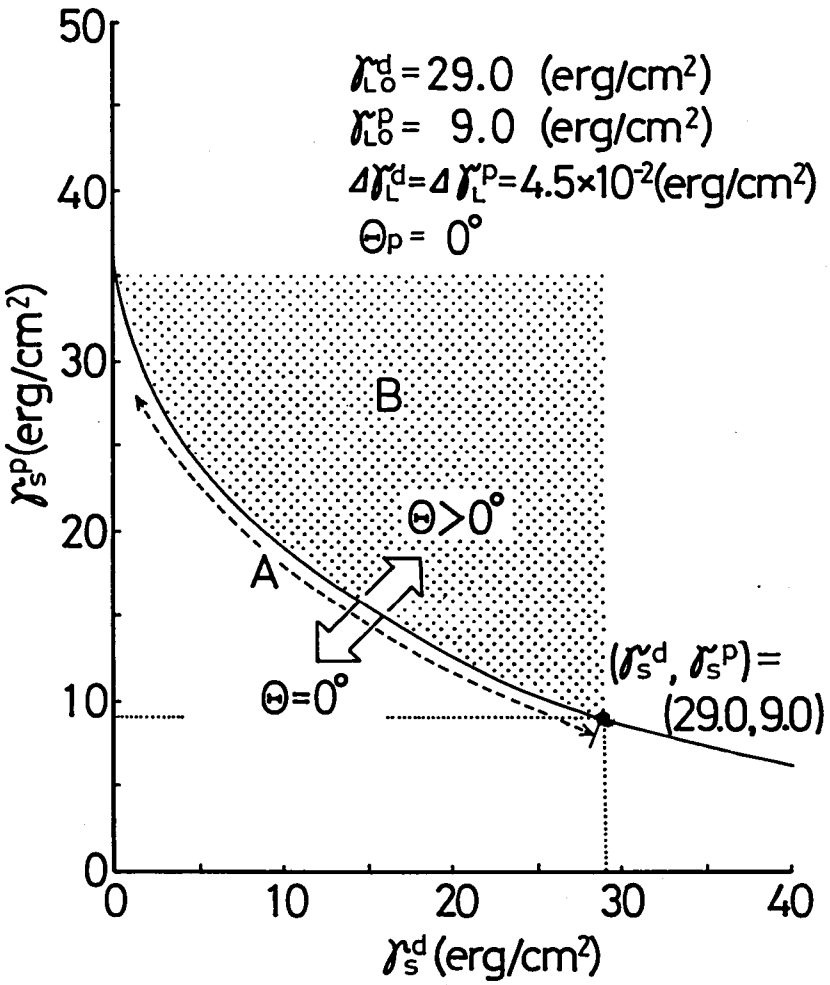

Fig. 6-9 Calculated substrate surface-energy condition for MBBA homeotropic alignment (Θ = 0°).

6-4. Summary

Liquid-crystal substrate interfacial energy has been considered as a sum of dispersive and polar components, each of which has been represented in liquid-crystal alignment-angle dependent forms. By using this interfacial energy formula and estimated characteristic parameter values for liquid-crystal surface energy components, we have calculated the easy-axis angles, so as to minimize the energy

at interfaces between liquid-crystals (MBBA and 5CB) and various substrates. The calculated results explain well the observed relations between liquid-crystal alignment angles θ_0 and substrate surface-energy components γ_S^d and γ_S^p. The calculated and observed relations between alignment angle θ_0 and surface energies γ_S^d and γ_S^p are as follows:

1) although both MBBA and 5CB align homeotropically on low γ_S^d or low γ_S^p substrates, they exhibit different alignments on high γ_S^d and high γ_S^p substrates caused by their different ways of polar interfacial interaction contributions, and

2) a γ_S^d and γ_S^p region for MBBA homeotropic alignment has been derived showing that MBBA aligns homeotropically on either low γ_S^d or low γ_S^p substrates.

In addition, by the aid of experimental results wherein critical surface-tension γ_c is approximately equal to dispersive surface-energy component γ_S^d, the existing γ_c-hypothesis for relations between liquid-crystal alignment angle and substrate surface-energy has been shown to be valid, only when no polar interfacial interaction contributions exist.

References

[1] F. M. Fowkes, Adv. Chem. Series, 43, 99 (1964)

[2] J. D. Parsons, Mol. Cryst. Liq. Cryst., 31, 79 (1975)

[3] L. A. Girifalco and R. J. Good, J. Phys. Chem., 61, 904 (1957)

[4] J. D. Parsons, J. Phys. (Paris), 37, 1187 (1976)

[5] M. A. Bouchiat and D. Langevin, Phys. Lett., 34A, 331 (1971)

[6] E. Perez, J. E. Proust, and L. Ter-Minassian-Saraga, *Adhesion 2* (Applied Science Publishers Ltd., England, 1978), Chap. 2, pp. 23 - 34

[7] J. E. Proust, E. Perez, and L. Ter-Minassian-Saraga, Colloid and Polymer Sci., 254, 672 (1976)

[8] G. Porte, J. Phys. (Paris), 37, 1245 (1976)

[9] A. G. Petrov and A. Derzhanski, Mol. Cryst. Liq. Cryst., 41, 41 (1977)

[10] W. A. Zisman, Adv. Chem. Series, 43, 1 (1964)

VII. DERIVATION OF SUBSTRATE SURFACE-ENERGY DEPENDENCE OF ANCHORING-STRENGTH COEFFICIENT

7-1. Introduction

The model described in Section VI also enables estimating the other anchoring parameter, i.e., the anchoring-strength coefficient B_θ at an interface between a substrate with known surface-energy components, γ_S^d and γ_S^p, and a liquid crystal with known surface-energy parameters, γ_{L0}^d, $\Delta\gamma_L^d$, γ_{L0}^p, $\Delta\gamma_L^p$, and θ_p.

Calculations performed for MBBA are given in Section 7-2. In Section 7-3, the calculated results are compared with previously obtained experimental results. Section 7-4 provides discussions on MBBA anchoring strength. A summary is presented in Section 7-5.

7-2. Calculations for Anchoring-Strength Coefficients

Anchoring strength at the interface, B_θ, is defined as an anisotropy coefficient in the model formula for the interfacial interaction energy (see Eq. (2-5)),

$$W_S(\theta_0) = A/2 + (B_\theta/2)\sin^2(\theta_0 - \theta) \quad . \tag{7-1}$$

In the case of $\theta = 0°$, B_θ is represented as

$$B_\theta = 2\,[\,W_S(\pi/2) - W_S(0)\,] \quad . \tag{7-2}$$

Equation (7-2), together with Eq. (6-20), enables calculating B_θ for given values of the parameters for liquid crystal, γ_{L0}^d, $\Delta\gamma_L^d$, γ_{L0}^p, $\Delta\gamma_L^p$, and θ_p, and of the parameters for substrate, γ_S^d and γ_S^p.

Calculations were performed for MBBA by using the same characteristic-parameter values (γ_{L0}^d, $\Delta\gamma_L^d$, γ_{L0}^p, $\Delta\gamma_L^p$, θ_p) = (29.0, 4.5×10^{-2},

9.0, 4.5×10^{-2}, 0°) as in Section 6-3-1. The results are shown in Fig. 7-1 . According to Fig. 7-1 , stronger anchoring conditions are expected for MBBA on substrates with small surface-energy components.

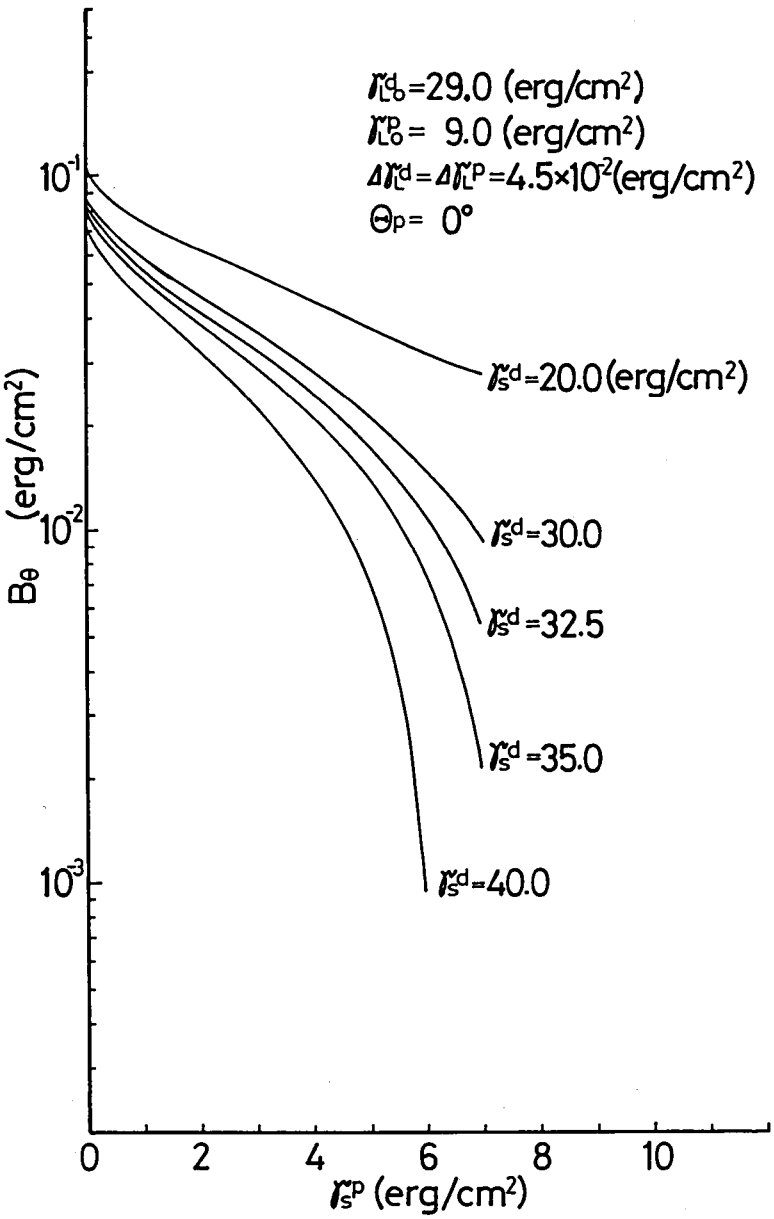

Fig. 7-1 Calculated relations between anchoring-strength coefficients B_θ and substrate surface-energy components, γ_S^d and γ_S^p.

7-3. Comparison with Experimental Results

As was described in Section 7-2, B_θ for MBBA can be calculated from measured γ_S^d and γ_S^p values and Eqs. (7-2) and (6-20). In order to calculate B_θ values and compare them with measured B_θ in Section 4-4-1, the γ_S^d and γ_S^p values were derived for the surfaces of In_2O_3 - evaporated glass substrates covered with silane coupling agent nS layers ($n = 10,12,14,16,18$, $x = 1.0\times10^{-3}$) . Contact-angle values were measured for liquids I∿V in Table 5-1 on these substrates. The results are listed in Table 7-1. The γ_S^d and γ_S^p were obtained as shown in Table 7-2 and Fig. 7-2 , by using the α values, the γ_L^d and γ_L^p values in Table 5-1, and Eq. (5-9) . The B_θ values for MBBA were calculated by using the γ_S^d and γ_S^p values and are also listed in Table 7-2 as well as the previously measured B_θ values. Both the calculated and the measured B_θ values are shown in Fig. 7-3 . It is seen in Fig. 7-3 that the calculated B_θ's agree with the measured B_θ's within an order of magnitude.

Table 7-1 Measured liquid contact-angles on nS-treated substrates (In_2O_3 - evaporated glass substrates, $x = 1.0\times10^{-3}$ mol/l).

	CONTACT ANGLES α (deg)				
LIQUIDS	10S	12S	14S	16S	18S
WATER	85.1 ± 4.4	80.2 ± 4.0	85.3 ± 5.3	85.7 ± 4.4	90.4 ± 2.0
GLYCEROL	73.3 ± 3.7	71.9 ± 1.2	73.1 ± 1.9	76.7 ± 5.5	81.8 ± 4.2
FORMAMIDE	61.0 ± 2.3	56.6 ± 1.3	61.6 ± 4.9	61.0 ± 4.1	71.6 ± 4.4
di-IODOMETHANE	55.9 ± 1.7	51.8 ± 0.6	53.0 ± 0.6	55.1 ± 0.3	56.0 ± 2.3
α-BROMONAPHTHALENE	43.1 ± 0.2	35.2 ± 6.0	33.9 ± 9.6	39.2 ± 2.4	45.8 ± 9.8

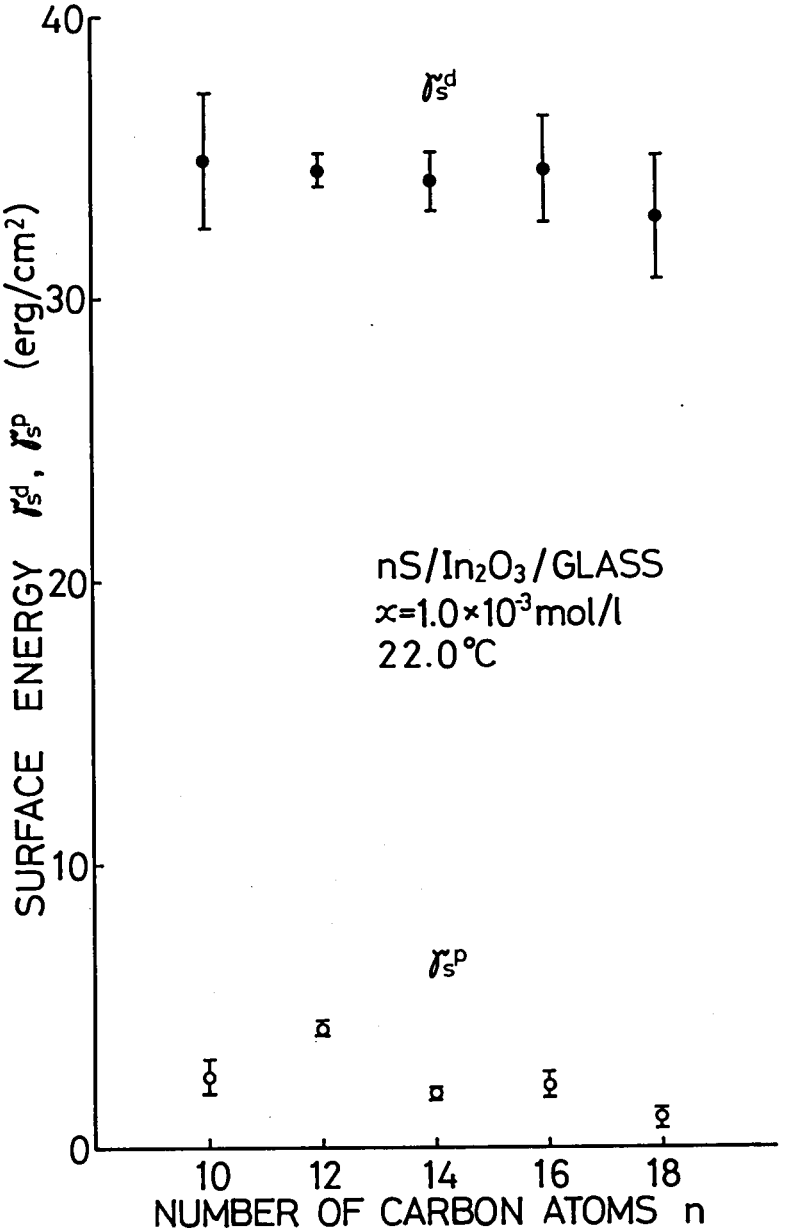

Fig. 7-2 Measured substrate surface-energy γ_S^d and γ_S^p versus number of carbon atoms n in surfactant nS alkyl chain.

Table 7-2 Derived substrate surface-energy components and calculated and measured anchoring-strength coefficients for MBBA.

	γ_S^d	γ_S^p	B_θ ($\times 10^{-2}$ erg/cm^2)	
	(erg/cm^2)		CALCULATED	MEASURED
10S	34.9 ± 2.4	2.5 ± 0.6	3.4 ± 1.0	1.6 ± 0.2
12S	34.6 ± 0.6	4.2 ± 0.2	2.0 ± 0.2	2.1 ± 0.9
14S	34.2 ± 1.1	1.9 ± 0.2	4.1 ± 0.4	3.2 ± 0.8
16S	34.6 ± 1.9	2.2 ± 0.5	3.7 ± 0.7	3.6 ± 0.7
18S	32.9 ± 2.2	1.1 ± 0.4	5.4 ± 0.9	1.2 ± 0.6

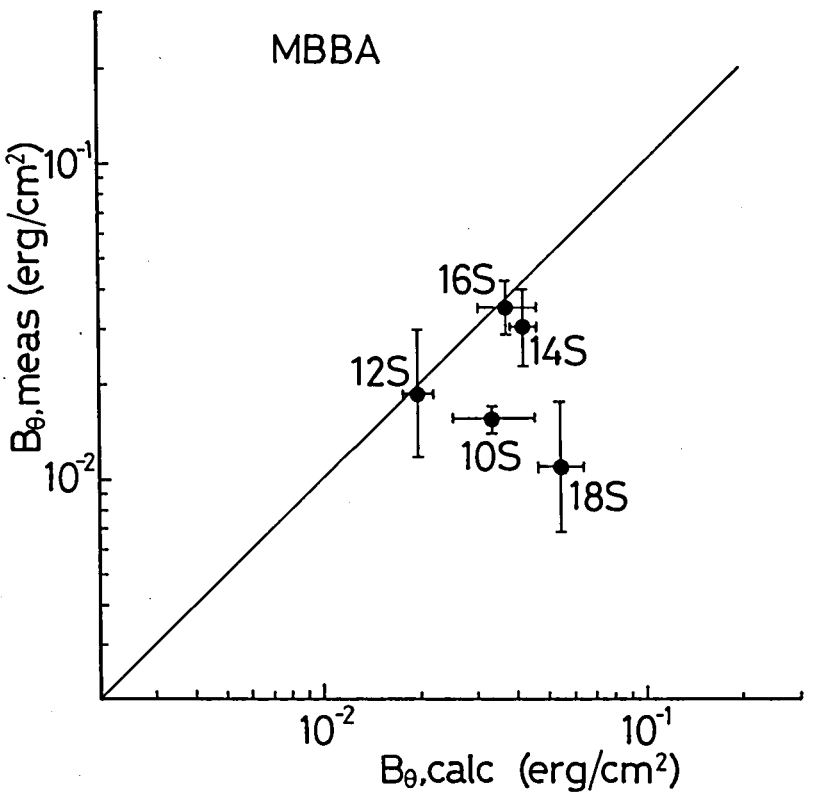

Fig. 7-3 Relations between calculated and measured anchoring-strength coefficients B_θ for MBBA on substrates with nS layers.

7-4. Discussions

Calculated results in Section 7-2 show that stronger anchoring conditions for MBBA are expected for lower γ_S^d and lower γ_S^p substrates. It has been shown in Section V that low γ_S^d is obtained by substrates covered with a perfluorocarbon-chain containing surfactants such as FS150. Thus, FS150-treated substrates are expected to exhibit strong anchoring-strength for MBBA. It has been experimentally observed in Section 4-4-1 (see Table 4-2). Moreover, the experimental results in Section V show that low γ_S^p is obtained by the surfactant-layer screening effect. Short alkyl-chain containing surfactants are considered to be less effective to screen the substrate electrostatic field and to reduce γ_S^p than long alkyl-chain containing surfactants. When the surfactant alkyl chain aligns perpendicular to a substrate surface, the substrate γ_S^p becomes smaller as the surfactant alkyl-chain length increases. When the alkyl chain is too long, however, γ_S^p is not affected by the alkyl-chain length because of its increased flexibility. Thus, the substrate surface energy γ_S^p component is considered to exhibit minimum at pertinent n values. Although measured n-dependence of γ_S^p given in Section 7-3 does not necessarily agree with this model precisely, it is considered to be a result of rather small γ_S^p values for precise measurements. On the contrary, γ_S^d is not significantly affected by the surfactant alkyl-chain alignment. The reason is as follows. The substrate surface is considered to be covered with $-CH_2-$ group, when surfactant alkyl chains lie parallel to the substrate surface. Even when surfactant alkyl chains lie perpendicular to the substrate surface, almost all the substrate surface area is covered with $-CH_2-$ group of nS propyl chain, as is shown in Fig. 7-4 . Moreover, γ_c , which is shown to nearly equal γ_S^d in Section 6-3-2, is known not to differ very much (24 erg/cm^2 for $-CH_3$[1] and 31 erg/cm^2 for $-CH_2-$[2]). Consequently, anchoring strength becomes maximum for surfactants with pertinent-length alkyl chain which makes γ_S^p minimum. This is consid-

ered to be the origin of the n-dependence (of B_θ) which was observed in Section 4-4-1.

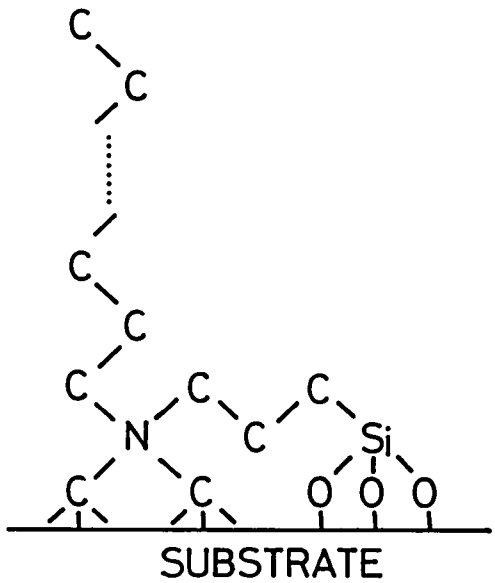

Fig. 7-4 Schematic drawing of a surfactant nS molecule with a vertically aligned alkyl chain on a substrate surface.

7-5. Summary

Anchoring-strength coefficient B_θ can be estimated by substrate surface-energy components, γ_S^d and γ_S^p, and liquid-crystal surface-energy parameters, γ_{L0}^d, $\Delta\gamma_L^d$, γ_{L0}^p, $\Delta\gamma_L^p$, and θ_p. The calculated B_θ values for MBBA at nS-treated substrate surfaces agree with experimentally derived B_θ values within an order of magnitude. Thus, the present model clarified weak-anchoring conditions obtained by substrates with organic-material layers. According to the present model, B_θ for MBBA becomes large for small γ_S^d or small γ_S^p. This can explain the observed surfactant alkyl-chain length dependence of B_θ,

because γ_S^p is considered to exhibit a minimum value at a pertinent length of surfactant alkyl chain and γ_S^d stays almost the same, independent of surfactant alkyl-chain length.

References

[1] E. G. Shafrin and W. A. Zisman, J. Colloid Sci., 7, 166 (1952)

[2] H. W. Fox and W. A. Zisman, J. Colloid Sci., 7, 428 (1952)

VIII. ANCHORING PARAMETER DEPENDENCE OF RELAXATION TIME IN CHOLESTERIC↔NEMATIC TRANSITION TYPE OF ELECTRO-OPTIC EFFECTS

8-1. Introduction

In the foregoing sections, relationships between liquid-crystal anchoring parameters and surfactant structure or surface-treatment procedures have been made clear. If relationships between liquid-crystal anchoring parameters and device characteristics are known, it is possible to improve device characteristics from the viewpoint of substrate-surface treatments. The following two sections are devoted to clarifying the relationships between liquid-crystal anchoring parameters and liquid-crystal display-device characteristics and showing the improvement of characteristics for liquid-crystal display devices. The display devices, which are taken up in this study, are storage type of liquid-crystal matrix display devices utilizing cholesteric↔nematic transition of dielectrically positive cholesteric liquid crystals.

Segment type of liquid-crystal display devices, utilizing the twisted-nematic mode, are now widely used for wrist watches, pocketable calculators, etc. Research and development on liquid-crystal display devices are naturally directed to a color display and a matrix-addressed display. For the matrix-addressed display, both a multiplexing scheme for the twisted-nematic mode, the dynamic scattering mode, etc. and coupling with active switching elements are considered. Especially for the character display, the multiplexing scheme for the twisted-nematic mode has reached the practical use stage. Matrix display panels with 16 multiplexing ratio are presently available. Those with 32 multiplexing ratio are under development. The twisted-nematic mode has, however, some disadvantages, such as lowering contrast ratio and limitation in viewing angle when utilized in

a highly multiplexed scheme. Moreover, the coupled liquid-crystal display devices with active switching elements have serious problems in regard to manufacturing cost, etc. On the contrary, the cholesteric↔nematic transition mode is very effective for a character-display use, although it is not suited for a dynamic display, such as television-screen display. The reason is that the cholesteric↔nematic transition mode is free from the "cross talk" problem and enables scanning more than 100 lines. Also, the display panel utilizing the cholesteric↔nematic transition mode has an internal memory effect.

These distinctive features for cholesteric↔nematic transition mode originate in a fast relaxation from a field-induced nematic texture to a quiescent cholesteric texture, which is produced by the homeotropic-alignment condition at the substrate surface. Consequently, the homeotropic-alignment condition at the substrate surface is of practical importance for the cholesteric↔nematic transition mode, whose characteristic performances strongly depend on the anchoring strength at the substrate surface.

In Section 8-2, a model is presented for the liquid-crystal orientational relaxation during the transition from the field-induced nematic to the quiescent cholesteric texture. The anchoring-parameter dependence of the transition time is considered. Section 8-3 presents experimental results for the anchoring-parameter dependence of the nematic→cholesteric transition time. Discussions are made in Section 8-4 on the comparison of the relaxation model and experimental results. A summary of this section is presented in Section 8-5.

8-2. Relaxation Process Consideration

Before describing the nematic→cholesteric relaxation process,

consider the cholesteric texture under no external electric field, which is the final state in the relaxation process. The field-induced texture is the nematic homeotropic texture, because the dielectric anisotropy for the liquid-crystal materials considered is positive. The cholesteric texture under no external electric field strongly depends on easy-axis angle Θ of anchoring parameters. However, the subject in this study is limited to the $\Theta \simeq 0°$ cases, which are favorable for practical devices.

In a cell with $\Theta \simeq 0°$ boundary conditions, cholesteric liquid-crystals exhibit several textures in accordance with layer thickness ℓ and intrinsic pitch length P_0 .

First, consider the case when $\ell/P_0 \lesssim 1$. When liquid-crystal layer thickness ℓ is nearly equal to, or smaller than, a critical thickness ℓ_c ($\ell \lesssim \ell_c$), cholesteric liquid crystals form a homeotropic nematic texture. Critical layer thickness ℓ_c is calculated[1] under the "strong anchoring" condition as

$$\ell_c = (K_{33}/2K_{22}) P_0 \quad . \tag{8-1}$$

In general, K_{33} is twice as large as K_{22} . Consequently, the present $\ell \lesssim \ell_c$ condition is represented by $\ell \lesssim P_0$, i.e., $\ell/P_0 \lesssim 1$. In the case of "weak anchoring" condition, critical layer thickness ℓ_c' becomes smaller than ℓ_c and the ratio ℓ_c'/ℓ_c is given by

$$\ell_c'/\ell_c = \beta \cot (\pi\ell_c'/2\ell_c) \quad . \tag{8-2}$$

Figure 8-1(a) shows a polarized microscopic photograph of a sample cell satisfying the condition $\ell \lesssim \ell_c$. Cell gap ℓ is 13.7 μm and the liquid-crystal material is a cholesteric-nematic mixture with P_0 = 13.7 μm. The nematic material used is a eutectic mixture of 4-cyano-4'-*n*-heptylbiphenyl, 4-cyano-4'-*n*-pentoxybiphenyl, 4-cyano-4"-*n*-pentyl-*p*-terphenyl, 4-*n*-heptyl-4'-cyanophenyl-cyclohexane, and 4-*n*-pentyl-4'-cyanobiphenyl-4-cyclohexane in 27.4 : 25.7 : 9.3 : 27.2 : 10.4 weight ratio. The cholesteric material used is cholesteryl nonanoate

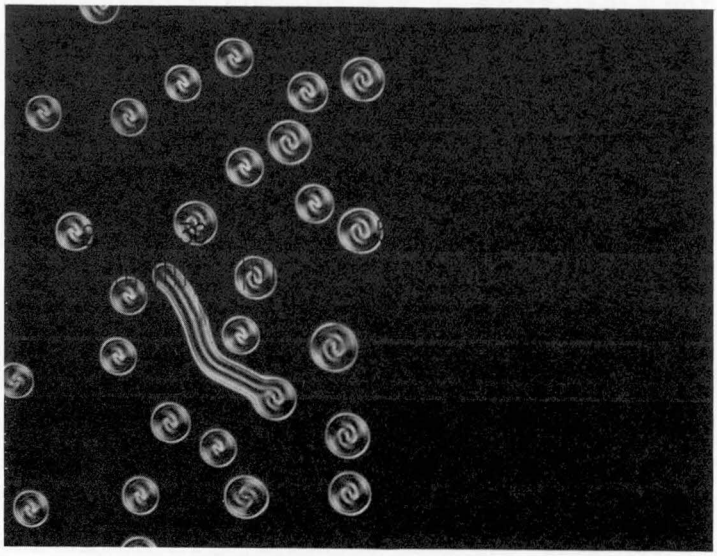

(a)

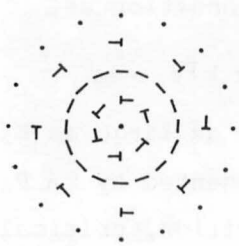

(b)

Fig. 8-1 Cholesteric liquid crystal between parallel substrates with $\Theta = 0°$ condition ($P_0 = 13.7$ μm, $\ell = 13.7$ μm; $\ell/P_0 \lesssim 1$). (a) Polarized microscopic photograph (10×10, ∿10.5 μm/div.) and (b) molecular alignment model for a bubble domain [Refs. 2 and 3].

and its concentration is 1.47 wt.% . This cholesteric-nematic mixture is used in various weight ratios for the following liquid-crystal texture observations. The surface-treatment material used is

16S, which introduces the $\Theta = 0°$ condition. In this case, $\ell \lesssim \ell_c$ ($= P_0 = 13.7$ μm) is satisfied and the homeotropic texture is induced. The bright islands in the dark homeotropic region in Fig. 8-1(a) are so-called bubble domains. The bubble domains are known[2] to appear in a liquid-crystal cell, where ℓ is nearly equal to ℓ_c, when the liquid-crystal cell is cooled down through the isotropic→cholesteric transition point or when an applied DC or a low-frequency AC electric field, which is strong enough to induce electrohydrodynamic turbulence, is turned off. The bubble domain is considered[2,3] to be caused by a liquid-crystal molecular alignment illustrated in Fig. 8-1(b).

Next, consider the case when $1 < \ell/P_0 < \sim 2$. In this case, the stripe texture is obtained as shown in Fig. 8-2(a). In Fig. 8-2(a), $\ell = 12.1$ μm and $P_0 = 8.1$ μm ($\ell/P_0 \simeq 1.5$). In this case, the cholesteryl nonanoate weight ratio is 2.49 wt.%. The stripe texture is considered[4] to be caused by the molecular alignment forming helixes, whose axes are almost parallel to the substrate surface (Fig. 8-2(b)).

In $\ell/P_0 > \sim 2$ cases, the stripe texture is broken and the texture exhibits somewhat winding features, as shown in Fig. 8-3. The texture in Fig. 8-3 was obtained for a sample with $\ell = 11.8$ μm and $P_0 = 4.7$ μm ($\ell/P_0 \simeq 2.5$). The cholesteryl nonanoate weight ratio in its mixture used is 4.26 wt.%.

When the pitch length is shorter and the condition $\ell/P_0 > \sim 3$ is satisfied, a spiral texture is formed, as shown in Fig. 8-4(a). In this case the cholesteric weight ratio is 6.26 wt.% ($P_0 = 3.2$ μm) and cell gap is 11.2 μm. Figure 8-4(b) is another example of a spiral texture which is observed in larger - ℓ/P_0 cases. The liquid-crystal material used is a cholesteric-nematic mixture which is composed of 4'-methoxybenzylidene-4-*n*-butylaniline, 4'-butoxybenzylidene-4-*n*-cyanoaniline, and cholesteryl chloride in 68:20:12 weight ratio. Its pitch length is 1.4 μm and cell gap is 11.5 μm. For spiral texture,

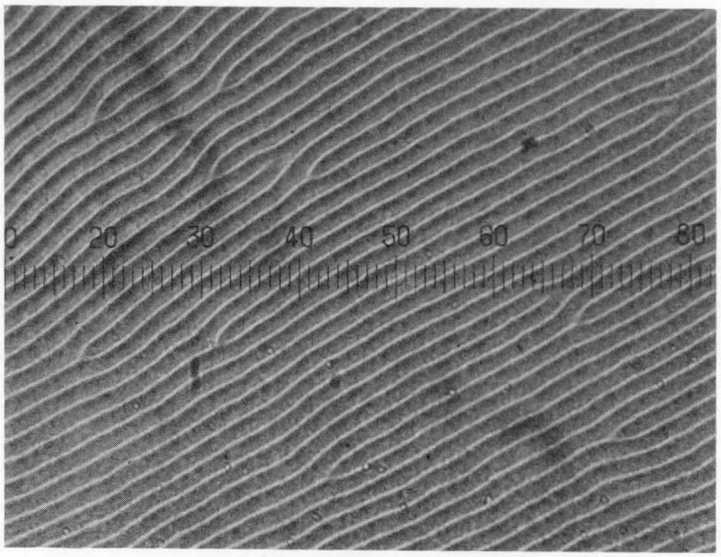

(a)

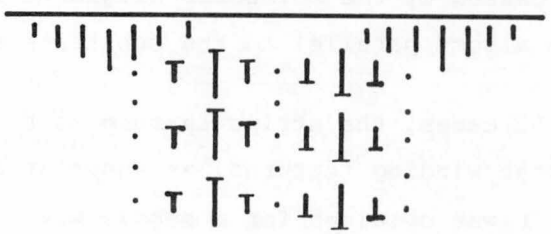

(b)

Fig. 8-2 Cholesteric liquid crystal between parallel substrates with $\Theta = 0°$ condition ($P_0 = 8.1$ μm, $\ell = 12.1$ μm; $\ell/P_0 \simeq 1.5$). (a) Polarized microscopic photograph (10×10, ∿10.5 μm/div.) and (b) molecular alignment model for a stripe texture [Ref. 4].

it is considered that the helical axis is perpendicular to the substrate surface in almost all the bulk region, because the electric capacitance is measured as almost the same for both planar texture and spiral texture. Consequently, it can be proposed that the liquid-

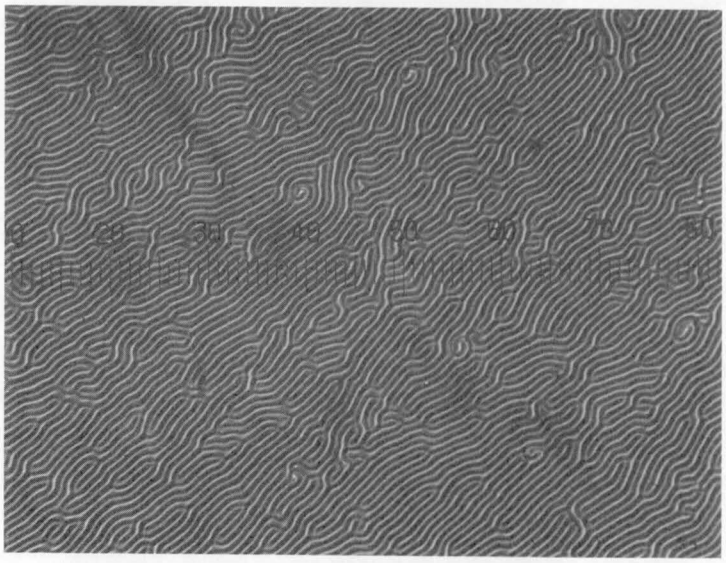

Fig. 8-3 Polarized microscopic photograph (10×10, ∿10.5 μm/div.) showing cholesteric liquid crystal between parallel substrates with $\Theta = 0°$ condition ($P_0 = 4.7$ μm, $\ell = 11.8$ μm; $\ell/P_0 \simeq 2.5$).

crystal molecular alignment is such as shown in Fig. 8-4(c) . The bright line in Figs. 8-4(a) and (b) is caused by light scattering and depolarization by the $\tau^{\pm}$ disclination lines running parallel to the substrate surface. The points where three bright lines join in Figs. 8-4(a) and (b) correspond to the λ^{-} disclination line perpendicular to the substrate surface.

In the following, on the basis of above considerations on cholesteric textures, consider the relaxation process from the field-induced homeotropic texture to those quiescent cholesteric textures. In the case of $\ell/P_0 \lesssim 1$, it is needless to say that no transition occurs for the external electric-field removal, as the energetically stable texture under no external field is the same homeotropic nematic texture as that under the external electric field.

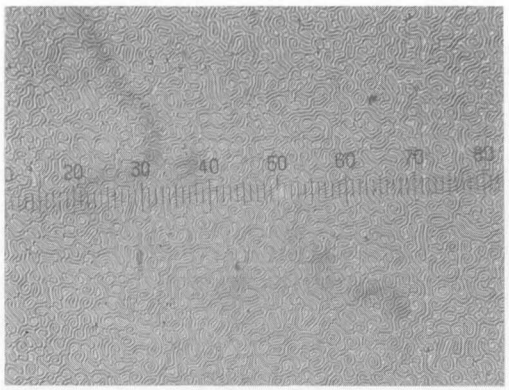

(a)

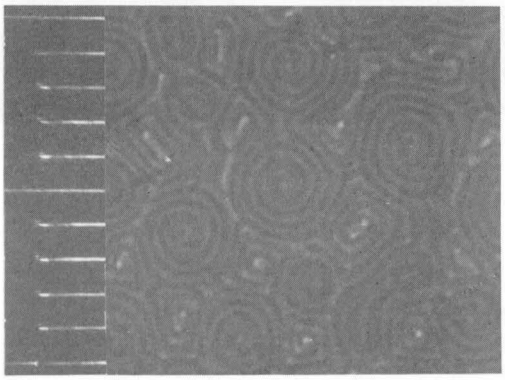

(b)

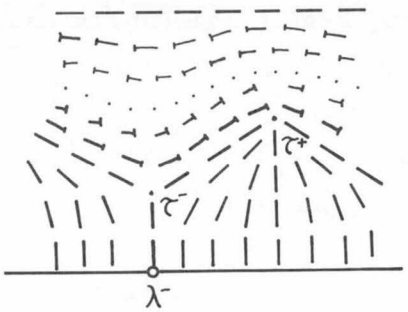

(c)

Fig. 8-4 Cholesteric liquid crystal between parallel substrates with $\Theta = 0°$ condition. (a) Polarized microscopic photograph (10×10, ∿10.5 μm/div.) when $P_0 = 3.2$ μm, $\ell = 11.2$ μm, and $\ell/P_0 \simeq 3.5$, (b) Polarized microscopic photograph (15×40, 10 μm/div.) when $P_0 = 1.4$ μm, $\ell = 11.5$ μm, and $\ell/P_0 \simeq 8.2$, and (c) proposed molecular alignment model for a spiral texture.

The nematic→cholesteric relaxation in the case of $1 < \ell/P_0 < \sim 2$ is considered to be such as illustrated in Fig. 8-5 , because the helical axis in the quiescent cholesteric texture is almost parallel to the substrate. This relaxation is approximately the same as the helical winding discussed by Jakeman *et al.*[5] . Consequently, relaxation time τ is given[5] by

$$\tau = \eta / K_{22} \, (2\pi/P_0)^2 \quad . \qquad (8\text{-}3)$$

This τ value is of the order of 10^2 ms for P_0 satisfying the inequality $1 < \ell/P_0 < \sim 2$ and practical ℓ values ($\ell \simeq 10$ μm). This $1 < \ell/P_0 < \sim 2$ case, however, is of less interest in a sense of display device applications, because no effective electro-optic effects have been observed.

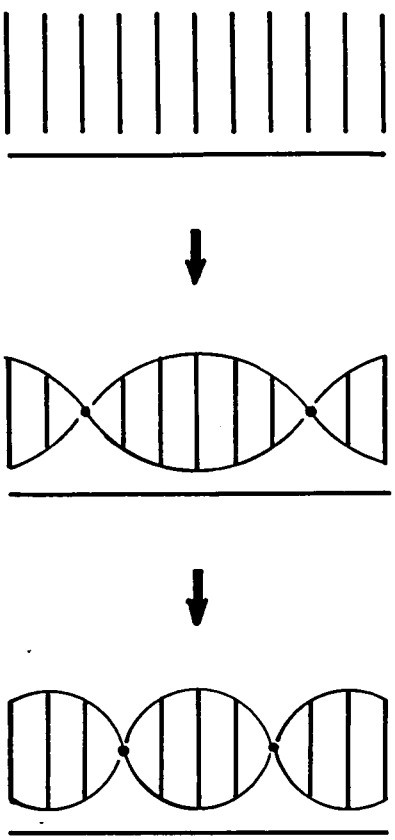

Fig. 8-5 Molecular reorientation model for a nematic→cholesteric relaxation, when $1 < \ell/P_0 < \sim 2$.

In cases of $\ell/P_0 > \sim 3$, a comparatively rapid recovery of the quiescent cholesteric texture is observed. This fast relaxation is very useful for display device applications. Consequently, in the following, the relaxation in this $\ell/P_0 > \sim 3$ case, i.e., the relaxation from a field-induced homeotropic texture to the spiral texture is considered in details.

During the nematic → cholesteric relaxation, the light transmission through a liquid-crystal layer changes, as shown in Fig. 8-6(a). That is, the light transmission exhibits a hump("G*") before it reaches minimum("G'") and finally recovers its initial magnitude("S"). On the contrary, the electric capacitance of the liquid-crystal layer exhibits a monotonic decrease, as shown in Fig. 8-6(b) . From these observations, it is plausible to consider that a helical orientation, with the helical axis perpendicular to the substrate surface, is already obtained at "G*" state[6,7]. Moreover, it is reported[8,9] that the helical pitch length at "G*" state is about twice as large as the intrinsic pitch length P_0 . Consequently, it is possible to divide the nematic→cholesteric relaxation process into two steps. In the first step, a helical orientation with pitch length $P \simeq 2P_0$ is formed. Then, in the second step, the pitch length reduces to its intrinsic value P_0 .

Relaxation time τ_1 for the "G*" state formation is considered to correspond to the winding ($P = \infty \rightarrow 2P_0$) time in the bulk, which is not affected by boundary conditions. Consequently, it seems plausible to apply formula (8-3) to τ_1 . On the contrary, the relaxation time for the second step is considered to be subject to the molecular realignment near the substrate surface and, therefore, to be strongly affected by anchoring strength. In the following, the anchoring-strength dependence of the relaxation time is considered for the second step in details.

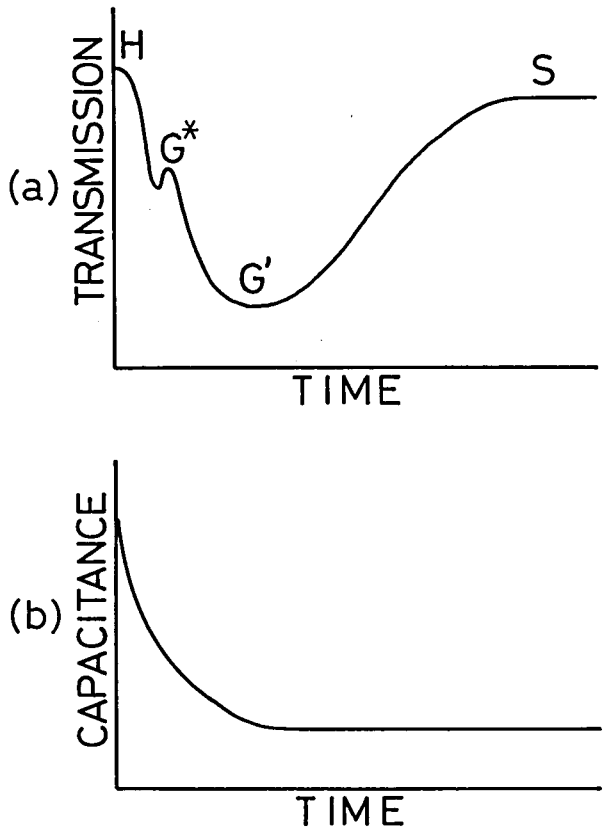

Fig. 8-6 Nematic → cholesteric relaxation when $\ell/P_0 > \sim 3$. (a) Light transmission and (b) electric capacitance changes.

In the first step of nematic → cholesteric relaxation, a continuous change of director orientation is expected, as shown in Fig. 8-7. Once a helical orientation is formed, however, no continuous contraction of the helical pitch can occur without the aid of disclinations. A possible noncontinuous contraction of the helical pitch is illustrated in Fig. 8-8. In this case, the helical-pitch contraction goes on independently of the existence of transient layers. According to the polarized microscopic observation, which is shown in Fig. 8-9, however, a continuous change in the patterns occurs during the second-step relaxation time. As stated before, these microscopic patterns

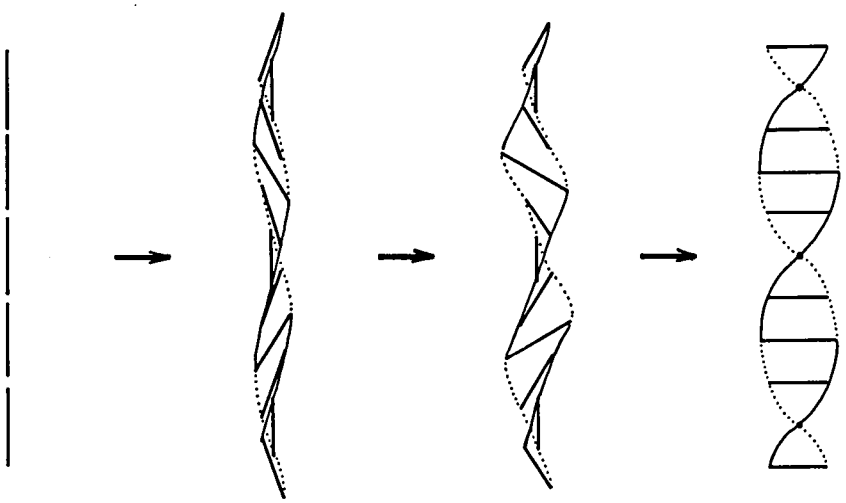

Fig. 8-7 Molecular reorientation model for the first step of nematic → cholesteric relaxation, when $\ell/P_0 > \sim 3$.

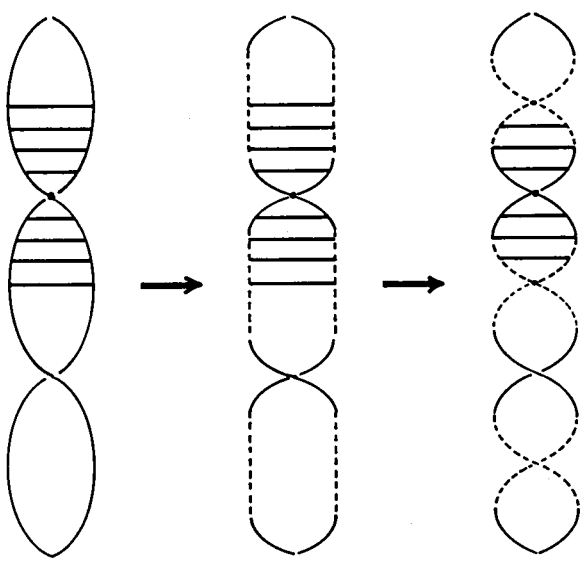

Fig. 8-8 Possible noncontinuous contraction of a cholesteric helical pitch.

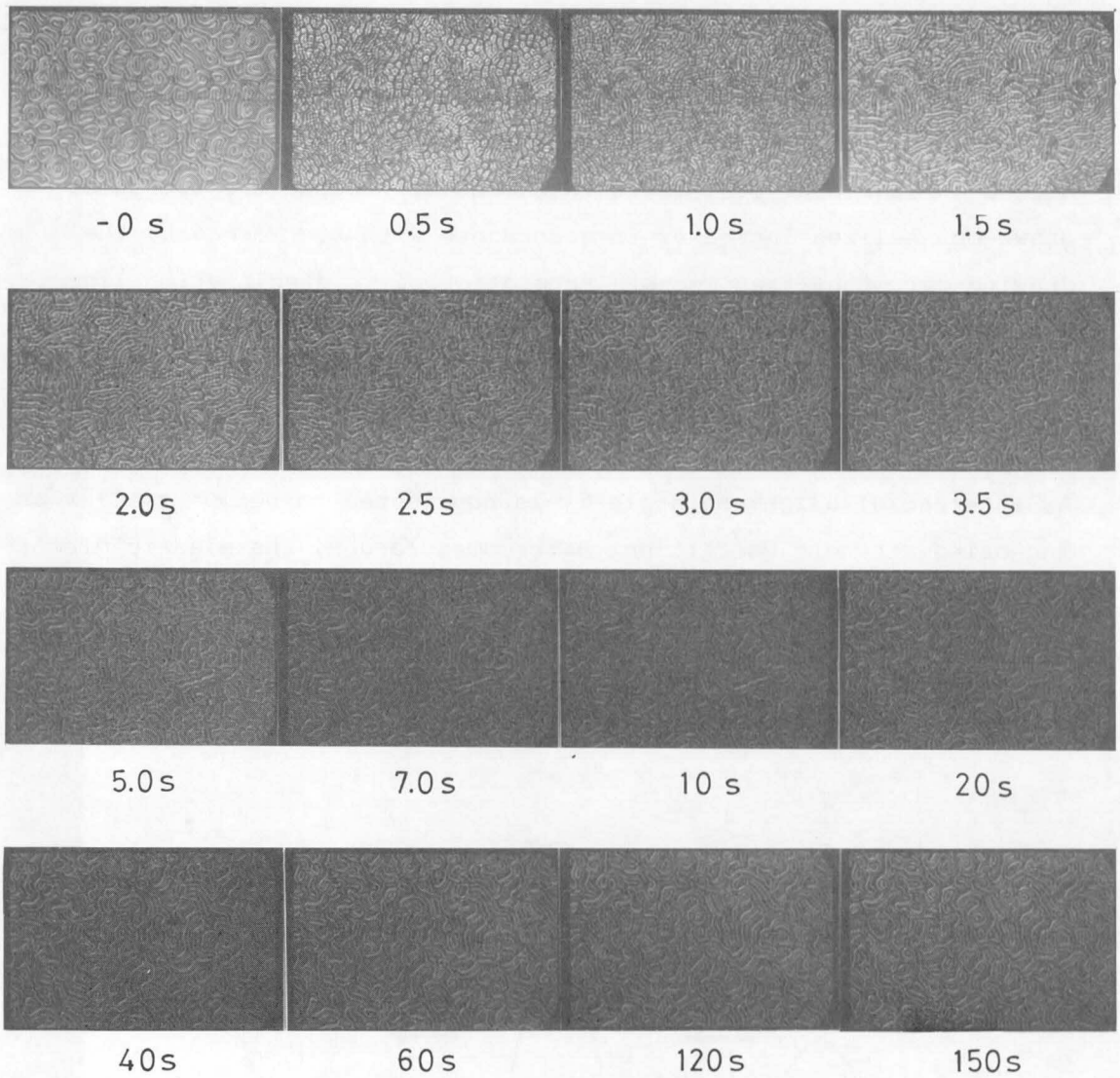

Fig. 8-9 Polarized microscopic observation of the second-step nematic → cholesteric relaxation, when $\ell/P_0 > \sim 3$.

are introduced by disclination lines in the transient layer. Thus, the helical-pitch contraction, as is shown in Fig. 8-8 , seems unlikely and the following model containing a motion of disclination lines is considered to be more plausible. In this model, as is shown in

Fig. 8-10 , the helix is drawn out of the transient layers and a helical-pitch contraction is carried out continuously.

According to this "drawing-out" model, the relaxation time will depend on liquid-crystal layer thickness ℓ, because the number of drawn-out helixes increases in accordance with ℓ. Moreover, the drawing-out of helixes means a separation of $\tau^{\pm}$ disclination lines. Therefore, it will be subject to anchoring strength.

Here, consider the relationships between anchoring strength and disclination-line separation, that is transient-layer thickness ξ. As interfacial alignment angle θ_0 is considered to become smaller as anchoring-strength coefficient B_θ becomes larger, the elastic distortion energy in the transient layer of constant thickness ξ is larger as B_θ is larger. Thus, larger B_θ acts to increase ξ for elastic energy reduction, that is, larger B_θ helps $\tau^{\pm}$ disclination lines sepa-

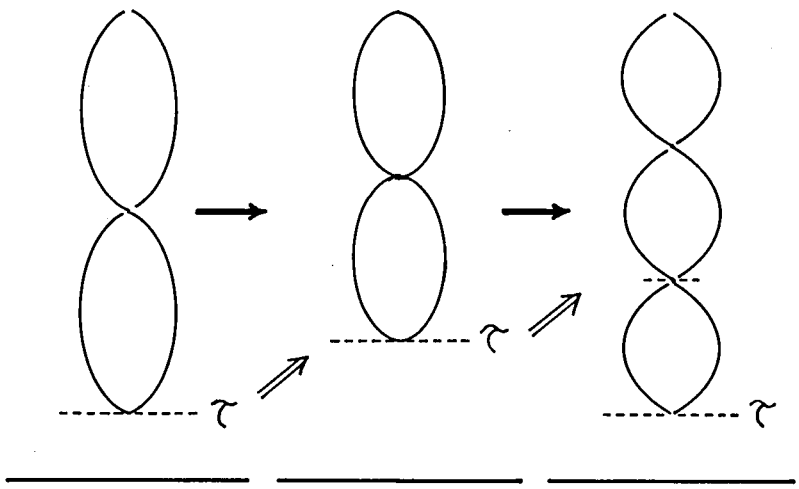

Fig. 8-10 Proposed "drawing-out" model for molecular reorientation during the second-step nematic→cholesteric relaxation, when $\ell/P_0 > \sim 3$.

rate from the substrate surface. Consequently, the second-step relaxation time is expected to be shortened as B_θ increases.

As a conclusion, the "drawing-out" model is considered to be plausible from the polarized microscopic observation for the second step of the nematic→cholesteric relaxation. As the second-step relaxation time τ_2 is generally more than ten times as large as the first-step relaxation time τ_1, the nematic→cholesteric relaxation time τ_{rp} for $\ell/P_0 > \sim 3$ cases can be represented by τ_2. Consequently, relaxation time τ_{rp} ($\simeq \tau_2$) is considered to be shortened by decreasing liquid-crystal layer thickness ℓ or increasing anchoring-strength coefficient B_θ.

8-3. Experimental Results on Anchoring-Parameters Dependence of Nematic→Cholesteric Relaxation Time

8-3-1. Easy-axis angle dependence

Liquid-crystal layer thickness dependence for the nematic (homeotropic)→cholesteric (spiral) relaxation time was examined for several surface-treatment conditions. The surfactants used for the substrate-surface treatment are a homologous series of *n*-alkylamines nA ($n = 6 \sim 18$). Experiments were carried out by using a cholesteric liquid-crystal material (MBC) composed of 4'-methoxybenzylidene-4-*n*-butylaniline(MBBA), 4'-*n*-butoxybenzylidene-4-cyanoaniline(BBCA), and cholesteryl chloride(CC). The mixed ratio is 70:20:10 in weight. Its dielectric anisotropy is positive.

Measured ℓ-dependence of relaxation time τ_{rp} is shown in Fig. 8-11. From Fig. 8-11, an empirical formula:

$$\tau_{rp} \propto \ell^m \qquad (8\text{-}4)$$

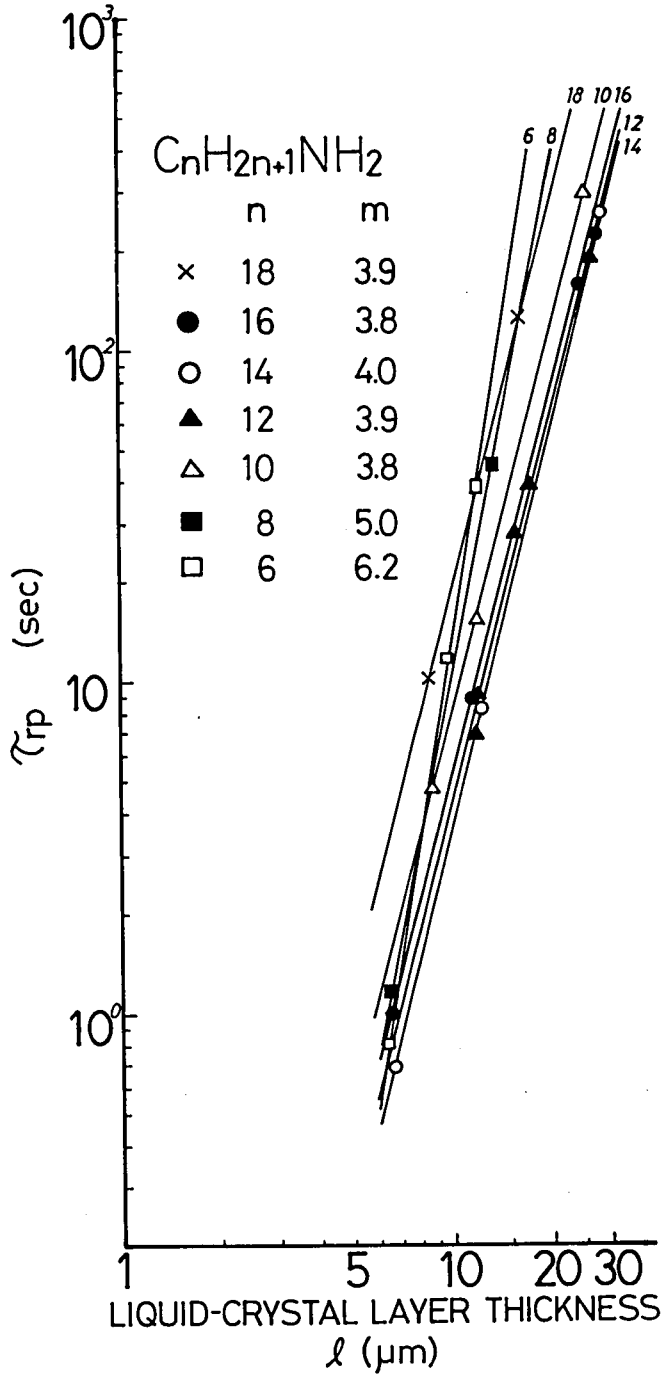

Fig. 8-11 Liquid-crystal thickness dependence of nematic → cholesteric relaxation time τ_{rp}.

is obtained, where m depends on the surfactants used for the substrate-surface treatment. Power m is 4, in the cases when substrates are treated with 10A∿18A. When the substrates are treated with 8A or 6A, on the contrary, m value obtained is 5 or 6, respectively.

Easy-axis angle Θ was previously measured for MBBA on these substrates. It was found that $\Theta = 0°$ for 14A∿18A, $\Theta = \sim 3°$ for 10A∿12A, $\Theta = \sim 12°$ for 8A, and that $\Theta = \sim 24°$ for 6A (see Table 4-2(c)). As MBBA is the main (70 wt.%) component of the cholesteric mixture MBC, it is plausible to consider that Θ value for MBC is nearly the same as the Θ values for MBBA. Consequently, the relationships between m and Θ are so obtained that $m = 4$ for $\Theta \simeq 0°$ cases ($n = 10 \sim 18$ for nA) and m becomes larger for larger Θ ($m = 5$ for $\Theta \simeq 12°$ and $m = 6$ for $\Theta \simeq 24°$).

The Θ-dependence of relaxation time τ_{rp} is exhibited in Fig. 8-12, which was transformed from Fig. 8-11. In Fig. 8-12, Θ values are also shown on the axis of abscissas. Although it is impossible to reduce the Θ-dependence of τ_{rp} strictly from Fig. 8-12, because the anchoring-strength dependence of τ_{rp} is also included in the τ_{rp} vs n curves in Fig. 8-12, it is plausible to consider that τ_{rp} for larger-Θ cases is generally larger than that for $\Theta = 0°$, and a minimum τ_{rp} is obtained in $\Theta = 0°$ cases. The differences among τ_{rp} values for different Θ values become larger as liquid-crystal layer thickness ℓ becomes larger. It is because τ_{rp} strongly depends on ℓ, as represented by Eq. (8-4).

8-3-2. Anchoring-strength dependence

The B_θ-dependence of relaxation time τ_{rp} was examined for MBC on such surfaces as nS ($n = 14,16,18$), nCl ($n = 12,16,18$), nS ($n = 18$), and FS150, where $\Theta = 0°$ is expected. As τ_{rp} is proportional to ℓ^4 in $\Theta = 0°$ cases, τ_{rp} can be represented as

$$\tau_{rp} = \alpha' \ell^4 \quad . \tag{8-5}$$

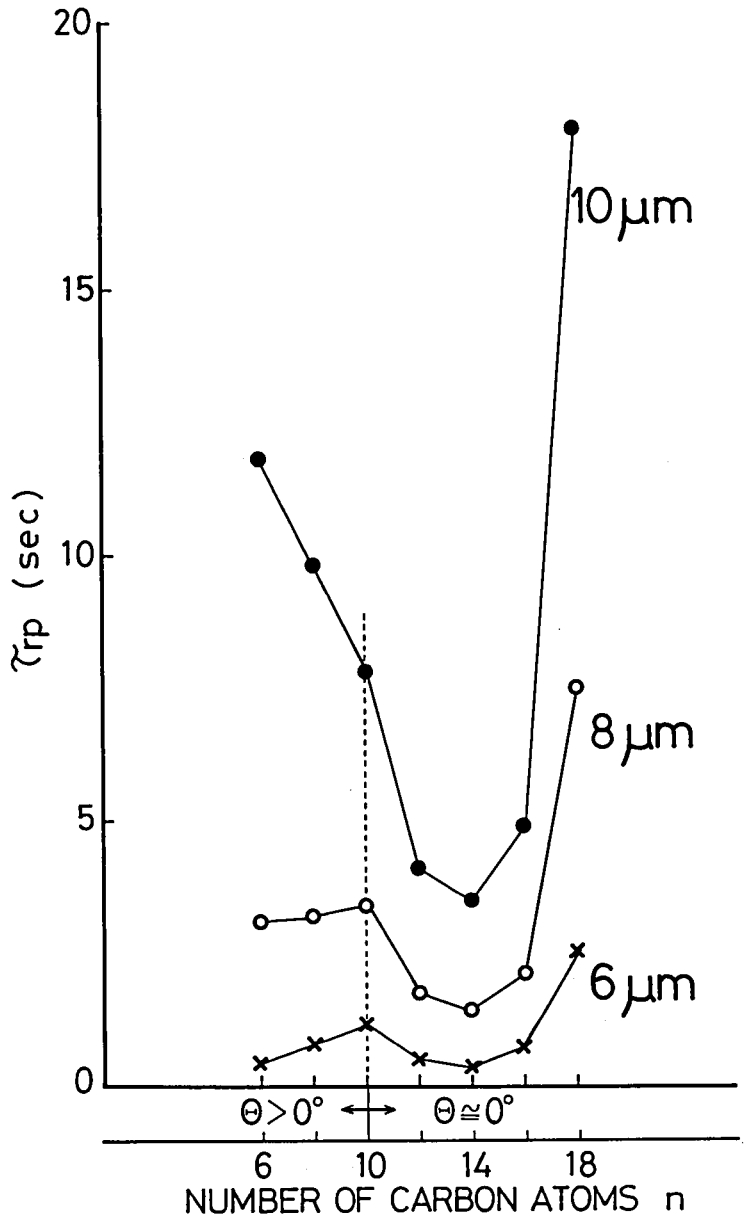

Fig. 8-12 Easy-axis angle dependence of nematic→ cholesteric relaxation time τ_{rp}.

Relaxation time τ_{rp} was measured for samples with various thickness ℓ values, as previously shown in Fig. 8-11.

From these measurements, derived relaxation coefficient α' values were as listed in Table 8-1, In Table 8-1, previously-measured B_θ and Θ values for MBBA are also listed. Here, assume again that B_θ for MBC is nearly the same as B_θ for MBBA which occupies 70 wt.% in MBC. Then, relationships between α' and B_θ for MBC are obtained as shown in Fig. 8-13 . Figure 8-13 exhibits a tendency that α' decreases as B_θ becomes larger. That is, the relaxation time τ_{rp} is shorter for larger B_θ .

Table 8-1 Nematic→cholesteric relaxation coefficient α' for a cholesteric mixture MBC and anchoring parameters Θ and B_θ for a nematic component MBBA.

	α' ($\times 10^{12}$ s/cm^4)	B_θ ($\times 10^{-3}$ erg/cm^2)	Θ (deg)
14A	3.5	4.0 ± 0.7	0
16A	4.9	3.5 ± 1.2	0
18A	18	2.5 ± 0.6	0
12Cl	7.3	2.7 ± 1.2	0
16Cl	6.3	7.6	0
18Cl	7	2.7 ± 0.3	0
18S	3.6	11 ± 4	0
FS150	3.2	10 ± 2	0

8-4. Discussions

The experimental results in Section 8-3 show that relaxation time τ_{rp} from the field-induced nematic state to the quiescent cholesteric spiral-texture, depends on the liquid-crystal layer thickness and the anchoring parameters. These results agree qualitatively with

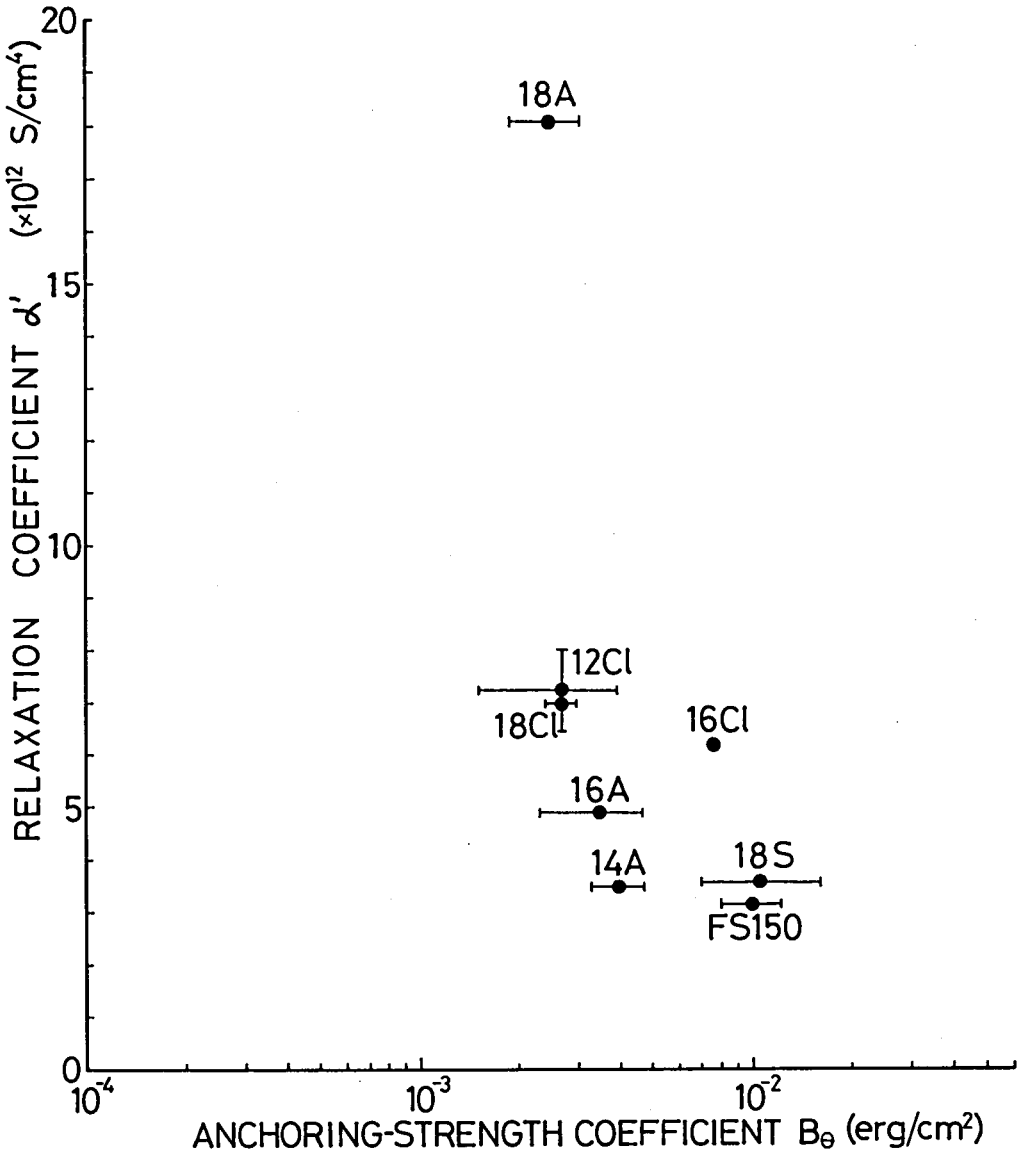

Fig. 8-13 Relationships between nematic→cholesteric relaxation coefficient α' for a cholesteric mixture MBC and anchoring-strength coefficient B_θ for a nematic component MBBA.

relaxation time τ_{rp} anchoring-parameter dependence, which was predicted in Section 8-2. Consequently, it seems approximately valid to

use nematic anchoring parameters for cholesteric ones, as long as nematic materials amount to a major part of the cholesteric mixture. The observed strong liquid-crystal layer thickness dependence of the relaxation time ($\tau_{rp} \propto \ell^4$ for $\Theta = 0°$) is considered to demonstrate that the interfacial relaxation phenomenon is essential to the nematic→cholesteric relaxation process, and agrees with the ℓ-dependence of τ_{rp} predicted by the "drawing-out" model, which expects a smaller τ_{rp} value for a larger B_θ value.

For liquid-crystal material dependence of relaxation time τ_{rp}, it is reported[10] that τ_{rp} is relatively short for cholesteric mixtures with smectic phases, as compared with cholesteric mixtures without smactic phases. The B_θ dependence of τ_{rp}, which was made clear in this study, can be considered to be identical with existing liquid-crystal material dependence. At the interface, the translational symmetry of liquid-crystal molecular distribution is broken. This breakdown in translational symmetry is the same condition as for a smectic layer structure. That is, it is considered that a smectic ordering is formed close to the interface, such as cholesteric materials with smectic phases exhibit a latent smectic ordering. The strong forces to align liquid-crystal molecules homeotropically at the interface play an analoqous role to forces which produce the smectic-A ordering. Consequently, it is plausible that a larger B_θ condition at the interface makes relaxation time τ_{rp} shorter, as the latent smectic ordering of cholesteric materials does.

As experimentally clarified in this section, nematic→cholesteric relaxation time τ_{rp} becomes minimum, when the easy-axis angle Θ is zero and anchoring-strength coefficient B_θ is largest. Moreover, nematic liquid-crystal anchoring parameters approximately substitute for those for cholesteric mixtures, if the nematic materials are main cholesteric mixture components. As a desirable surface treatment can be designed for obtaining $\Theta = 0°$ and large-B_θ conditions in accordance

with this study, it is possible to realize a cholesteric↔nematic transition type of liquid-crystal display device with an improved characteristic, such as a fast nematic→cholesteric relaxation.

8-5. Summary

Cholesteric↔nematic transition mode, which is very effective for a character-display use, has been characterized by its fast relaxation from the field-induced nematic state to the quiescent cholesteric spiral structure. The "drawing-out" model has been proposed for the director realignment during the nematic→cholesteric relaxation time τ_{rp}. It has been shown that τ_{rp} depends on liquid-crystal layer thickness and anchoring parameters. When the anchoring parameters for cholesteric mixtures are considered to be approximately the same as those for nematic materials, which are their main components, the experimental results agree qualitatively with the results expected by the "drawing-out" model. Those are summarized as follows.

1) Relaxation time τ_{rp} is proportional to the m-th power of liquid-crystal layer thickness ℓ, where m is 4 for $\Theta = 0°$ cases and m becomes larger when Θ is larger than $0°$.

2) When Θ is zero, larger anchoring-strength coefficient B_θ makes τ_{rp} shorter.

3) Relaxation time τ_{rp} becomes minimum in $\Theta = 0°$ cases.

These results suggest that the anchoring condition for zero easy-axis angle and for large anchoring-strength coefficient is desired for a fast nematic→cholesteric relaxation.

References

[1] M. Luban, D. Mukamel, and S. Shtrikman, Phys. Rev. A, 10, 360 (1974)

[2] M. Kawachi, O. Kogure, and Y. Kato, Jpn. J. Appl. Phys., 13, 1457 (1974)

[3] T. Akahane and T. Tako, Jpn. J. Appl. Phys., 15, 1559 (1976); T. Akahane and T. Tako, Mol. Cryst. Liq. Cryst., 38, 251 (1977)

[4] P. E. Cladis and K. Kleman, Mol. Cryst. Liq. Cryst., 16, 1 (1972)

[5] E. Jakeman and E. P. Raynes, Phys. Lett., 39A, 69 (1972)

[6] T. Ohtsuka and M. Tsukamoto, Jpn. J. Appl. Phys., 12, 22 (1973)

[7] R. A. Kashnow, J. E. Bigelow, H. S. Cole, and C. R. Stein, in *Liquid Crystal and Ordered Fluids* edited by J. F. Johnson and R. S. Porter (Plenum Press, New York, 1974) Vol. 2 , p. 483

[8] M. Kawachi, O. Kogure, S. Yoshii, and Y. Kato, Jpn. J. Appl. Phys., 14, 1063 (1975)

[9] M. Kawachi, K. Kato, and O. Kogure, Jpn. J. Appl. Phys., 16, 1263 (1977)

[10] C. Tani, Jpn. J. Appl. Phys., 18, 1387 (1979)

IX. CHARACTERISTICS OF CHOLESTERIC↔NEMATIC TRANSITION TYPE OF LIQUID-CRYSTAL DISPLAY DEVICES

9-1. Introduction

In the foregoing sections, we have derived the relationships between substrate surface-energy condition and liquid-crystal anchoring parameters and found out the surfactant materials and surface-treatment procedures to produce zero easy-axis angle and large anchoring-strength coefficient conditions. In addition, we have obtained in Section VIII that a fast nematic→cholesteric relaxation is obtained, when easy-angle θ is zero and anchoring-strength coefficient B_θ is large. Thus, it is possible to realize a cholesteric↔nematic transition type of liquid-crystal display device with such a characteristic as a fast nematic→cholesteric relaxation which is improved from the viewpoint of substrate-surface treatment.

In Section 9-2, the operational principle of cholesteric↔nematic transition type of liquid-crystal display devices is presented. It is stated that a fast nematic→cholesteric relaxation is needed for storage-type of matrix display. The panel construction of the storage type of liquid-crystal matrix display is presented in Section 9-3. Section 9-4 provides the characteristics of prototype display devices. A summary of this section is given in Section 9-5.

9-2. Operational Principles of Cholesteric↔Nematic Transition Type of Liquid-Crystal Display Devices

Liquid-crystal cells with homeotropic boundary condition, utilizing dielectrically positive cholesteric mixtures, have an electro-optic hysteresis effect[1,2], as shown in Fig. 9-1. The liquid-crys-

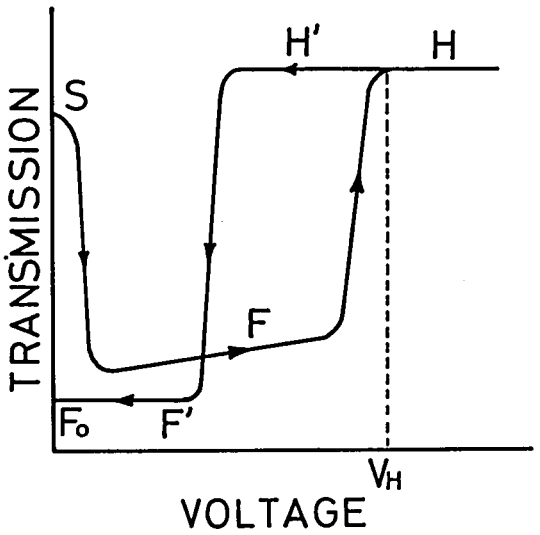

Fig. 9-1 Electro-optic hysteresis curve for dielectrically positive cholesteric liquid crystal between parallel substrates with $\Theta = 0°$ condition.

tal cell, in its quiescent state, assumes an almost transparent spiral texture "S". It changes into a scattering fan-shaped texture "F" by voltage application, and transforms at threshold volatage V_H to a homeotropic nematic texture "H" as a result of the field-induced cholesteric→nematic transition. The cell remains as a metastable homeotropic texture "H'" for a rather long time T, when the voltage is lowered from V_1 ($V_1 > V_H$) to V_2 ($V_H > V_2 > V_{H'} \simeq V_H/2$). When the applied voltage is switched off from V_1 (or V_2) to zero (Fig. 9-2(a) or (c)), rapid relaxation occurs from the transparent nematic texture "H" (or "H'") to initial quiescent texture "S" through a transient scattering cholesteric texture "G'" (Fig. 9-2(b) or (d)), (nematic→cholesteric relaxation time τ_{rp}). As explained in Section 8-2, light transmission during the nematic→cholesteric relaxation exhibits a hump "G*" before it reaches a minimum at state "G'" (Fig. 9-2(b)). The time interval for the transition from texture "H" or "H'" to texture "G*" is interpreted to be the helical winding time τ_1 represented by Eq. (8-3).

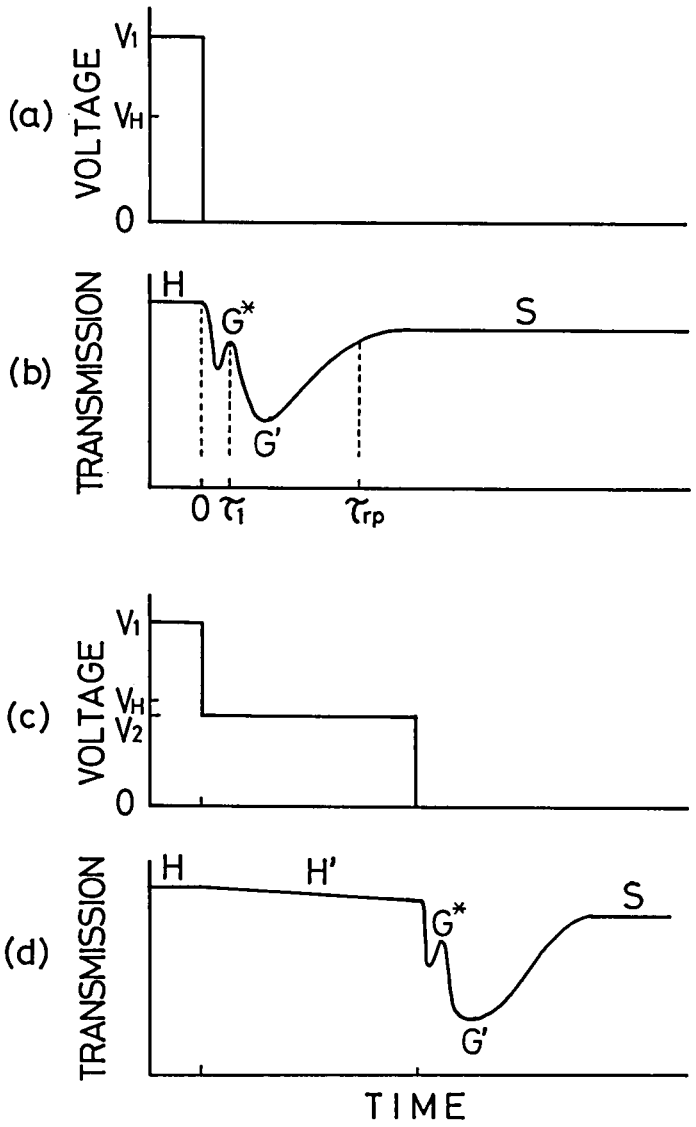

Fig. 9-2 Applied voltage and light-transmission change at non-selected picture elements.

If voltage V_2 is applied after a time interval t_0, such that $t_0 > \tau_1$ (Figs. 9-3(e) and (g)), a scattering texture "F'" is formed, which transforms to stored scattering texture "F_0" after the voltage removal (Figs. 9-3(f) and (h)). Thus, scattering texture "F_0" and transparent texture "S" can be formed and stored selectively by putting $t_0 > \tau_1$

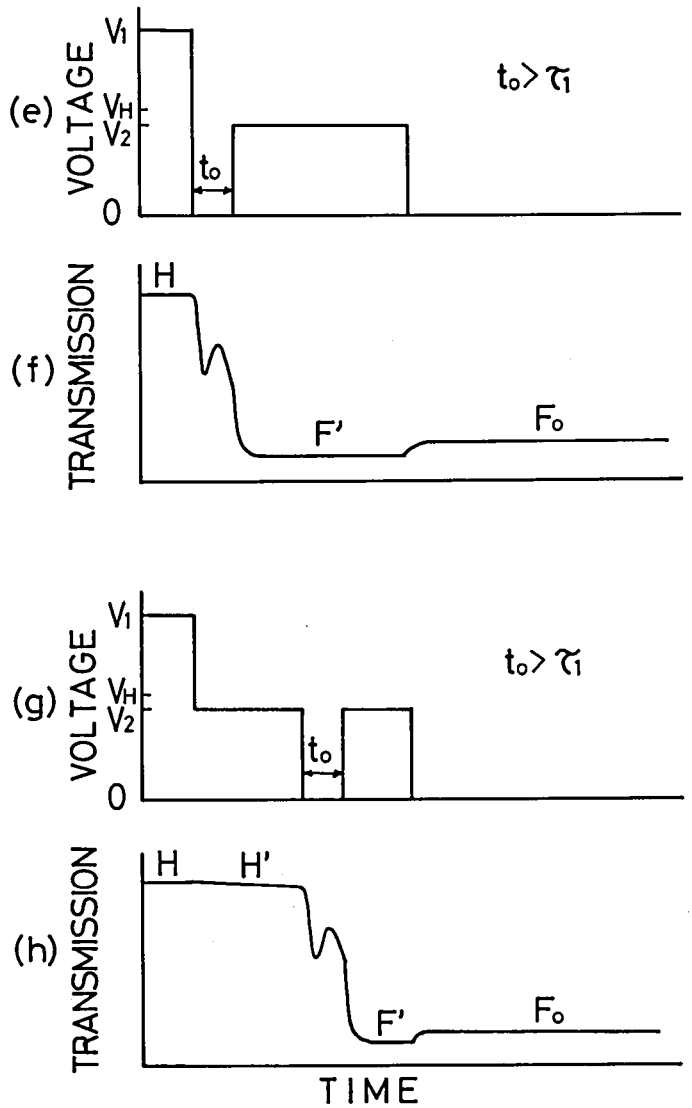

Fig. 9-3 Applied voltage and light-transmission change at selected picture elements.

(Figs. 9-3(e) and (f) or Figs. (g) and (h)) and $t_0 = 0$ (Figs. 9-2(c) and (d)) , respectively. After the applied voltage is removed, however, the transparent picture elements exhibit a transient light scattering during time interval τ_{rp} , as shown in Fig. 9-2(b) or (d) . As the displayed information is washed out during this time interval, the

time τ_{rp} is required to be as short as possible.

Figure 9-4 shows the actual addressing scheme in the writing process in a 3×3 matrix. Scanning signals are applied to the row electrodes and data signals are applied to the column electrodes. V(0) and $V(\pi)$ are AC pulses, which have the same height and 180° phase difference. The V(0) and $V(\pi)$ pulse heights are less than V_H. The scanning signals voltage is 0 for non-addressed lines, and $V(\pi)$ for an addressed line. The data signals voltage is V(0) for non-selected lines, and $V(\pi)$ for selected lines. Therefore, the voltage applied to the addressed and selected element is 0, and V or 2V is applied to the other elements. Through a total writing process, the applied voltage changes in such ways as $V \rightarrow 0 \rightarrow V$ or $0 \rightarrow V$ at the selected elements, and $V \rightarrow 2V \rightarrow V$ or $2V \rightarrow V$ at the non-selected elements. Consequently, the selected elements are written and the others aren't. After such a writing process, voltages for all elements are removed and the written image is stored.

SCANNING SIGNALS \ DATA SIGNALS		NON SELECTED	SELECTED	NON SELECTED
		V(0)	V(π)	V(0)
NON ADDRESSED	0	V	V	V
ADDRESSED	V(π)	2V	0	2V
NON ADDRESSED	0	V	V	V

Fig. 9-4 Addressing scheme for cholesteric $\leftrightarrow$ nematic transition type of matrix display.

In case of a matrix display, the number of scanning lines is limited by the ratio T/t_0 ($< T/\tau_1$). As T and τ_1 values are usually several seconds and several miliseconds, the ratio T/t_0 can be as high as several hundred.

9-3. Display Panel Construction

Figure 9-5 shows the structure of the present liquid-crystal display panel. The V_2 range giving successful display performance is given by an inequality, $0.6 \lesssim V/V_H \lesssim 0.9$, which gives a variation allowance in liquid-crystal layer thickness ℓ, since $V_H \propto \ell$. Since $\tau_{rp} \propto \ell^4$, a requirement for short τ_{rp} impose the upper limit on ℓ. A typical value of $\ell \simeq 8 \pm 1\,\mu m$ has been obtained in the whole display area. In case of large area panels, an MgF_2 layer was deposited onto one of the electrode surfaces, in order to avoid an electrical short. In case of reflective panels, a metalic dot reflector is provided for every picture element.

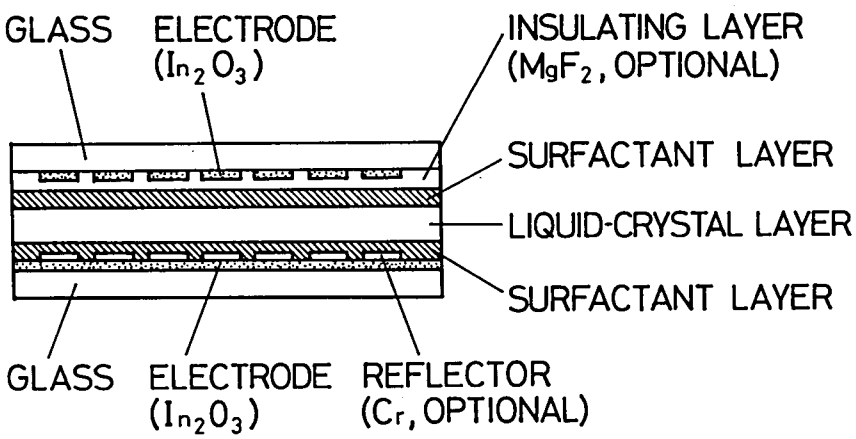

Fig. 9-5 Schematic cross section of liquid-crystal display panel.

The liquid-crystal material used for prototype devices is a mixture MBC, which is composed of 4'-methoxybenzylidene-4-*n*-butylaniline (MBBA), 4'-*n*-butoxybenzylidene-4-cyanoaniline (BBCA), and cholesteryl chloride (CC) in 70:20:10 weight ratio. In order to obtain a short τ_{rp}, FS150 ($C_8F_{17}SO_2NHCH_2CH_2CH_2N^+(CH_3)_3I^-$, Dainippon Ink & Chemicals, Inc.) was chosen as a surfactant for the substrate-surface treatment and its concentration in aqueous solution was selected to be 4×10^{-4} mol/l. It is because FS150, when used in such a concentration, produces $\Theta = 0°$ condition (see Fig. 5-4) and exhibits large B_θ ($10\pm2\times10^{-3}$ erg/cm^2; see Table 4-2(b)) for MBBA, which is the main component of cholesteric mixture MBC. Although some silane coupling agents nS are expected to exhibit larger B_θ than FS150 (see Table 4-2), FS150 is superior to nS in a sense of uniformity of large-area treatment. Especially, in the cases when MgF_2 layer exists, the uniformity of liquid-crystal alignment is extremely reduced on nS layers. The reason is considered to be that the siloxane bonding cannot be formed between nS and MgF_2 and, therefore, the nS adsorption ability becomes extremely weak.

Figure 9-6 shows the illumination scheme in a side-lit display. The lamp is located near one side of the panel, and the dark colored rear plate is located behind the panel. Light enters a glass plate at the side face of the panel and propagates inside the panel due to repeating total reflection. Then, it is scattered at the scattering regions of a liquid-crystal layer. With this illumination method, an excellent and uniform display image can be obtained.

9-4. Display Panel Characteristics

Two sizes of matrix display panels with storage effects were made. Figure 9-7 shows photographs of their model displays. Table 9-1 shows their main characteristics. No. 1 (side-lit type) and No. 2

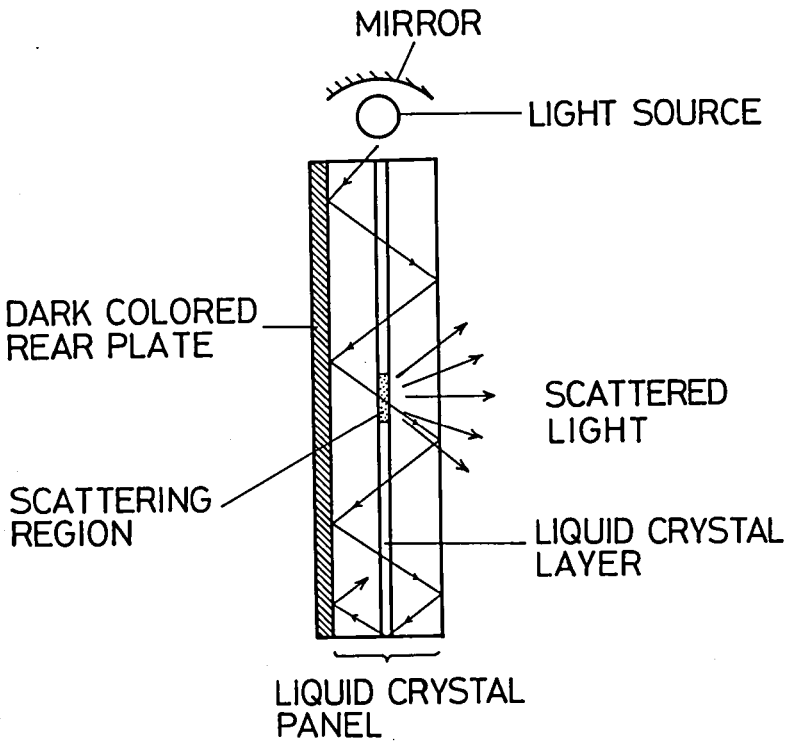

Fig. 9-6 Illumination scheme for side-lit mode display.

(reflective type) are the largest display panels made in the trial manufacture. No. 3 is the display panel of a prototype device which has capability of displaying 120 alphanumeric characters.

Although the driving voltage is rather high (14∿17 Volts) as compared with existing twisted-nematic mode display devices, it can be compatible with CMOS components. This cholesteric↔nematic transition mode has advantages of short writing time (8 ms/line), large number of scanning lines (> 100 lines), and a memory effect (storage time without voltage application is typically several hours). The "wash-out" problem caused by the transient light scattering after voltage removal is reduced effectively by the improved surface-treatment technique, that is the selection of surfactant material and the

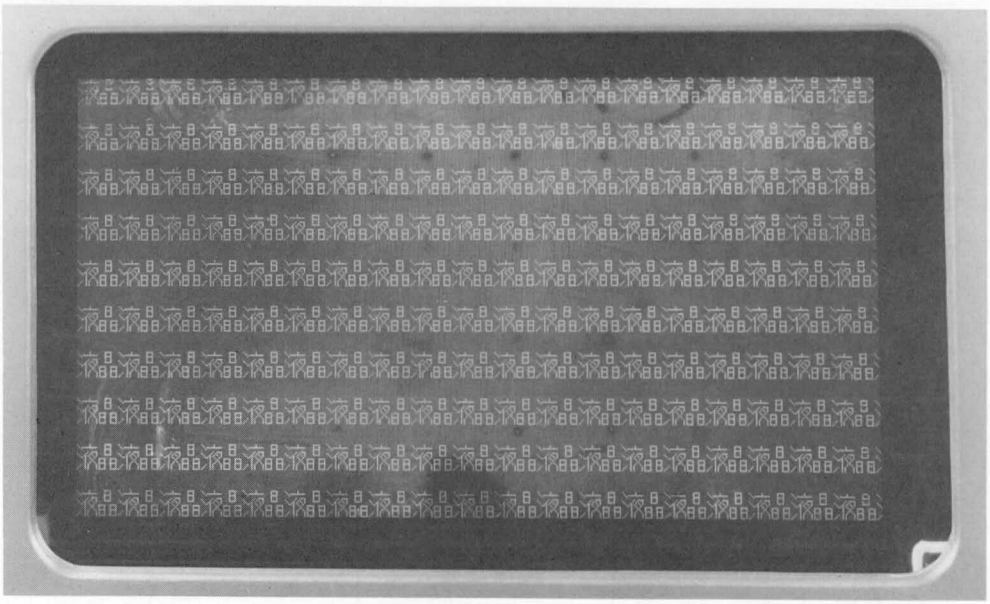

(a)

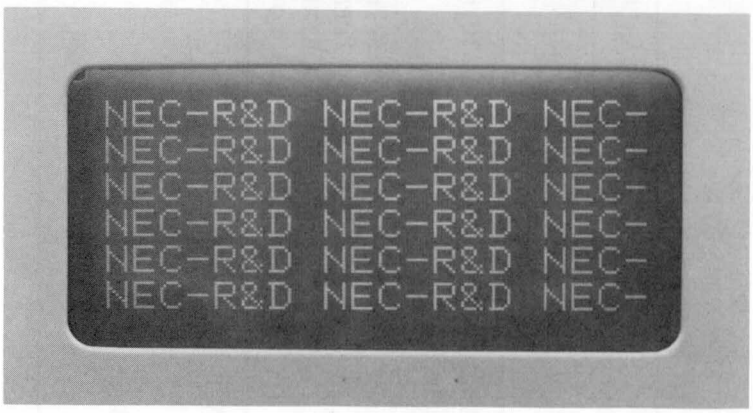

(b)

Fig. 9-7 Stored display images for model displays. (a) 122×230 mm^2 large-area panel (No. 2, reflective mode) and (b) 58×144 mm^2 medium-area panel (No. 3 , side-lit mode).

Table 9-1 Main characteristics of fabricated cholesteric ↔ nematic transition type of liquid-crystal matrix display devices.

	LARGE AREA PANELS		MEDIUM AREA PANEL
	No. 1 SIDE-LIT	No. 2 REFLECTIVE	No. 3 SIDE-LIT
EFFECTIVE DISPLAY AREA	122×230 mm^2		58×144 mm^2
NUMBER OF ELECTRODES	306×574		72×180
RESOLUTION	2.5 dots/mm		1.25 dots/mm
NUMBER OF CHARACTERS	320 CHINESE CHARACTERS IN 10 LINES		120 ALPHANUMERIC CHARACTERS IN 6 LINES
CHARACTER	16×18 dots		7×9 dots
DRIVING VOLTAGE (V_2)	±17 V	±14 V	±16 V
WRITING TIME (t_0)	8 ms/line	8 ms/line	8 ms/line
"WASH OUT" TIME (τ_{rp})	2 s	1s	1.5s
STORAGE TIME (τ_s)	SEVERAL HOURS	SEVERAL HOURS	3hrs

surface-treatment procedure. Relaxation time τ_{rp}, which corresponds to the "wash-out" time interval, is as short as $1 \sim 2$ s. Any differences in τ_{rp} values in Table 9-1 are the results of different liquid-crystal layer thickness for each panel.

9-5. Summary

The improved surface-treatment technique made it possible to reduce nematic → cholesteric relaxation time τ_{rp} as short as ~ 1 s and, therefore, remove the "wash-out" problem in the storage type of matrix display utilizing the cholesteric ↔ nematic transition mode. Among various operation modes, the cholesteric ↔ nematic transition mode with storage effect has several new features, when applied to matrix display. Those are

1) information once written is stored for several hours to several weeks and, therefore, no refreshing is required,

2) power consumption is extremely small, since no electrical power is required in retaining stored information,

3) driving voltage is small enough to be compatible with CMOS components,

4) the number of scanning lines can be as large as several hundred, by virtue of the long-sustaining metastable state of the cholesteric ↔ nematic transition effect,

5) the driving scheme applicable to the cholesteric ↔ nematic transition mode does not cause any crosstalk problems to arise, and

6) the acceptable viewing angle is larger than 140°, almost as large as 180°.

References

[1] M. Kawachi and O. Kogure, Jpn. J. Appl. Phys., 16, 1673 (1977)

[2] W. Greubel, Appl. Phys. Lett., 25, 5 (1974)

X. CONCLUSIONS

Although the importance of liquid-crystal interfacial alignment control for liquid-crystal display devices had been recognized, attention had been scarcely paid to the anchoring strength of liquid-crystal molecules at substrate surfaces and so-called strong-anchoring condition had been always assumed to be satisfied. The reason is because no method had been known to measure the anchoring strength. This dissertation, however, has presented a new method which has been developed to measure the anchoring strength. It has been demonstrated that the strong anchoring condition is not always realized. Many kinds of surface-treated substrates have been evaluated by their anchoring parameters, i.e., easy-axis angle Θ and anchoring-strength coefficient B_θ. Pertinent relationships have been clarified between surfactant structure or surface-treatment procedure and the anchoring-parameter values through the evaluation of substrate-surface energy polar and nonpolar components, γ_S^p and γ_S^d.

As a result, for liquid-crystal alignment mechanisms, the contributions of both polar forces and dispersive (nonpolar) forces have been clarified. What is important is that the anisotropies of liquid-crystal polar and nonpolar surface-energies play essential roles in liquid-crystal interfacial alignments and that anisotropic properties are not necessarily needed for the substrate surface to align liquid-crystal molecules on it. In addition to having clarified the liquid-crystal alignment mechanisms, it has become possible to calculate the necessary condition, γ_S^p and γ_S^d, and select a surfactant to realize the γ_S^p and γ_S^d condition in order to obtain desirable anchoring parameter values, Θ and B_θ, if necessary liquid-crystal characteristic parameters are known.

For the influence of liquid-crystal interfacial alignment on de-

vice characteristics, we have obtained the anchoring-parameter dependence of nematic→cholesteric relaxation time which characterizes the cholesteric↔nematic transition effect of cholesteric liquid crystals. This cholesteric↔nematic transition mode has many features, when used for a storage type of matrix display. Thus, it was possible to obtain a storage type of liquid-crystal matrix display with such a characteristic as a fast nematic→cholesteric relaxation, which has been improved from the viewpoint of substrate-surface treatment.

In Section II, wall effects on the Freedericksz transition have been analyzed. It has been shown that the threshold field strength H_c' for the Freedericksz transition is a function of anchoring parameters, Θ and B_θ. From the analyzed results, it has been demonstrated that anchoring-strength coefficient B_θ can be derived by measuring Θ and H_c'.

In Section III, new methods have been introduced for both interfacial alignment angle θ_0 and the Freedericksz-transition measurements. One is an improved magneto-capacitance method which is applicable even for distorted director distributions. The other is a total-reflection method which is applicable even for insulating glass substrate samples. It has become possible to derive the anchoring-strength coefficient B_θ for various liquid-crystal substrate interfaces, including insulating substrate cases, by using the magneto-capacitance method or the total-reflection method.

In Section IV, the equipment used for the anchoring-parameters measurements has been developed, and liquid-crystal anchoring-parameters, Θ and B_θ, have been derived on various surface-treated substrates. According to the measurements, it has been found that (1) liquid-crystal interfacial alignment angle θ_0 is 0° (homeotropic alignment, $\Theta = 0°$) for long-chain surfactant (typically number of carbon atoms $n \geqq 10$) and increases as chain length decreases, (2) the liquid-

crystal anchoring strength shows a maximum value when n = 14 or 16, (3) liquid-crystal anchoring strength also depends on the surfactant adsorption group, and B_θ values for cationic surfactants are larger than those for nonionic surfactants of the same chain length, and (4) for cationic surfactants, polished glass substrates reduce the liquid-crystal anchoring strength by almost half, as compared with In_2O_3 - evaporated glass substrates.

In Section V, surface energy polar and nonpolar components, γ_S^p and γ_S^d, have been measured for various surface-treated substrates. It has been found that γ_S^p and γ_S^d values exhibit different compositions in accordance with the surfactant material or the surfactant concentration in its solution used for surface treatment. In addition, relationships between liquid-crystal interfacial alignment angle θ_0 and the parameters, γ_S^p and γ_S^d, have been obtained. It has been found that MBBA molecules align homeotropically on low γ_S^d or low γ_S^p substrates. Thus, it has been clarified that the liquid-crystal interfacial alignment mechanisms are not uniform. That is, in some cases, polar forces play a decisive role and in other cases dispersive forces do.

In Section VI, it has been found that calculated easy-axis angles, which minimize the energy at interfaces between liquid-crystals (MBBA and 5CB) and substrates with various γ_S^p and γ_S^d values, agree well with the experimentally observed alignment angles θ_0. According to these calculations, the existing γ_c-hypothesis, saying that the homeotropic alignment is produced in the case when the substrate critical surface-tension γ_c is smaller than the liquid-crystal surface tension, has been shown to be valid, only when no polar interfacial-interaction contributions exist.

In Section VII, both calculations and measurements have been performed for substrate-surface energy γ_S^p and γ_S^d dependence of anchoring-

strength coefficient B_θ. The calculated results have been found to agree semiquantitatively with the experimental results. Thus, the weak anchoring conditions have been confirmed to be realized in usual liquid-crystal cells.

In Section VIII, the molecular realignment model has been proposed for the nematic→cholesteric relaxation. As is expected by the model, nematic→cholesteric relaxation time τ_{rp} has been found to depend on anchoring parameters, that is, τ_{rp} values become minimum in the case of $\Theta = 0°$ and are smaller as B_θ is larger. As a result, it has become possible to get a liquid-crystal display device with such an improved characteristic as a fast relaxation by selecting the surfactant material and the surface-treatment procedure to obtain a $\Theta = 0°$ and large-B_θ condition.

Finally, in Section IX, we have fabricated storage type of liquid-crystal matrix display devices utilizing the cholesteric↔nematic transition mode electro-optic effect. These devices have several new features: (1) information once written is stored for several hours to several weeks and, therefore, no refreshing is required, (2) power consumption is extremely small, since no electrical power is required in retaining stored information, (3) driving voltage is small enough to be compatible with CMOS components, (4) the number of scanning lines can be as large as several hundred, by virtue of the long-sustaining metastable state of the cholesteric↔nematic transition effect, (5) the driving scheme applicable to the cholesteric↔nematic transition mode does not cause any crosstalk problem to arise, and (6) acceptable viewing angle is larger than 140°, almost as large as 180°. Moreover, by using a surfactant FS150 ($C_8F_{17}SO_2NHCH_2CH_2CH_2N^+(CH_3)_3I^-$) for the substrate surface-treatment and selecting the concentration in its aqueous solution as 4×10^{-4} mol/l, the nematic→cholesteric relaxation time τ_{rp} has become as short as $\sim$1 s. Therefore, the "washout" problem at the point of storing the displayed information has

been diminished. As a result of the above features, display devices utilizing the cholesteric↔nematic transition mode have been shown to be superior to those utilizing other modes, such as the dynamic-scattering mode and the twisted-nematic mode, for a character or a graphic display use.

Suggestions for further study are summarized as follows. As a result of the physicochemical study on the liquid-crystal alignment mechanisms, it has been shown that the anisotropy of liquid-crystal surface energy has a close connection with the anchoring-parameter values. Although the anisotropy of liquid-crystal surface energy (the energy at free surface when liquid-crystal molecules align homeotropically or homogeneously) is not precisely equal to the characteristic parameters, $\Delta\gamma_L^d$, $\Delta\gamma_L^p$, etc., defined in this dissertation, its polar and nonpolar component values are considered to be connected with anchoring parameters through their magnitude, as compared with substrate surface-energy components. Consequently, it is expected that both to establish a method to measure the anisotropy of liquid-crystal surface energy and to perform measurements for various liquid-crystal materials are most effective to confirm the liquid-crystal interfacial-alignment mechanisms advocated in this dissertation and find an optimum surface-treatment technique for devices using those liquid-crystal materials.

From the anchoring-strength viewpoint, the surfactant FS150 used for the fabricated prototype devices in this study is not considered to be the best material, but silane coupling agents such as 14S and 16S seem better than FS150. Furthermore, recommended materials are silane coupling agents having both the same adsorption groups that nS has and the same perfluorocarbon chain as FS150 has. The reason why those silane coupling agents were not used for the present devices is that an MgF_2 layer was necessary as an insulator for other reasons than liquid-crystal alignment. If it is not improper to use inorganic

oxides, such as SiO_x, Ce_2O_3, etc., as an insulator, it is considered to be possible to form a uniform layer of silane coupling agents having siloxane bondings and, therefore, get improved display devices with shorter nematic→cholesteric relaxation time.

In addition to the present study on anchoring parameters, investigation in the liquid-crystal interfacial alignments has to be extended concerning the following: (1) the alignment should be physically stable, (2) surfactant molecules should be chemically and electrochemically stable, and (3) the surfactant layer should not cause the electric current to increase in the liquid-crystal cell. Moreover, as liquid-crystal materials for practical use have a tendency to be used in mixtures of many components, it seems to be necessary to clarify the relationships between anchoring parameters for liquid-crystal components and those for their mixtures.

APPENDICES

A. Conventional Methods for Elastic Constants Measurements

Nematic liquid-crystal elastic constants K_{ii} ($i = 1,2,3$) are measured by various methods, such as microscopic observations of field-induced periodic perturbation[1,2] or electrohydrodynamic instability [3], crossed-nicols observations of π-twist wall[4-6] or twisted nematic distortion[7], and Freedericksz-transition observations[7-16]. Among these methods, Freedericksz-transition observation is considered to be the most useful one, especially for K_{11} and K_{33} measurements. The reason is that the Freedericksz-transition observation method yields K_{11} and K_{33} independently and is relatively accurate, because the observation object is a critical phenomenon.

Various observation principles for the Freedericksz transition are reported, such as retardation[7-10], interference rings[11], pattern rotation[12,13], capacitance[1,14,15], and conductivity[16] measurements. Although the K_{33} value of MBBA has been obtained by using each of these measurements, previously reported K_{33} values of MBBA differ for each pertinent literature. The K_{33} values of MBBA reported in literature are shown in Fig. A-1 , together with surfactant materials used for obtaining MBBA homeotropic alignment.

Consider that the differences shown in Fig. A-1 are results of surfactant materials. Then, it is found that the surfactants located at the left side in Fig. A-1 (Lecithin and HTAB) exhibit smaller anchoring-strength coefficient B_θ than those at the right side in Fig. A-1 (DMOAP and Dodecanol). This is because K_{33} values, shown in Fig. A-1 were derived by using a relation $H_C' = (\pi/\ell)(K_{33}/\chi_a)^{1/2}$ and measured H_C'. The relation, however, is valid only when a strong anchoring condition ($\beta = \infty$) is realized and the difference $(\pi/\ell)(K_{33}/\chi_a)^{1/2} - H_C'$ becomes

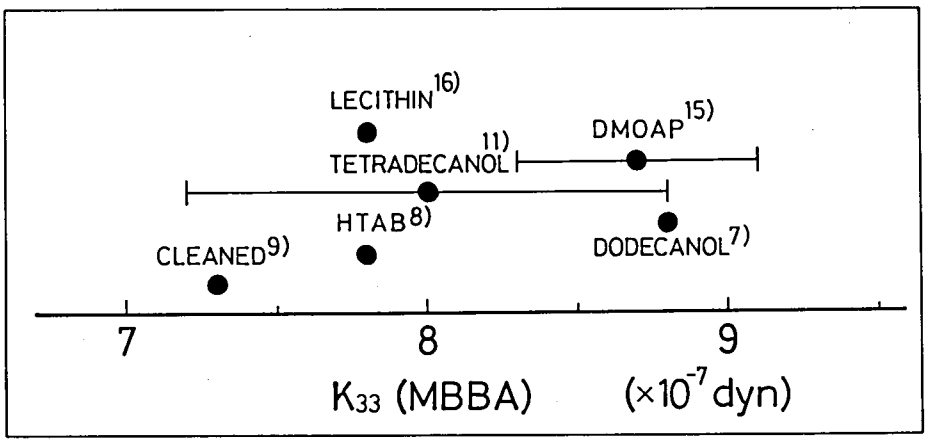

Fig. A-1 Reported K_{33} values of MBBA and surfactants used in measurements.

larger as β decreases (see Fig. 2-12). That is, the derived K_{33} value from the relation $H_c' = (\pi/\ell)(K_{33}/\chi_a)^{1/2}$ becomes smaller than the real K_{33} value as β (B_θ) decreases. This consideration is supported by the measured B_θ in this dissertation (see Table 4-2) showing that B_θ values for Lecithin, *n*-Hexadecanol (16OH, which is considered to be similar to Tetradecanol), and *n*-Hexadecyltrimethylammonium chloride (16Cl, which is considered to be similar to HTAB) are smaller than B_θ values for DMOAP (noted as 18S in this dissertation). Consequently, for a precise derivation of nematic liquid-crystal elastic constants using the Freedericksz-transition observations, it is important to use surface-treated substrates with large B_θ values and make the liquid-crystal layer thickness ℓ as large as possible in order to obtain large β ($= \ell B_\theta / \pi K_{33}$) .

B. Derivation of Liquid-Crystal Surface-Energy Anisotropy

Here, liquid-crystal molecular alignment on a long-chain surfactant layer is considered, where dispersive forces are dominant. In

this case, the γ_c-hypothesis is valid and the liquid-crystal interfacial alignment angle is determined by the liquid-crystal surface-energy dispersive component and substrate critical surface-tension. In the following, MBBA surface-energy anisotropy $\Delta\gamma_L^d$ is derived by utilizing measured parameters, Θ and B_θ, and γ_c for substrates with *n*-alkyltrimethylammonium bromide layers.

Considering only dispersive components, we have

$$W_S(\theta_0) = \gamma_S^d + \gamma_{LC}^d(\theta_0) - W_a^d(\theta_0) \quad , \tag{B-1}$$

$$W_S(\theta_0) = A/2 + (B_\theta / 2) \sin^2 (\theta_0 - \Theta) \quad . \tag{B-2}$$

By utilizing the foregoing assumptions

$$W_a^d(\theta_0) = 2[\gamma_S^d \gamma_{LC}^d(\theta_0)]^{1/2} \quad , \tag{B-3}$$

$$\gamma_S^d \simeq \gamma_c \quad , \tag{B-4}$$

and combining Eqs. (B-1) and (B-2), we can obtain

$$A/2 + (B_\theta / 2) \sin^2 (\theta_0 - \Theta) = \gamma_c + \gamma_{LC}^d(\theta_0) - 2\gamma_c^{1/2} \gamma_{LC}^d(\theta_0)^{1/2} \quad . \tag{B-5}$$

Consequently, in $\Theta = 0°$ case, we have

$$B_\theta / 2 = \gamma_{LC}^d(\pi/2) - \gamma_{LC}^d(0) - 2\gamma_c^{1/2} [\gamma_{LC}^d(\pi/2)^{1/2} - \gamma_{LC}^d(0)^{1/2}] . \tag{B-6}$$

Here, the γ_c values were measured for substrates with *n*-alkyltrimethylammonium bromide layers by utilizing the contact-angle method (see Section 6-3-2). The obtained γ_c values are shown in Fig. B-1, in contrast with number of carbon atoms n in surfactant alkyl chain.

As $\gamma_{LC}^d(0) < \gamma_{LC}^d(\theta) < \gamma_{LC}^d(\pi/2)$ is valid (see Section 6-3) for MBBA, homeotropic alignment $\theta_0 = \Theta = 0°$ is considered to be realized for $\gamma_c < \gamma_{LC}^d(0)$ cases. Experimental results in Fig. B-1 exhibit that $\Theta = 0°$ is obtained for $n \geqq 12$, that is $\gamma_c < 26$ erg/cm^2. This means that

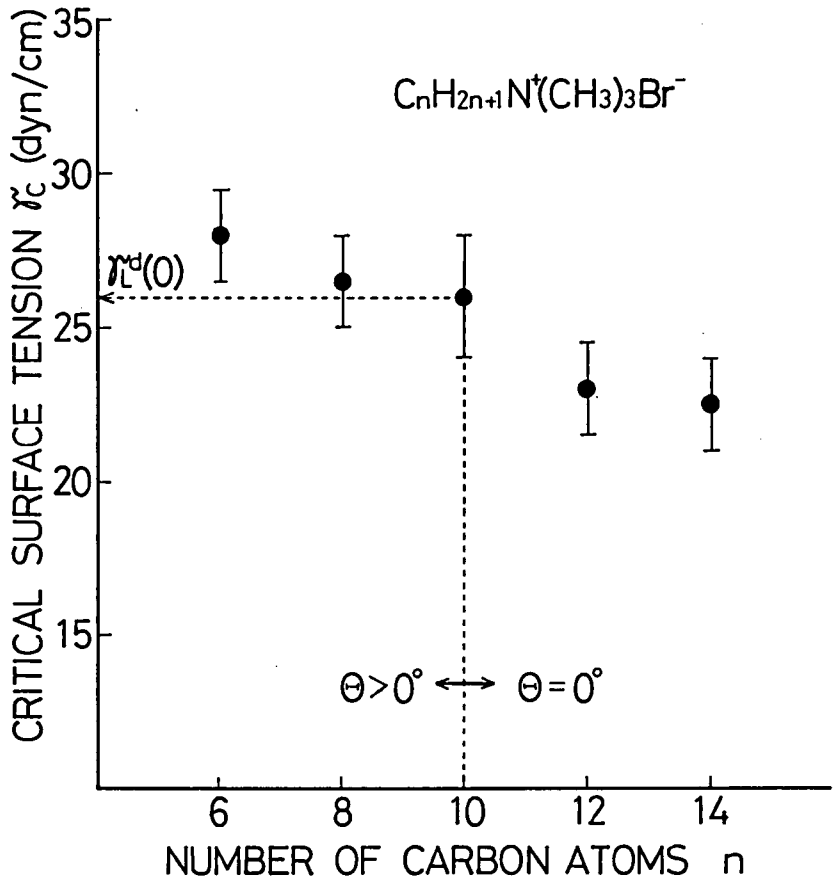

Fig. B-1 Critical surface-tension for substrates with *n*-alkyltrimethylammonium bromide layers.

$\gamma_{LC}^d(0) = 26$ erg/cm^2 for MBBA. Moreover, B_θ values were obtained to be 7×10^{-3} and 9×10^{-3} erg/cm^2 for n = 12 and 14 cases, respectively (see Table 4-2). The insertion of these $\gamma_{LC}^d(0)$, γ_c, and B_θ values into Eq. (B-6) yields $\gamma_{LC}^d(\pi/2)$ for MBBA and finally gives the MBBA surface-tension anisotropy $\Delta\gamma_L^d = \gamma_{LC}^d(\pi/2) - \gamma_{LC}^d(0) = (4.5 \pm 1.3)\times10^{-2}$ erg/cm^2.

Despite various assumptions and rough determination of γ_c values for $\Theta = 0°$, the obtained MBBA surface-tension anisotropy is very small and on the same order as reported for 5CB in a literature[17]. As

this $\Delta\gamma_L$ value was obtained by using measured B_θ values, it is of less meaning to use this $\Delta\gamma_L$ value for B_θ calculations from γ_S^d and γ_S^p values. However, it is used in Section VII for B_θ calculations, as this order of $\Delta\gamma_L$ value is supported by another independent measurement[17].

References

[1] F. Rondelez and J. P. Hulin, Solid State Commun., 10, 1009 (1972)

[2] F. Rondelez, H. Arnould, and C. J. Gerritsma, Phys. Rev. Lett., 28, 735 (1972)

[3] Y. Galerne, G. Durand, M. Veyssie, and V. Pontikis, Phys. Lett., 38A, 449 (1972)

[4] L. Leger, Mol. Cryst. Liq. Cryst., 24, 33 (1973)

[5] L. Leger, Solid State Commun., 11, 1499 (1972)

[6] L. Leger, Solid State Commun., 10, 697 (1972)

[7] W. H. de Jeu, W. A. P. Claassen, and A. M. J. Spruijt, Mol. Cryst. Liq. Cryst., 37, 269 (1976)

[8] I. Haller, J. Chem. Phys., 57, 1400 (1972)

[9] J. Robert, G. Labrunie, and J. Borel, Mol. Cryst. Liq. Cryst., 23, 197 (1973)

[10] R. E. Michel and G. W. Smith, J. Appl. Phys., 45, 3234 (1974)

[11] C. Williams and P. E. Cladis, Solid State Commun., 10, 357 (1972)

[12] P. E. Cladis, Phys. Rev. Lett., 28, 1629 (1972)

[13] F. Leenhouts, F. Van der Woude, and A. J. Dekker, Phys. Lett., 58A, 242 (1976)

[14] D. Meyerhofer, Phys. Lett., 51A, 407 (1975)

[15] D. Meyerhofer, J. Appl. Phys., 46, 5084 (1975)

[16] M. Greulich, G. Heppke, and F. Schneider, Z. Naturforsch., 30a, 515 (1975)

[17] J. E. Proust, E. Perez, and L. Ter-Minassian-Saraga, Colloid and Polymer Sci., 254, 672 (1976)

ACKNOWLEDGMENTS

The author wishes to express his deep appreciation to Professor Akio Sasaki of Kyoto University for his invaluable advice and encouragement throughout the present work and his stimulating discussions and criticisms on the manuscript. The author is grateful to Professor Toshinori Takagi of Kyoto University for his invaluable advice and encouragement, who had guided the author to the study on liquid crystals as a senior and a master course student. The author is also grateful to Professor Akira Kawabata of Kyoto University for his encouragement, who had given the author a chance to study on liquid crystals. Appreciation is due to Professor Isao Yamada of Kyoto university for his continuous encouragement.

The author wishes to extend his gratitude to Dr. Fujio Saito, assistant general manager of Opto-Electronics Research Laboratories, Nippon Electric Company, for his continuous guidance, encouragement, and invaluable advice throughout the present work. Appreciation is due to Dr. Teiji Uchida, general manager of Opto-Electronics Research Laboratories, Nippon Electric Company, and Dr. Michiyuki Uenohara, associate senior vice president and director research of Nippon Electric Company, for their encouragement.

The author wishes to thank Dr. Yoshitake Ohnishi and Tatsuo Onozawa for their helpful discussions especially on anchoring-parameters derivation. Thanks are due to Fumihiro Ogawa for his discussion on total-reflection measurements and to Toshihiko Ueno for his discussion on substrate surface-energy derivations. Thanks are also due to Chizuka Tani for his discussion on the cholesteric spiral texture. The author also thanks Dr. Junji Matsui for photographing and discussing reflective electron diffraction patterns.

Besides those members in Nippon Electric Company, the author

wishes to express his appreciation to Osamu Kogure and other staff members in Ibaraki Electrical Communication Laboratory of Nippon Telegraph and Telephone Public Corporation for their continuous discussions and advice on the cholesteric↔nematic transition effect and fabrication of model display devices. Appreciation is also due to Takeshi Imai in Research Division of Toray Silicone Company, who synthesized and supplied the silane coupling agents.

PUBLICATIONS LIST

[1] "Measurement of Anisotropic Interfacial Interactions between a Nematic Liquid Crystal and Various Substrates"

S. Naemura

Appl. Phys. Lett., 33, 1 (1978)

[2] "Anisotropic Interactions between MBBA and Surface-Treated Substrates"

S. Naemura

J. Phys. (Paris), C3-40, C3-514 (1979)

[3] "Storage-Type Liquid-Crystal Matrix Display"

C. Tani, F. Ogawa, S. Naemura, T. Ueno, F. Saito, and O. Kogure

Proc. S.I.D., 21, 71 (1980)

[4] "Polar and Nonpolar Contributions to Liquid-Crystal Orientations on Substrates"

S. Naemura

J. Appl. Phys., 51, 6149 (1980)

[5] "Physicochemical Study on Liquid-Crystal Substrate Interfacial Interactions"

S. Naemura

Mol. Cryst. Liq. Cryst., 68, 183 (1981)

ORAL PRESENTATIONS LIST

A. International Liquid Crystal Conference

[1] "Anisotropic Interactions between MBBA and Surface-Treated Substrates"

S. Naemura

7th Int'l. Liq. Cryst. Conf., Bordeaux, July, 1978, HP62

(This has been published as [2] in Publications List.)

[2] "Physicochemical Study on Liquid-Crystal Substrate Interfacial Interactions"

S. Naemura

8th Int'l. Liq. Cryst. Conf., Kyoto, July, 1980, J-6

(This has been published as [5] in Publications List.)

B. Society for Information Display

[3] "Storage-Type Liquid-Crystal Matrix Display"

C. Tani, F. Ogawa, S. Naemura, T. Ueno, F. Saito, and O. Kogure

1979 SID International Symposium, Chicago, May, 1979, 13.3

(This has been published as [3] in Publications List.)

C. Liquid Crystal Conference in Japan

[4] "Anisotropic Interfacial Interactions between a Nematic Liquid Crystal and Surface-Treated Substrates"

S. Naemura

3rd Conference, Science Univ. of Tokyo, November, 1977, 2A21

[5] "Liquid-Crystal Alignment on Substrates with Surfactant Layers"

S. Naemura

4th Conference, Nagoya Univ., October, 1978, 2S16

[6] "Substrate Surface Energy and Liquid-Crystal Orientation"

S. Naemura

5th Conference, Kyushu Univ., October, 1979, 1Q19

D. Japan Society for the Promotion of Science, The 142 Committee of Organic Materials for Information Science

[7] "Liquid-Crystal Molecular Orientations on Long-Chain Alkylsilane Layers"

S. Naemura

Tohoku Univ., June, 1979

E. Japan Society of Applied Physics

[8] "Storage-Type Electro-Optic Effect in a Dielectrically Positive Nematic and Small Amount of Cholesteric Liquid-Crystal Mixture"

S. Naemura, Y. Ohnishi, and F. Saito

21st Spring Meeting of JSAP, Toyo Univ., April, 1974, 1p-B-11

[9] "Measurements of Wall Effects on Freedericksz Transition by Total-Reflection Method"

S. Naemura

38th Fall Meeting of JSAP, Okayama Univ., October, 1977, 13a-C-3

[10] "Wall Effects on Relaxation Time in Phase-Transition Type Storage Liquid-Crystal Cell"

S. Naemura

25th Spring Meeting of JSAP, Musashino Inst. Tech., March, 1978, 29p-G-5

F. Institute of Electronic and Communication Engineers of Japan

[11] "Storage-Type Matrix Liquid-Crystal Display"

O. Kogure, M. Kawachi, K. Kato, S. Yoshii, F. Saito, C. Tani, and S. Naemura

The Professional Group of Electronic Components and Materials of IECEJ, May, 1975, CPM75-11

G. The Institute of Television Engineers of Japan

[12] "Phase-Transition Type Storage Liquid-Crystal Display"

F. Saito, C. Tani, F. Ogawa, S. Naemura, T. Ueno, Y. Ohnishi, and T. Onozawa

The Professional Group of Electronic Devices of ITEJ, November, 1978, ED408